Université de Toulouse

eman ta zabal zazu

Universidad del País Vasco　Euskal Herriko Unibertsitatea

Resonant Raman-Brillouin Scattering in Semiconductor and Metallic Nanostructures

From Nano-Acoustics to Acousto-Plasmonics

Nicolas LARGE

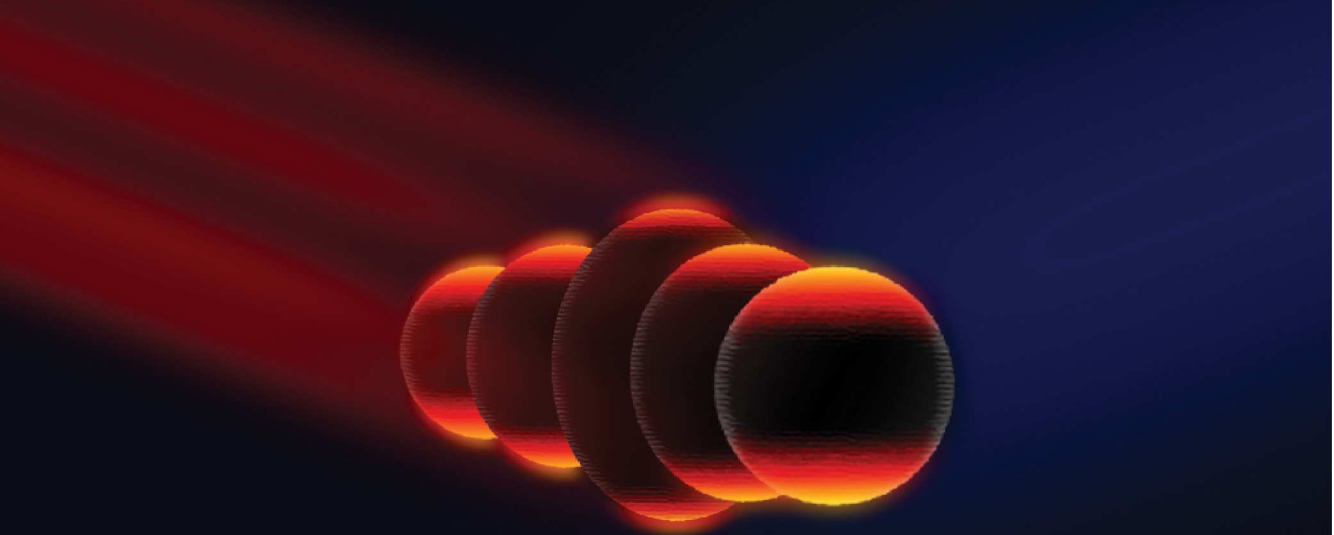

Thesis supervised by
Prof. Adnen MLAYAH and Dr. Javier AIZPURUA

- 2011 -

Université
de Toulouse

eman ta zabal zazu

Universidad
del País Vasco

Euskal Herriko
Unibertsitatea

Resonant Raman-Brillouin Scattering in Semiconductor and Metallic Nanostructures: from Nano-Acoustics to Acousto-Plasmonics

by

Nicolas LARGE

ED Sciences de la Matière, and Departamento de Física de Materiales

A thesis submitted for the degree of

Doctor of Philosophy

at the

Université de Toulouse, and Universidad del País Vasco

Specialities

“Nanophysique”
and “Physics of Nanostructures and Advanced Materials”
(Física de Nanoestructuras y Materiales Avanzados)

To my loving parents, Gigi and Alain, my brothers, Thomas, Loïc, Pascal,
and to the woman I shared my life with during the past seven years, Narie,
who gave me the strengh to overcome the difficulties and my doubts.

Acknowledgements

I wish to express my deepest and most sincere acknowledgments to my supervisors Prof. Adnen Mlayah and Dr. Javier Aizpurua. They helped me to develop my scientific knowledge and skills but also my personality. They constantly supported, guided, and encouraged me, giving me freedom and confidence necessary for innovative and interesting research. The also taught me so many things from a scientific point of view but also from a personal side that I can not enumerate everything here but the numerous discussions about physics or life have made me a better and more confident person. I am grateful to them for giving me the opportunity to work in a such nice environment with so good conditions. The “Cotutelle” has been a great human and scientific experience from that I have learnt a lot.

I also would like to express many thanks to Dr. Lucien Saviot and Dr. Arnaud Arbouet, for their theoretical and experimental investigations of the nanoparticle vibrations and for their help, their advice and the interesting discussions about physics and research.

I sincerely thank people from research centers I belonged to: CEMES, CFM and especially from DIPC where I spent good moments and where I met nice people ready to help me. Many thanks to Belén, Carmen, Luz and Txomin from the computing center to Ana, Marimar and Amaia from the administration as well as Nerea from the Nanophotonics group I belonged to. Furthermore, I also want to thank to the President of the DIPC, Prof. Pedro Miguel Echenique for the great working conditions he creates in the Donostia International Physics Center. I would like to express also my most sincere friendly feelings to all the PhD students and the post-docs I worked with and I shared such nice moments with: Juan Pablo, Aitzol, Eneko, Olalla, Marco, Renaud, Victoria, Alejandro, Pablo, Ruben, and all the others.

Special thanks are addressed to the people who were the most important for me for years and especially during the last four ones. First my parents and my brothers who supported and encouraged me all the time and who never hesitate to come to San Sebastián when I went through difficult periods, and in particular Loïc for his help in the conception of some of the figures presented in this manuscript. Thanks again to my best friends Arnaud, Hans, Rémi, and Sylvain for their help, support and advice although they were sometimes far from “here”. The last person I would like to thank, but not the least, is the woman who shared my life for the last seven years, Narie, and who brought me strength, happiness, support and encouragements to overcome all the doubts and difficulties.

Thanks to all of you! Merci à tous! ¡Muchas gracias a todos!

Abstract

The 21^{st} century has seen the emergence of new technologies in several fields. Nano-objects and nanostructures are now involved in a variety of applications in bio-medicine, electronics, telecommunication devices, new compounds for aeronautics and sport equipments or pharmaceutical products. To develop such applications, one needs to understand the modifications of the physical laws when downsizing the materials to the nanoscale. Nanofabrication, experimental and theoretical aspects are still a challenge to fully understand fine optical and vibrational properties of these nanostructures.

This work is devoted to the study of the optical and vibrational properties of semiconductor and metallic nanostructures. The inelastic light scattering by low frequency acoustic vibrations (few meV), named Raman-Brillouin scattering, gives access to such properties. On one hand, due to their size, the electronic states of semiconductor nanostructures (e.g. quantum wells, nanowire or quantum dots) are confined and discretized. These electronic states are involved in the Raman-Brillouin scattering and act as an intermediary during the optical process. On the other hand, when applying an external electric field, metallic nano-objects sustain collective oscillation modes of the free electron gas called surface plasmons. In the Raman-Brillouin scattering, these surface plasmon modes also act as an intermediary during the emission and the absorption of low frequency acoustic vibrations. The understanding of the interaction between the acoustic vibrations and the electronic excitations, whether they are excitons (confined electronic states in semiconductors) or surface plasmons (in metals), gives direct information on the optical and vibrational properties of those nano-objects.

This work is based on the development of numerical simulations devoted to the understanding these interaction processes. In particular, new physical concepts are introduced as theoretical tools for the interpretation of the Raman-Brillouin scattering in semiconductors and metals. An effective electronic density, called the “Raman-Brillouin Electronic Density”, which is responsible for the Raman-Brillouin scattering in semiconductors, is here introduced for the first time. This physical quantity is a new advanced theoretical tool for the interpretation of the inelastic light scattering processes by low frequency acoustic vibrations. Finally, the concept of acousto-plasmonics is also introduced for the first time to study and describe the modulation of the plasmonic properties of metallic nano-objects by the acoustic vibrations. To do so, advanced numerical methods such as the Boundary Element Method (BEM), the Discrete Dipole Approximation (DDA) or the Finite-Difference Time Domain (FDTD) have been used to solve Maxwell’s equations in the case of metallic nano-objects.

These methods as well as the concepts introduced in this work allow for the study of the optical properties of metallic nano-objects, such as spherical nanoparticles, nanocolumns, nanorings, nanodisks, nano-antennas, and dimers of nanoparticles and of semiconductor nanostructures, such as membranes and superlattices. They allowed to interpret fine physical effects such as significant and unpredicted spectral red-shifts of plasmons resonances in gold nanorings and unexpected observations of acoustic vibration modes by Raman-Brillouin spectroscopy, whether it is in semi-conductors or in metals. The latter lead to the establishment of new Raman-Brillouin selection rules in silver nanocolumns.

Keywords: Semiconductors; (Mutiple) Quantum wells; Confined electronic states; Excitons; Perturbations theory; Quantum mechanics; Metallic nanostructures/nanoparticles; Plasmonics; Surface plasmon-polaritons; Near-field optics; Optical properties of nanoparticles; Nano-optics; Nanophotonics; Electromagnetic field; Acoustic vibrations; Phonons; Acousto-plasmonics; Raman-Brillouin scattering/spectroscopy; Numerical simulation/modeling; Finite- difference time-domain (FDTD); Discrete dipole approximation (DDA); Boundary element method (BEM).

French abstract - Résumé

Le XXI$^{\text{ème}}$ siècle a vu l'avènement des nouvelles technologies dans un grand nombre de domaines. Du bio-médical, à l'électronique, en passant par les télécommunications, les nouveaux alliages pour l'aéronautique ou pour les équipements sportifs ou même les cosmétiques, l'utilisation de nano-objets ou de nanostructures a été une révolution. La course à la miniaturisation des systèmes nécessite de comprendre ce qu'il se passe lorsque l'on réduit la taille des objets. La nano-fabrication ainsi que les études expérimentales et théoriques restent un défi pour une compréhension fine des propriétés optiques et vibrationnelles de ces nanostructures.

Ce travail de thèse s'articule autour de l'étude des propriétés optiques et vibrationelles de nanostructures semiconductrices et métalliques par le biais des processus de diffusion inélastique de la lumière par les vibrations acoustiques basses fréquences (quelques meV) présentes dans les matériaux : la diffusion Raman-Brillouin. Les nanostructures semiconductrices (ex : puits, fils ou boites quantiques) possèdent, de par leurs dimensions nanométriques, des états électroniques confinés, qui sont impliqués dans le processus de diffusion Raman-Brillouin. Les excitations électroniques (excitons) sont des intermédiaires lors de ce processus. Les nano-objets métalliques, lorsqu'ils sont soumis à un champ électrique externe, supportent quand à eux des modes d'oscillation collective des électrons de conduction appelés plasmons de surface. Lors de la diffusion Raman-Brillouin, les plasmons de surface jouent le rôle d'intermédiaires lors du processus d'absorption ou d'émission des vibrations acoustiques dans le système. L'étude des interactions entre les modes de vibrations acoustiques et les excitations électroniques, que ce soient des excitons (semiconducteurs) ou des plasmons de surface (métaux), sondées par spectroscopies optiques, nous renseignent directement sur les propriétés optiques et vibrationnelles de ces nano-objets.

Ce travail de recherche s'axe plus spécifiquement sur le développement d'outils numériques pour la modélisation de ces processus d'interaction. De nouveaux concepts physiques sont introduits pour l'interprétation des processus de diffusion Raman-Brillouin dans les nanostructures semiconductrices et métalliques. Ainsi, une densité électronique effective, “Raman-Brillouin Electronic Density”, directement responsable de la diffusion Raman-Brillouin dans le cas des semiconducteurs, est introduite ici pour la première fois. Cette quantité physique est un outils d'interprétation avancés des processus de diffusion inélastique de la lumière par les vibrations acoustiques basses fréquences. Enfin, le concept d'acousto-plasmonique est également introduit pour la première fois afin de rendre compte et de décrire la modulation des propriétés plasmoniques des nano-objets métalliques par les vibrations acoustiques. Pour ce faire, l'utilisation de méthodes numériques avancées telles que la Boundary Element Method (BEM), la Discrete Dipole Approximation (DDA) ou encore la Finite-Difference Time Domain (FDTD) a été nécessaire afin de résoudre les équations de Maxwell dans le cas des nano-objets métalliques.

Les méthodes utilisées et les concepts introduits ont permis l'étude des propriétés optiques de nano-objets métalliques, tels que des nanoparticules sphériques, nanocolonnes, nano-anneaux, nanodisques, nano-antennes et dimères de nanoparticules ainsi que des nanostructures semiconductrices telles que des membranes et des super-réseaux. Ils ont permis de rendre compte d'effets physiques fins tels que d'importants décalages vers le rouge non prédits de résonances plasmons dans des nano-anneaux d'or ou encore l'observation inattendue de certains modes de vibrations acoustiques par spectroscopie Raman-Brillouin, que se soit dans les semiconducteurs ou bien les métaux. Ce dernier a conduit l'établissement de nouvelles règles de sélection Raman-Brillouin dans des nanocolonnes d'argent.

Mots clés : Semiconducteurs ; (Multi-)Puits quantiques ; Etats électroniques confinés ; Excitons ; Théorie des perturbations ; Mécanique quantique ; Nanostructures/nanoparticules métalliques ; Plasmonique ; Plasmons de surface ; Polaritons ; Champ proche ; Propriétés optiques de nanoparticules ; Nano-optique ; Nanophotonique ; Champs électromagnetiques ; Vibrations acoustiques ; Phonons ; Diffusion/ spectroscopie Raman-Brillouin ; Simulation/modélisation numérique ; Finite-difference time-domain (FDTD) ; Discrete dipole approximation (DDA) ; Boundary element method (BEM).

Spanish abstract - Resumen

El siglo XXI ha sido testigo del impacto de las nuevas tecnologías en un gran número de sectores, desde el biomédico, y la electrónica, pasando por las telecomunicaciones, las nuevas aleaciones para la aeronáutica o para los equipos deportivos o también los productos farmacéuticos. La utilización de nano-objetos o de nano-estructuras ha supuesto una revolución. La carrera de la miniaturización de los sistemas hace necesaría la comprensión de lo que sucede cuando se reduce el tamaño de los objetos. La nanofabricación, así como el desarrollo de los estudios experimentales y teóricos suponen un constante reto para la comprensión profunda de las propiedades ópticas y vibracionales de estas nano-estructuras.

Este trabajo de tesis se articula alrededor del estudio de las propiedades ópticas y vibracionales de nano-estructuras semiconductoras y metálicas mediante el estudio de los procesos de difusión inelástica de la luz por las vibraciones acústicas de frecuencias bajas (algunos meV) presentes en los materiales: la difusión Raman-Brillouin. Las nano-estructuras semiconductoras (p.ej.: pozos, hilos o puntos cuánticos) poseen, por sus dimensiones nanométricas, estados electrónicos confinados, que participan en el proceso de difusión Raman-Brillouin. Las excitaciones electrónicas (i.e. excitones) son unos intermediarios en este proceso. Los nano-objetos metálicos, cuando están sometidos a un campo eléctrico externo, soportan unos modos de oscilación colectiva de los electrones de conducción llamados plasmones de superficie. En la difusión Raman-Brillouin de metales, los plasmones de superficie son los que desempeñan el papel de intermediarios en el proceso de absorción o de emisión de las vibraciones acústicas en el sistema. El estudio de las interacciones entre los modos de vibraciones acústicas y las excitaciones electrónicas, mediante sondas espectroscópicas ópticas, sean excitones (semiconductores) o plasmones de superficie (metales), nos informa directamente sobre las propiedades ópticas y vibracionales de estos nano-objetos.

Este trabajo de investigación desarrolla la modelización numérica de estos procesos de interacciones. Se introducen nuevos conceptos físicos para comprender los resultados experimentales y entender los fundamentos de cada proceso de difusión Raman-Brillouin en las nano-estructuras semiconductoras y metálicas. Así, se introduce por primera vez una densidad electrónica efectiva, "Raman-Brillouin Electronic Density", directamente responsable de la difusión Raman-Brillouin en el caso de los semiconductores. Esta cantidad física es herramienta teórica avanzada para la interpretación de los procesos de difusión inelástica de la luz por las vibraciones acústicas de frecuencias bajas. Por último, se presenta también por primera vez el concepto de acousto-plasmónica con el fin de describir la modulación de las propiedades plasmónicas de los nano-objetos metálicos por las vibraciones acústicas. Para ello, se utilizan métodos numéricos avanzados tales como el Boundary Element Method (BEM), Discrete Dipole Approximation (DDA) y Finite-Difference Time Domain (FDTD) con el fin de resolver las ecuaciones de Maxwell en el caso de nano-objetos metálicos.

Los métodos utilizados y los conceptos introducidos han permitido el estudio de las propiedades ópticas de nano-objetos metálicos, tales como las nanopartículas esféricas, las nanocolumnas, los nanoanillos, los nanodiscos, las nanoantenas y dímeros de nanopartículas y también de nano-estructuras semiconductoras, tales como membranas y super-redes. Se han estudiado de efectos tales como corrimientos hacia el rojo de resonancias de plasmones no predichos en nano-anillos de oro o también la observación inesperada de ciertos modos de vibraciones acústicas por espectroscopía Raman-Brillouin, ya sea en los semiconductores así como en los metales. Esta último estudia condujo al establecimiento de nuevas reglas de selección Raman-Billouin en nanocolumnas de plata.

Palabras clave: Semiconductores; (Multi-)Pozos cuánticos; Estados electrónicos confinados; Excitones; Teoría perturbacional; Mecánica cuántica; Nanoestructuras/ nanopartículas metalícas; Plasmónica; Plasmones de superficie; Polaritones; Campo cercano; Propiedades ópticas de nanopartículas; Nanoóptica; Nanofotónica; Campos electromagnéticos; Vibraciones acústicas; Fonones; Acousto-plasmónica; Dispersión/ espectroscopía Raman-Brillouin; Simulación/modelización numérica; Finite-difference time-domain (FDTD); Discre-

te dipole approximation (DDA); Boundary element method (BEM).

Contents

List of Figures

List of Tables

Introduction

Although nanotechnology is a relatively recent research field (the term “nanotechnology” was first defined by Norio Taniguchi in 1974), the development of its central concepts happened over a longer period of time. Nanotechnology has unwittingly been used for thousands of years in making steel, in vulcanizing rubber, and in paintings (e.g. Lycurgus Cup, Notre Dame Cathedral in Paris). Moreover, nanometer-scale structures are also present in Nature: photonic crystals on butterfly wings give their colors. Each of these processes relies on the properties of stochastically-formed atomic ensembles of several nanometers in size, and are distinguished from chemistry in that they do not rely on the properties of individual molecules but rather on the properties that reach several hundreds of atoms. However, the development of the body of concepts now subsumed under the term nanotechnology has been slower. Indeed, the first mention of some of the distinguishing concepts in nanotechnology was in 1867 by James Clerk Maxwell when he proposed as a thought experiment a tiny entity known as Maxwell’s Demon able to handle individual molecules. The first observations and size measurements of nanoparticles were made during the first decade of the 20^{th} century. They are mostly associated with Richard Adolf Zsigmondy who made a detailed study of gold sols and other nanomaterials with sizes less than 10 nm by use of a dark-field ultramicroscope. Zsigmondy was the first who used “nanometer” explicitly for characterizing particle size in 1914.

Nowadays, a large set of materials and improved products relies on a change in their physical properties when the feature sizes are shrunk. Nano-objects and nanostructures are now involved in a variety of applications in bio-medicine (e.g. drug delivery, assisted surgery, medical imaging, diagnostic sensors, and cancer therapy) [93; 111; 139], electronics (e.g. transistors, integrated circuits, molecular electronic devices, NEMS, and photo detectors/solar cells) [13; 132; 141; 177], telecommunication devices (e.g. nano-antennas, optical switches, waveguides, and optical lenses) [96; 164; 173], in aeronautics, aerospace and sport equipments (e.g. increase of optical, thermal, electric or mechanical properties of steel, glass, polymers and other compounds) [22], or cosmetics (e.g. sunscreens, and anti-aging cream). To develop such applications, it is necessary to understand the underlying physics when shrinking the size of the materials to the nanoscale. Nanofabrication, experimental and theoretical studies are still challenging to fully understand fine properties of these nanostructures.

This work is devoted to the study of the optical properties of nanostructures and nano-objects [65; 138]. More specifically, it focuses on inelastic light scattering properties of such nanomaterials [30; 194]. Based on the development of numerical tools, the interaction between electronic excitations and low frequency acoustic vibration modes [few milli-electronvolts (meV)] involved in the Raman-Brillouin scattering process are investigated. A first part of the manuscript is devoted to the understanding of the optical and acoustic properties of semiconductor nanostructures [98; 128]. After a brief overview of the Raman-Brillouin scattering (Chapter 1) I introduce, in the case of a freestanding silicon membrane, a Raman-Brillouin Electronic Density which is a new theoretical tool for the interpretation of the Raman-Brillouin spectra (Chapter 2). A third chapter (Chapter 3) is then dedicated to the extension of the Raman-Brillouin Electronic Density formalism to a more complex system: a semiconductor superlattice. The second part, is dedicated to metallic nano-objects and to their optical properties. I first introduce the basic physics of acoustic vibrations [162] and surface plasmons [69; 115; 166] (Chapter 4). The last two chapters are devoted to the plasmonic properties (Chapter 5) [96; 97] and to the acousto-plasmonic dynamics (Chapter 6) [99; 100] of metallic nano-objects.

Part I - Nano-Acoustics of Semiconductor Nanostructures

Inelastic light scattering by acoustic vibrations in low dimensional systems has attracted much interest since the early works of Merz *et al.* [121] and Colvard *et al.* [38] who observed light scattering by acoustic phonons (acoustic vibrations) due to Brillouin zone folding in semiconductor superlattices (SLs). Afterwards, many experimental and theoretical studies have extended the use of Raman-Brillouin scattering to the study of nanostructures [30; 88; 194] consisting of spatially distributed quantum objects (wells, wires, dots) [30; 88; 158]. The interest lies in the fact that the wavelengths of acoustic vibrations, in solids and in the THz frequency range, are of the order of few nanometers, i.e. well adapted to nano-sized objects [15; 127]. Another important advantage of acoustic phonons is the delocalized nature of their displacement field. Unlike optical phonons, which are usually confined within one type of material, acoustic vibrations may extend over distances much larger than the average separation between distributed scatterers. As a result, collective effects, due to spatial ordering, appear in the electron-phonon interaction and in the light scattering process [15; 127]. Hence, the information that can be extracted through modeling and simulations of the Raman-Brillouin spectra is very rich (size and shape distributions, spatial correlations...).

Low-frequency Raman-Brillouin scattering in semiconductor SLs displays spectral features related to folding of acoustic phonons which originates in the periodic modulation of the acoustic and acousto-optical properties. This topic has been extensively investigated in the past [18; 30; 37; 85; 120] and has recently regained a significant interest due to possible generation and detection of high frequency coherent acoustic waves using femtosecond laser pulses [28; 46; 131; 134]. Applications in vibrational spectroscopy, nanoscale imaging of defects and picosecond modulation of semiconductor optoelectronic properties are targeted. In particular, a strong effort is devoted to the enhancement of the acousto-optic transduction efficiency in these devices using optical resonances. Most of the published works report Raman scattering by folded acoustic phonons recorded under non-resonant excitation conditions [30; 85], i.e. with probe energies far from specific optical transitions of the system. These results were fairly well explained using the Photoelastic Model (PEM) which assumes a periodic step-like variation of the Photoelastic coefficients along the SL axis: inside each layer the photoelastic coefficients are constant and their values in the bulk materials are used [37]. This model does not take into account explicitly neither the size dependence of the photoelastic coefficients, nor the changes in the spatial dependence of the photoelastic coefficient due to the electronic confinement. Therefore, it fails to describe the resonance behaviour of the Raman-Brillouin scattering due to folded acoustic phonons.

Since the work of Colvard *et al.* [37] and Merlin *et al.* [120], it has been shown that resonant Raman-Brillouin scattering by folded acoustic phonons in semiconductor SLs can be properly interpreted using quantum mechanics: the inelastic light scattering process is described within a third order perturbation theory in which the resonantly excited optical transitions are taken into account explicitly. The acousto-optical interaction is mediated by the electronic states of the system owing to the electron-phonon and electron-photon interactions [159; 194]. Therefore, the resonant Raman-Brillouin spectra strongly reflect the electronic states selected by the optical excitation. In particular, the adequacy between the symmetry of the acoustic displacement field and that of the intermediate electronic states determines the Raman selection rules. However, when several electronic transitions are involved in the resonant light scattering process, interpretation of the Raman-Brillouin features becomes difficult due to interferences between the different scattering paths [64]. Moreover, the SL/substrate interface, the sample surface [109; 110], the thickness fluctuations of the SL layers [21; 158; 160], and the presence of impurities may strongly affect the electronic states thus reflecting in the resonant Raman-Brillouin spectra. For these reasons, the relationship between the electronic properties of a system and its resonant Raman-Brillouin spectra can be very complex.

In a first chapter, a new concept of Raman-Brillouin electronic density [80] is introduced as a theoretical tool for the interpretation of the Raman-Brillouin scattering measurements. It is applied to a simple system consisting on a freestanding silicon membrane [128]. A second chapter is devoted to the extension of this approach to more complex nanostructures consisting in GaAs/AlAs superlattices [98].

Chapter 1

Raman-Brillouin Scattering: Basics

Contents

Raman and Brillouin scattering are inelastic scattering processes in which the wavelength of the scattered radiation is different from that of the incident light and a change in the internal energy of the scattering medium occurs [25; 30]. The two processes exhibit a range of similarities and differences in the properties of the scattering process as well as in the materials that are involved. In the litterature, “Raman scattering” is often used as a generic term for both Raman and Brillouin scattering. In the following I will use the term “Raman-Brillouin”.

1.1 Raman-Brillouin scattering process

1.1.1 Principle

Light-matter interaction can be described by quantum mechanics in the framework of the perturbation theory (cf. Section 2.1). Order 0 event corresponds to the propagation of an electromagnetic radiation (i.e. photon) without interaction (Figure 1.1a). Fermi's golden rule gives the transition rates between eigenstates, and is the first order of the perturbation theory. These transitions correspond to one-step absorption or emission of a photon by creation or anihilation of an electron-hole pair (Figure 1.1b). If the photo-excited electron-hole pair scatters elastically, for instance by impurities or defects before recombining, then the light scattering process is energy conserving and is called Rayleigh scattering (Thomson scattering in the case of free charged particles) (Figure 1.1c). The scattered photon wavevector satisfies both $\vec{k}_s \neq \vec{k}_i$ and $|\vec{k}_s| = |\vec{k}_i|$. This optical process is the order 2 of the perturbation theory.

Light is inelastically scattered (order 3) when there is some energy and wavevector transfers from the electron bath to the phonon bath (e.g. creation or anihilation of vibrations): $E_s \neq E_i$. In such case, the inelastic scattering process is called Raman-Brillouin scattering (Figure 1.1d).

The inelastically scattered light contains frequencies different from those of the excitation source. Those new components are shifted to lower and higher frequencies and are called Stokes and anti-Stokes Raman-Brillouin components, respectively. Raman-Brillouin scattering can be understood using the energy level diagrams shown in Figure 1.2. Stokes Raman-Brillouin scattering consists of a virtual transition from a valence state $|v\rangle$ to a conduction state $|c'\rangle$ (blue arrow), a non-radiative transition from the electronic state $|c'\rangle$ to the electronic state $|c\rangle$ leading to the emission of a phonon of energy $\hbar\omega_{phn}$ (gray arrow), and finally the emission of a scattered photon with the transition from $|c\rangle$ to $|v\rangle$ (black arrow). Anti-Stokes Raman-Brillouin scattering entails a virtual transition from a valence state $|v\rangle$ to a conduction state $|c\rangle$ and the absorption of a phonon of energy $\hbar\omega_{phn}$ during the process. The anti-Stokes lines are typically much weaker than the Stokes lines due to contribution of both stimulated and spontaneous Raman-Brillouin scattering in Stokes process. The phonon population factor for the anti-Stokes process is given by Bose-Einstein distribution $n(\omega_{phn}) = [1 + \exp(\hbar\omega_{phn}/k_B T)]^{-1}$, where ω_{phn} is the frequency of the phonon, k_B is the Boltzmann factor and T is the temperature. For the Stokes process the phonon population factor is given by $n(\omega_{phn}) + 1$.

1.1.2 Models

Two main approaches are used for the interpretation and calculation of the Raman-Brillouin scattering by acoustic phonon in nanostructures. First, the well-known Photoelastic model [135] (PEM) assumes a modulation of the bulk material optical properties by acoustic vibrations through photoelastic coefficients, also known as Pockels coeffi-

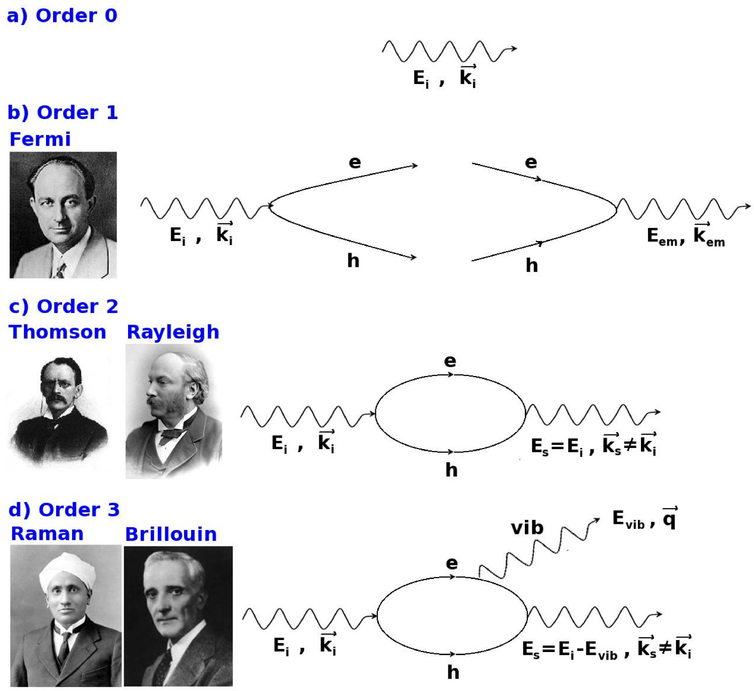

Figure 1.1: Optical processes: a) Order 0: Propagation of light in a medium i, with energy E_i, and momentum $\vec{k}_i$; b) Order 1: Absorption or emission of light creating or anihiling an electron e-hole h pair. Enrico Fermi (1901-1954); c) Order 2: Elastic light scattering producing photons with scattered energy E_s equal to E_i, but momentum $\vec{k}_s$ different to $\vec{k}_i$. Sir Joseph John Thomson (1856-1940) and Lord John William Strutt Rayleigh (1842-1919); d) Order 3: Inelastic light scattering by the vibrations where energy E_s of the scattered photon is reduced by the energy of the vibration E_{vib}. Sir Chandrashekhara Venkata Râman (1888-1970) and Léon Brillouin (1889-1969).

cients [148]. It was initially developed for the interpretation of Brillouin scattering in bulk materials. It has been further extended to two-dimensional structures [30] (superlattices, cavities, membranes). The PEM is very useful for studying acoustic cavity effects as shown by Giehler *et al.* [64] and Fainstein *et al.* [57]. Acoustic confinement in semiconductor membranes (tens of nanometers thick) has been also pointed out recently by Sotomayor *et al.* [172] using a detailed comparison between Raman-Brillouin scattering measurements and PEM simulations. In the PEM only the acoustic vibrations are modified by reflections and transmissions at interfaces and surfaces. The electronic structure is taken into account only through the spatial variation of the Photoelastic coefficients (which are material dependent). Optical cavity effects have also been introduced in some

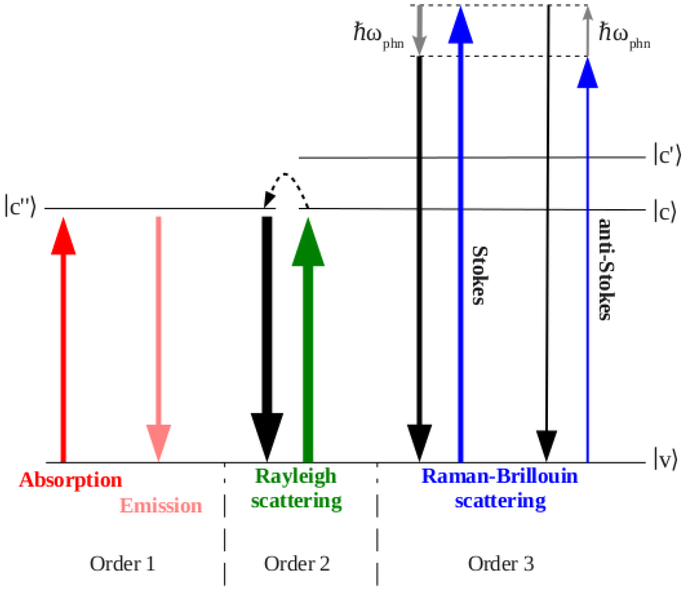

Figure 1.2: Energy level diagrams showing the three orders of an optical process: Absorption/Emission, Rayleigh scattering and non-resonant (anti-)Stokes Raman-Brillouin scattering. The width of the arrows indicates the relative importance of the different optical processes. $|v\rangle$, $|c\rangle$, $|c'\rangle$, and $|c''\rangle$ are valence and conduction electronic states, respectively.

cases [57; 172]. The PEM is valid for excitation energy far from any electronic transition (i.e. out of resonance). It is worthwhile to mention that the PEM is widely used also for the interpretation of the acoustic phonon echos observed in time-resolved pump-probe experiments [47; 118; 179]. The conclusions of the present work are mainly concerned with Raman-Brillouin scattering but they apply to the time-modulation of the optical properties as well.

The second way of calculating the Raman-Brillouin efficiency is based on a quantum mechanical description of the light scattering. The latter is a three step process: incident photon absorption, phonon emission (or absorption), and scattered photon emission. The electronic states play the role of intermediate states in the sense that the photon-phonon interaction is not direct, but occurs via electron-photon and electron-phonon interactions. Unlike in the PEM, in the Raman-Brillouin Quantum Model (RBQM) the electronic energies and wave functions are considered explicitly. This model has been successfully used for the simulation of resonantly excited Raman-Brillouin spectra, i.e. when the light scattering properties are determined by the electronic structure.

First studies of acoustic phonon scattering due to electronic wave-function localization were reported by Kop'ev *et al.* [90] and Sapega *et al.* [159] in GaAs/AlAs multiple quantum wells. In these structures, the electronic transitions were inhomogeneously broadened leading to resonant selection of localized electron and hole wave functions of individual quantum wells. Because of the spatial localization of the intermediate electronic states the wave vector exchanged during the scattering process is no longer transferred to a unique vibration mode but to all modes of the Brillouin zone. As a consequence, the spectral shape of the acoustic phonon Raman-Brillouin scattering reflects the spatial distribution of the excited electronic density[127]. The RBQM has been used to extract characteristic features of the electronic states such as localization and correlation lengths. These basic ideas have been recently extended to semiconductor quantum dots to include three-dimensional confinement effects[169] and spatial ordering effects[32; 33; 52; 79; 123; 124] .

Despite the fact that the PEM and RBQM were extensively used for the interpretation of the Raman-Brillouin measurements, the connection between both models still needs to be clarified. This is particularly important for the interpretation of experiments performed close to resonance, for which the validity of the PEM becomes questionable. On the other hand, under resonant excitation, only a few intermediate electronic states are responsible for the light scattering and therefore those are the main ones contributing to the RBQM. Out of (or close to) resonance, this approximation is no longer valid and the whole density of electronic states should be included in the RBQM. This is also the case when the energy separation between electronic states is smaller than the homogeneous broadening of the resonant optical transitions.

1.2 Acoustic vibrations

The acoustic vibrations can be described in the framework of elasticity theory [112] assuming a continuous elastic medium. This assumption is valid when the vibration wavelength is much larger than the inter-atomic distance. The displacement field $\vec{u}$ is then given by

$$\rho \frac{\partial^2 \vec{u}}{\partial t^2} = (\lambda + 2\mu)\, \overrightarrow{\mathrm{grad}}\,(\mathrm{div}\ \vec{u}) - \mu\ \overrightarrow{\mathrm{rot}}\left(\overrightarrow{\mathrm{rot}}\ \vec{u}\right). \tag{1.1}$$

Equation 1.1 is the Navier-Stokes' equation and gives the displacement $\vec{u}$. ρ is the density, and λ and μ are known as Lamé coefficients of the considered medium [112]. This equation allows to introduce the longitudinal v_L and transverse v_T sound velocities:

$$v_L = \sqrt{\frac{\lambda + 2\mu}{\rho}} \tag{1.2a}$$

$$v_T = \sqrt{\frac{\mu}{\rho}}. \tag{1.2b}$$

The displacement field of the acoustic vibrations can also be described in quantum mechanics using the second quantization theory. In such approach, the acoustic vibrations are described as a sum of harmonic oscillators. For an infinite medium, the eigenmodes are given by

$$\widehat{\vec{u}}_m(\vec{r}, t) = \sqrt{\frac{\hbar}{2\rho V \omega_m}} \epsilon_{\omega_m, \vec{k}_m} \left(\widehat{b}_{\omega_m, \vec{k}_m} e^{-i\vec{k}_m \vec{r}} + \widehat{b^+}_{\omega_m, \vec{k}_m} e^{i\vec{k}_m \vec{r}} \right), \tag{1.3}$$

where V is the volume of the medium, $\widehat{b}_{\omega_m, \vec{k}_m}$ and $\widehat{b^+}_{\omega_m, \vec{k}_m}$ are the vibration annihilation and creation operators, and $\epsilon_{\omega_m, \vec{k}_m}$ is the polarisation of the vibrations. ω_m and $\vec{k}_m$ are the frequency and the wavevector, respectively of the vibration mode m. The factor $\sqrt{\hbar/(2\rho V \omega_m)}$ ensures the normalization of the vibration mode to the energy $\hbar\omega_m$.

1.3 Electronic structure

In Raman-Brillouin scattering, the electronic states play an intermediate role in the scattering process (cf. Figures 1.1 and 1.2). Therefore, it is important to correctly describe the electronic structure of the materials.

Band structure derives from the diffraction of the quantum mechanical electron waves in a periodic crystal lattice with a specific crystal system and Bravais lattice [87] and determines several characteristics, in particular the material's electronic and optical properties.

Several methods allow to calculate the electronic band structure of materials such as (i) the $k \cdot p$ method based on the perturbation theory [194], (ii) the nearly-free electron model [87], (iii) the tight binding method [194], (iv) the density functional theory (DFT) [53], or (v) Ab-initio quantum chemistry methods.

Figure 1.3 shows the electronic band structure of bulk silicon. Its indirect band gap is E_g =1.1242 eV [20] at room temperature, and the direct band gaps are E_0' =3.4 eV and E_0 =4.2 eV [31; 147].

Figure 1.4 shows the electronic band structures of two III-V semiconductor compounds: Gallium Arsenide (GaAs, Figure 1.4a) and Aluminium Arsenide (AlAs, Fig-

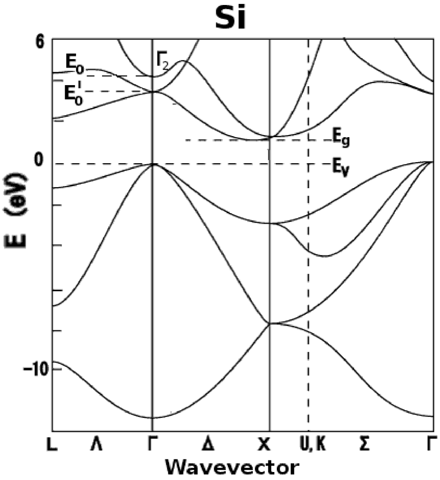

Figure 1.3: Electronic band diagram of silicon. It includes the L, Λ, Γ, Δ, X, U, K, and Σ symmetry points in the reciprocal space. E_0', E_0 and E_g are the two direct and the indirect band gaps, respectively, and E_v indicates the top of the valence band.

ure 1.4b). Contrary to silicon, GaAs has a direct band gap (Γ point in the reciprocal space) of $E_0 = E_g$ =1.424 eV [20] while AlAs is also an indirect band gap material with a gap (X point) of E_g =2.153 eV [20]. The direct gap of AlAs (Γ point) is E_0 =3.02 eV [20]. Electronic properties of GaAs/A1As short-period superlattices have been studied by Daran *et al* [43].

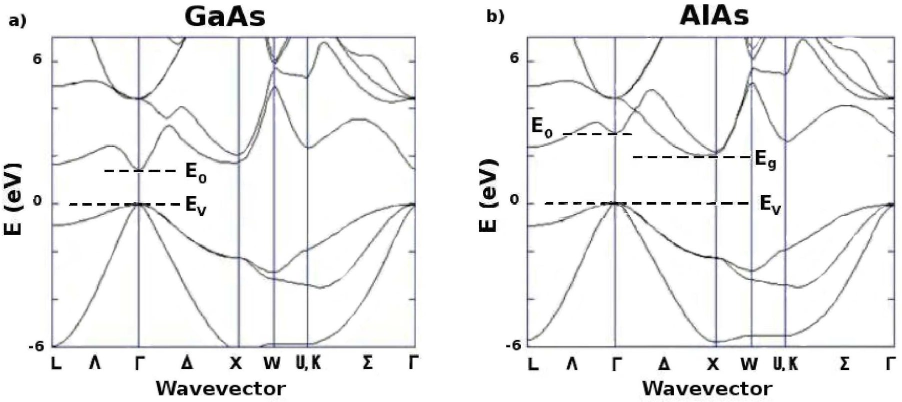

Figure 1.4: Electronic band diagrams of GaAs (a) and AlAs (b). It includes the L, Λ, Γ, Δ, X, W, U, K, and Σ symmetry points in the reciprocal space. E_0 and E_g are the direct and the indirect band gaps, respectively.

Chapter 2

Raman-Brillouin Electronic Density in Thin Films and Membranes

Contents

In order to understand and interpret Raman-Brillouin scattering spectra, it is important to correctly describe the interaction between the electronic states and the acoustic vibrations involved in the scattering process. Figure 2.1 shows experimental Raman-Brillouin spectra of a thin Silicon-On-Insulator (SOI) membrane [172]. These spectra show well-defined scattering by acoustic vibrations confined into the silicon layer (sketched in Figure 2.2).

In this chapter I present calculations of Raman-Brillouin scattering using both the PEM and RBQM in the case of freestanding silicon films with the aim of understanding the experimental spectra shown in Figure 2.1. The main points addressed in this chapter

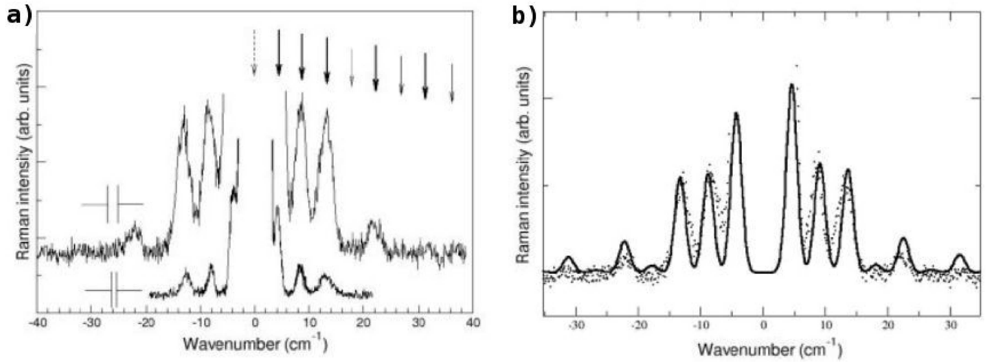

Figure 2.1: (a) Experimental Raman-Brillouin spectra of a 32.5 nm thick SOI membrane for two different resolutions. (b) Experimental Raman-Brillouin spectrum (dots) compared to PEM simulation (black line). Figures taken from Reference [172].

are: i) the dependence of the Raman-Brillouin spectra simulated with the RBQM on the optical excitation energy (resonance effects), ii) the comparison between the results of the Photoelastic model and the Raman-Brillouin Quantum model, iii) the validity of the step-like profile of the photoelastic constant used in the PEM.

2.1 Raman-Brillouin electronic density formalism

In this section I briefly recall the RBQM (Chapter 1) and introduce the effective Raman-Brillouin electronic density for a free standing quantum film (cf. Figure 2.2) [128].

2.1.1 Raman-Brillouin quantum model

When the scattering process occurs at the conduction band, i.e. when the scatterers are the electons, the Raman-Brillouin scattering rate is given by:

$$\mathcal{P}(\vec{k}_i, \vec{k}_s, \vec{k}_m) = \frac{2\pi}{\hbar} \left| \sum_{e,e',h} \frac{\langle h| H^s_{e-pht} |e'\rangle \langle e'| H_{e-vib} |e\rangle \langle e| H^i_{e-pht} |h\rangle}{(E_s - E_{e'-h} + i\gamma_{e'-h})(E_i - E_{e-h} + i\gamma_{e-h})} \right|^2 \delta(E_s \pm \hbar\omega_m - E_i), \tag{2.1}$$

where e, e', and h' are electron and hole eigenstates; E_{e-h} and γ_{e-h} are the energy and the homogeneous line width of the $e - h$ transition, respectively; E_{e-h} is defined as: $E_{e-h} = E_0 + E_e + E_h$ where E_0 is the bulk direct band gap and E_e (resp. E_h) is the electron (resp. hole) confinement energy. E_i and $E_s = E_i \pm \hbar\omega_m$ are respectively the

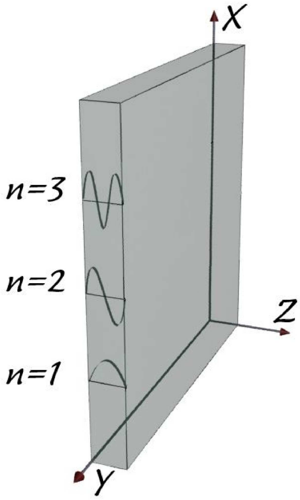

Figure 2.2: Sketch of Si membrane showing the first three confined electronic states (n =1, 2, and 3) along the z-direction. The membrane is considered to be infinite along the x- and y-directions.

incident and scattered photon energies, $\hbar\omega_m$ being the energy of the absorbed or emitted vibration mode m of frequency ω_m. H_{e-pht} and H_{e-vib} are the electron-photon and electron-vibration interaction Hamiltonians, respectively. A second contribution to the scattering rate is given by the scattering by the holes where the initial and final eigenstates are now e and the intermediate eigenstates are h and h'. Both contributions are taken into account the following. The Raman-Brillouin intensity measured by an experimental setup is then given by the non-coherent summation of all the contributions over the Brillouin zone (BZ):

$$I_{RB}(\omega_i,\omega_s) = \int_{BZ} \mathcal{P}(\vec{k}_i,\vec{k}_s,\vec{k}_m) g(\omega_m) d\omega_m, \tag{2.2}$$

where $g(\omega_m)$ is the density of vibration modes.

The conduction states e and e' and valence states h can be described by Bloch wavefunctions $\psi_{e(h)}(\vec{r}) = u_{c(v)}(\vec{r})\phi(\vec{r})$ where $u_{c(v)}(\vec{r})$ are the atomic-like wavefunctions and $\phi(\vec{r})$ the slowly varying envelope functions.

For the sake of simplicity, I consider here only zero in-plane wavevector electron-hole transitions. This restriction allows to discuss the relation between PEM and RBQM with simplified notations and without loss of generality. It must be however reconsidered for a detailed comparison with experiments.

Assuming that electrons and holes are perfectly confined within the film, the envelope wavefunctions are given by the Krönig-Penney model for thick barriers (i.e. infinite quantum well approximation) [87; 91]

$$\phi_{n_z}(z) = \sqrt{\frac{2}{L_z}} \sin\left(\frac{n_z \pi z}{L_z}\right), \tag{2.3}$$

where n_z is an integer and $L_z \ll L_x, L_y$ is the film thickness. The first four confined electronic states of the membrane $\Psi_{k_x,k_y,n_z} = \phi_{k_x}\phi_{k_y}\phi_{n_z}$ are plotted in the (y, z) plane in Figure 2.3 and sketched in Figure 2.2. Wavefunctions along x- and y-directions $\phi_{k_{x(y)}}$ are planewaves of wavevectors $k_{x(y)}$.

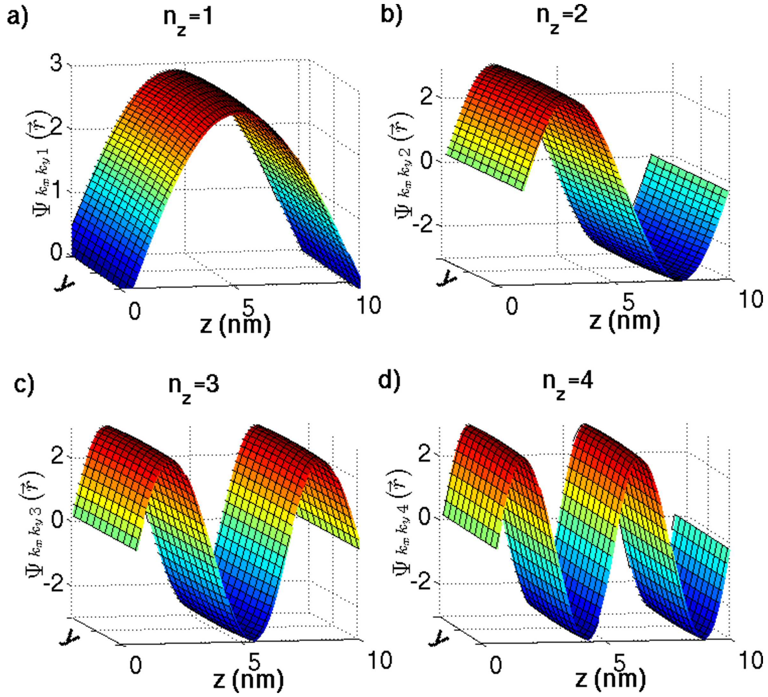

Figure 2.3: First four envelope wavefunctions (n_z =1, 2, 3, and 4) of a L_z = 10 nm, $L_x = L_y = 1000$ nm silicon thin film plotted in the (y, z) plane. $n_x = n_y = 1$.

Using the parabolic band approximation to describe the electronic structure at the center of the Brillouin zone (Γ point, Figure 1.3), the electron (resp. hole) confinement energy is:

$$E_{e(h)}^{n_z} = \frac{\hbar^2\pi^2}{2m_{e(h)}}\frac{{n_z}^2}{L_z^2}, \tag{2.4}$$

where m_e and m_h are respectively the electron and hole effective masses used in the

Table 2.1: Longitudinal sound velocity v_L, density ρ, deformation potentials of the conduction D_c and valence (averaged potential) D_v bands, and electron and hole effective masses m_e/m_0, and m_h/m_0 of silicon [67; 168]

v_L (m.s^{-1})	ρ (kg.m^{-3})	D_c (eV)	D_v (eV)	m_e/m_0	m_h/m_0
8430	2329	-2.46	2.0	0.28	0.49

calculations (cf. Table 2.1). Moreover, the bulk direct band gap of silicon is $E_0 = 4.2$ eV. It corresponds to direct transitions from the top of the valence band to the Γ_2 conduction band minimum [31; 147]. For this transition the parabolic band approximation is valid at least around the Γ_2 point (cf. Figure 1.3). Obviously, the confinement energies of electrons and holes in very thin silicon layers are overestimated by the parabolic band approximation (cf. Figure 1.3).

The electron-photon interaction Hamiltonian is given by

$$H_{e-pht}^{i(s)} = \frac{q\vec{p} \cdot \vec{A}_{i(s)}}{m_e}, \tag{2.5}$$

$\vec{p}$ being the momentum of the electron, q is the charge of the electron, and $\vec{A}_{i(s)}$ the vector potential of the incident (resp. scattered) radiations. We assume deformation-potential (DP) electron-vibration interaction involving longitudinal acoustic (LA) vibrations. Thus the electron-vibration Hamiltonian, acting on the envelope wavefunctions, reads $H_{e-vib} = D_{c(v)}\mathrm{div}\ \vec{u}$, where $\vec{u}$ is the displacement vector, and $D_{c(v)}$ is the conduction (resp. averaged valence) band deformation potential energy (cf. Table 2.1). Using stress-free boundary conditions at the film surfaces, the displacement field of confined LA vibrations along the z-direction is given by

$$u_m(z) = \sqrt{\frac{\hbar}{2\rho V \omega_m}} \cos\left(\frac{m\pi z}{L_z}\right), \tag{2.6}$$

where ρ and V are the mass density and film volume within the cell, respectively. The frequency of LA phonons, ω_{vib}, assuming a linear dispersion, is proportional to the longitudinal sound velocity v_L and the phonon wavevector $k_m = \pi\frac{m}{L_z}$, as $\omega_{vib} = \omega_m = v_L k_m$ (where m is an integer labeling the vibration mode).

When only one intermediate electronic state is resonantly excited by the probe light, the sum of scattering amplitudes (Equation 2.1) can be limited to one term; the off-resonance terms can be neglected. In that case the Raman-Brillouin peak positions and intensities are directly related to the spatial distribution of the electronic density selected by the optical excitation. Otherwise, one has to sum a large number of terms which leads to strong interference effects in the overall scattering efficiency. Therefore, the characteristics of the Raman-Brillouin spectra can hardly be related to characteristic features of the excited electronic states.

In order to overcome this difficulty, the Raman-Brillouin scattering rate (Equation 2.1) can be rewritten introducing a Raman-Brillouin electronic density defined as [80; 128]

$$\rho_{RB}(E_i, E_s, z) = \frac{1}{\mathcal{R}(E_i, E_s)} \sum_{e,e',h} R^s_{h,e'}(E_s)\phi^*_{e'}(z) R^i_{e,h}(E_i)\phi_e(z), \tag{2.7}$$

where $R^{i(s)}_{e,h}(E_{i(s)})$ is a dimensionless resonance factor given by

$$R^{i(s)}_{e,h}(E) = \frac{\langle e|\, H^{i(s)}_{e-pht}\, |h\rangle}{E_{i(s)} - E_{e-h} + i\gamma_{e-h}} \tag{2.8}$$

and

$$\mathcal{R}(E_i, E_s) = \sum_{e,h} R^s_{h,e}(E_s) R^i_{e,h}(E_i) \tag{2.9}$$

is a normalization factor satisfying $\int \rho_{RB}(z)dz = 1$.

$\rho_{RB}(z)$ is determined by the sum over the initial hole states of the overlapping between the effective electronic state $\sum_e R^i_{e,h}(E_i)\phi_e(z)$ excited at the probe laser energy E_i, and the effective electronic state $\sum_{e'} R^s_{h,e'}(E_s)\phi_{e'}(z)$ giving rise to emission of a scattered photon at energy $E_s = E_i \pm \hbar\omega_{vib}$; $\rho_{RB}(z)$ has real and imaginary contributions because of the homogeneous broadening of the electron-hole transitions (Equation 2.8). Using Equation 2.7, Equation 2.1 becomes

$$\mathcal{P}(\vec{k}_i, \vec{k}_s, \vec{k}_m) = \frac{2\pi}{\hbar} \left| \mathcal{R}(E_i, E_s) D_c \int \rho_{RB}(z) \frac{\partial u_m(z)}{\partial z} dz \right|^2 \delta(E_s \pm \hbar\omega_m - E_i). \tag{2.10}$$

From Equation 2.10, it can be noticed that $\rho_{RB}(z)$ is the electronic density distribution that interacts with the vibration field and is responsible for the Raman-Brillouin scattering.

Strictly speaking Equation 2.10 does not contain new physics with respect to Equation 2.1 in the sense that both equations are equivalent. However, using Equation 2.10, it is possible to plot an electronic density distribution which is directly connected to characteristic features of the Raman-Brillouin spectra, although many electronic states are involved in the light scattering.

2.1.2 Photoelastic model

In the Photoelastic model, the Raman-Brillouin scattering efficiency by LA vibrations is given by

$$\mathcal{P}(\vec{k}_i, \vec{k}_s, \vec{k}_m) = \frac{2\pi}{\hbar} \left| \int \vec{A}_s^*(z)\vec{A}_i(z)P(z)\frac{\partial u_m(z)}{\partial z}dz \right|^2 \delta(E_s \pm \hbar\omega_m - E_i), \tag{2.11}$$

where $P(z)$ is the spatial variation of the photoelastic coefficient, and $\vec{A}_i$ (resp. $\vec{A}_s$) is the incident (resp. scattered) photon field.

In order to introduce the spatial variation of the incident and scattered photon fields in a simple way, we can assume (for both PEM and RBQM) that $A_{i(s)}(z)$ is of the form $\cos\left[k_{i(s)}(z - L_z/2)\right]$, $k_{i(s)}$ being the incident or scattered photon wavevector component along the z-direction. The in-plane component of the incident and scattered wavevectors can be neglected in the backscattering configuration (excitation and detection along the z-direction). Optical cavity effects, due to reflections at the material/air interfaces, may play an important role because the symmetry of the electromagnetic fields inside the layer is responsible for a selection of the confined vibration modes that gives rise to Raman-Brillouin scattering. Although important for the interpretation of experimental data, such effects are not addressed in this chapter. Moreover, with the form adopted for $A_{i(s)}(z)$ (standing waves) the backward and forward scattering configurations are equivalent.

Here, because the system consists of a single two-dimensional layer (cf. Figure 2.2), $P(z)$ is taken as a rectangular function. The photoelastic coefficient is constant inside the layer and zero outside. In the following I will refer to this $P(z)$ profile as a “step-like” profile. In that case, the wavevector conservation law breaks down (along the z-direction) and all acoustic vibration modes become allowed. Their Raman activity depends on their symmetry (with respect to the middle of the layer) and on the electromagnetic fields inside the layer (cf. Equation 2.11).

2.2 Results and discussion

2.2.1 Construction of the Raman-Brillouin electronic density

Figure 2.4 shows the spatial distribution of the RBED calculated using Equation 2.7 for a film thickness $L_z = 10$ nm. Since I am interested in studying the change of the Raman-Brillouin scattering around the fundamental electronic transition, $\rho_{RB}(z)$ was generated using the first fifteen electron and first fifteen hole states. A homogeneous broadening

$\gamma_{e-h} = 25$ meV (thermal broadening at room temperature) was used for all transitions. The RBED shown in Figure 2.4 was calculated for various values of the detuning between the incident photon energy and the fundamental electron-hole transition; the detuning is defined as: $\delta = E_i - (E_0 + E_e^1 + E_h^1)$ where E_e^1 (resp. E_h^1) is the confinement energy of the fundamental electron (resp. hole) state. A reduced detuning $\delta' = \delta/(E_e^1 + E_h^1)$ and a reduced broadening $\gamma' = \gamma_{e-h}/(E_e^1 + E_h^1)$ are also defined.

The scattered photon energy is fixed at the Stokes value $E_s = E_i - \hbar\omega_1$ corresponding to emission of the first confined acoustic vibration mode.

Because $\hbar\omega_{vib} \ll \gamma_{e-h}$, in-coming and out-going resonances occur simultaneously, and the RBED is rather independent of the acoustic vibration energy (this point will be reconsidered later on).

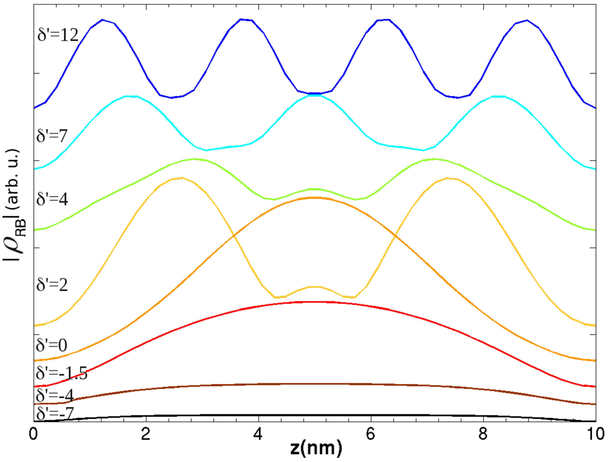

Figure 2.4: Modulus of the Raman-Brillouin electronic density along the z-axis of a 10 nm thick layer, for reduced detuning ranging from $\delta' = -7$ to $\delta' = 12$. The reduced homogeneous broadening is $\gamma' = \gamma_{e-h}/(E_e^1 + E_h^1) = 1.2$. The plots were shifted vertically for clarity: the origin being at $z = 0$.

For excitation well below the fundamental electron-hole transition ($\delta' = -7$ and -4) , the RBED distribution within the layer is quasi-uniform (i.e. constant except in the vicinity of the film surfaces). In this situation (far from resonance), there is no selection of a particular transition. Close to resonance ($\delta' = -1.5$), the contribution of the first confined electron-hole transition emerges and becomes dominant for resonant excitation ($\delta' = 0$). Higher energy confined transitions come into resonance, for $\delta' = 2$, 7 and 12, and give rise to strong oscillations of the RBED.

Figure 2.5 shows resonance profiles calculated according to Equation 2.9 for three

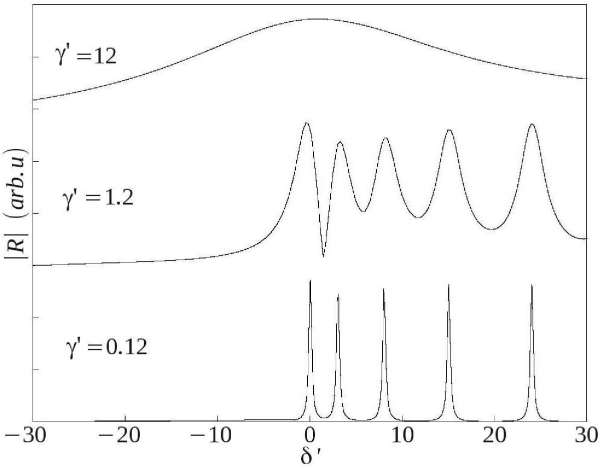

Figure 2.5: Raman-Brillouin intensity as a function of the detuning δ' for a 10 nm thick layer. Resonance profiles are shown for homogeneous broadening $\gamma = 2.5$ meV ($\gamma' = 0.12$), 25 meV ($\gamma' = 1.2$) and 250 meV ($\gamma' = 12$).

values of the reduced homogeneous broadening $\gamma' = \gamma_{e-h}/(E_e^1 + E_h^1)$. For rather small homogeneous broadening ($\gamma' = 0.12$ and 1.2) resonance peaks occur at each confined electron-hole transition: the selection of a given transition by the optical excitation is very efficient and the light scattering is mediated by the corresponding electron and hole states. For larger homogeneous broadening ($\gamma' = 12$), many electron-hole transitions are excited leading to interferences between different scattering paths: the low-energy tail (negative detuning in Figure 2.5) is due to the resonance effect and also to the fact that, for negative detuning, all scattering amplitudes have nearly the same phase (that of the optical excitation). In that case, the interferences between the different scattering amplitudes (terms of the summation in Equation 2.7) are constructive. Whereas, for positive and large detuning ($\delta' \gg 1$) some scattering amplitudes have a positive phase and others a negative phase depending on whether the energy of the excited (and detected) electron-hole transition is larger or smaller than the excitation energy. As a consequence, the scattered intensity falls down for positive detuning due to destructive interference between all scattering amplitudes.

Figure 2.6 shows the construction of the Raman-Brillouin electronic density for $\delta' = -7$ and $\gamma' = 1.2$ (plotted in Figure 2.4). The number n for electron and hole states is increased from 1 to 15.

It can be noticed that even for excitation well below ($\delta' = -7$) the fundamental electron-hole transition, high energy transitions play an important role in the construction of the RBED (i.e. in the scattering process). For instance, the maximum value of the RBED reaches only 91 percent of its final value (inset of Figure. 2.6) when including 3 electron and 3 hole states. The convergence curves and the plots in Figure 2.6 show that the RBED tends to be quasi-uniform and does not evolve once 10 electron and 10 hole states are taken into account.

As can be noticed, the convergence of the RBED is very rapid. This allows generating Raman-Brillouin spectra, within a reasonable computation time, even for large systems.

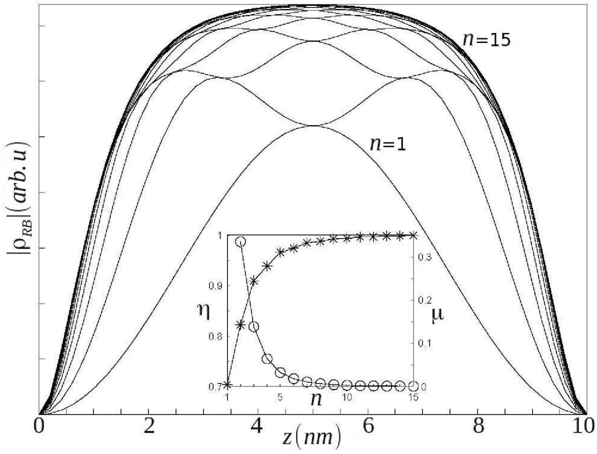

Figure 2.6: Construction of the RBED for $\delta' = -7$ (excitation below the fundamental optical resonance) and $\gamma' = 1.2$. n is the number of electron and the number of hole states used in the calculations. Starting from the lowest plot $n = 1$ (one electron and one hole states), n is increased up to 15. The inset shows convergence curves defined as $\mu = ||\rho^{n}_{RB,max}| - |\rho^{n-1}_{RB,max}||/|\rho^{n}_{RB,max}|$ (circles) and $\eta = 1 - ||\rho^{15}_{RB,max}| - |\rho^{n}_{RB,max}||/|\rho^{15}_{RB,max}|$ (stars).

From Equation 2.7 it is evident that the RBED has a real part and an imaginary part; the latter is due to the homogeneous broadening of the electronic transitions. For $\delta' = -7$ and $\gamma' = 1.2$ the imaginary part of the RBED is rather small in comparison with the real part. It however, increases when approaching the resonance and has a noticeable influence on the spatial distribution of $|\rho_{RB}(z)|$.

2.2.2 Size dependence of the RBED

The lower panel in Figure 2.7 shows the spatial distribution of the RBED along the z-axis for various layer thicknesses L_z. The excitation energy E_i and homogeneous broadening γ are fixed at 4.075 eV and 25 meV, respectively. In that case, the reduced detuning δ' and homogeneous broadening γ' depend on the layer thickness as indicated in the figure caption. For very thin layers ($L_z = 2$ nm) both δ' and γ' are small. Then, the fundamental electron-hole transition is efficiently selected by the optical excitation. For this reason the RBED reduces to the density distribution associated with the first confined electron and hole states (Equation 2.3). With increasing layer thickness, the energy separation between the confined electronic states decreases and many transitions come into resonance. This leads to a quasi-uniform distribution of the RBED for $L_z = 10$ and 25 nm as shown in Figures 2.6 and 2.7. However, for $L_z = 100$ nm the RBED oscillates and strongly deviates from a quasi-uniform distribution. In fact, it is the wavevector conservation law that starts to come out with increasing layer thickness.

Indeed, for $k_{i(s)}L_z \ll 1$, i.e. for a layer thickness much smaller than the (incident and scattered) photon wavelength (around 150 nm inside the layer) the electromagnetic fields $A_i(z)$ and $A_s(z)$ are slowly varying functions along the z-axis. Therefore, the electron-photon matrix elements are proportional to the overlapping between the electron and hole wavefunctions. Thus, only electron and hole states having the same envelope wavefunctions are relevant for both the photon absorption and emission steps. As a consequence, the intermediate states e and e' in Equations 2.1 and 2.10 are inevitably the same and the RBED is composed of diagonal matrix elements. The RBED plotted in Figures 2.5 and 2.6 are mainly due to such diagonal contributions ($k_{i(s)}L_z \approx 0.1$). Off-diagonal transitions have been taken into account but are negligible for $L_z \lesssim 10$ nm.

Figure 2.8 shows the spatial distribution of both diagonal and off-diagonal Raman-Brillouin electronic densities. For these plots, E_i and γ are varied so that the reduced detuning and homogeneous broadening are fixed ($\delta' = -7$ and $\gamma' = 1.2$). This allows to compare similar resonance conditions for the different layer thicknesses.

With increasing layer thickness the off-diagonal part of the RBED increases and becomes important for $L_z = 100$ nm (Figure 2.8). Indeed, for a layer thickness comparable to the absorbed and emitted photon wavelengths, $k_{i(s)}L_z \sim 1$, the spatial variation of the electromagnetic fields allows transitions between electron and hole states having different envelope wavefunctions. Therefore, different states e and e' in Equations 2.1 and 2.10 can be involved in the light scattering. In the limit of $k_{i(s)}L_z \gtrsim 1$ the RBED involves only transitions that fulfill the wavevector conservation rule at the electron-photon interaction

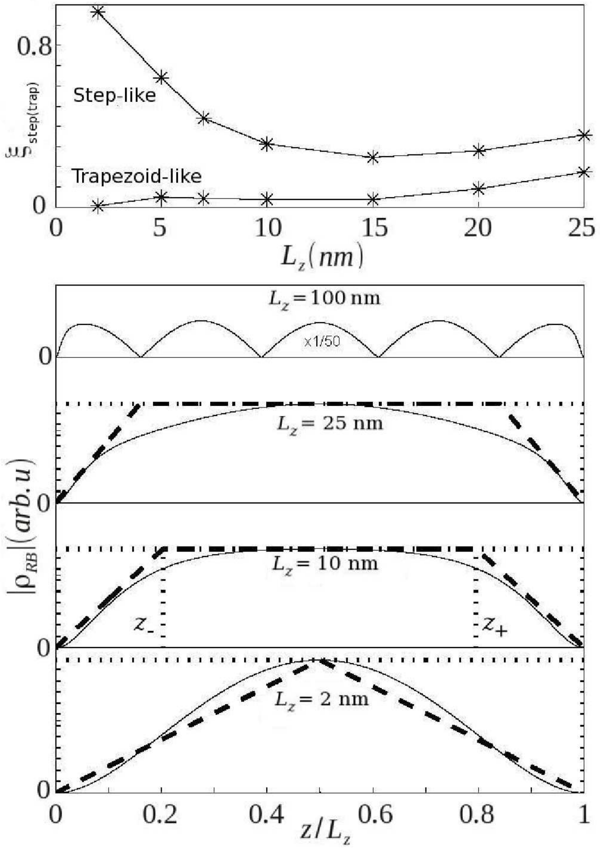

Figure 2.7: Lower panel: Modulus of the RBED along the z-axis for layer thickness ranging from L_z =2 nm to 100 nm. The excitation energy is fixed at $E_i = 4.075$ eV and the homogeneous broadening is $\gamma = 25$ meV. Reduced detuning and homogeneous broadening (δ', γ') are, from bottom to top, (-1.2, 0.05), (-7, 1.2), (-38, 7.4) and (-590, 120). For each L_z are shown the step-like profile (bold dotted line) and the trapezoid-like profile (bold dashed line); z_- and z_+ are the z-coordinates (dashed lines) which define the trapezoid. Upper panel: deviation of the step-like and trapezoid-like profiles from the RBED evaluated as $\xi_{\text{step(trap)}} = |S_{step(trap)} - \int |\rho_{RB}(z)|dz| / \int |\rho_{RB}(z)|dz$.

steps (emission and absorption). In that case states e and e' differ by the exchanged wavevector.

It is interesting to notice that the RBED shown in Figure 2.8 for $L_z = 2$ nm strongly differs from the one plotted in Figure 2.7 for the same layer thickness. The reduced detuning is not the same in these figures. In Figure 2.8 the optical excitation is well below ($\delta' = -7$) the electron-hole transition. It is much larger, in absolute value, than the separation between the confined energy levels. In that case, the resonance factors associated with the different transitions are similar. That is why the RBED tends to be quasi uniform for a very negative detuning.

The study of the RBED distribution shows that the optical transitions giving rise to the light scattering process strongly depends on size effects. This is particularly important for the emission and absorption of vibration modes and for the interpretation of experimental data.

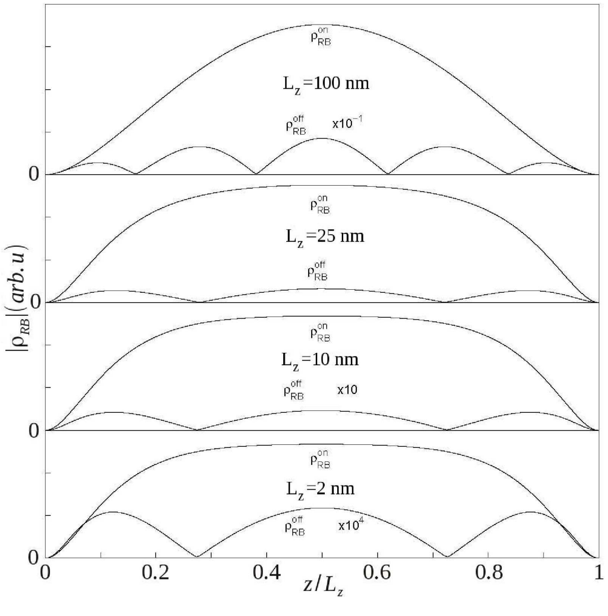

Figure 2.8: Diagonal (ρ_{RB}^{on}) and off-diagonal (ρ_{RB}^{off}) RBED modulus along the z-axis for $L_z = 2$ nm, 10 nm, 25 nm and 100 nm. Detuning and homogeneous broadening are respectively $\delta' = -7$ and $\gamma' = 1.2$

In the photoelastic model a step-like photoelastic coefficient (constant within the layer and zero outside) is usually assumed.

By comparing Equation 2.10 and Equation 2.11 it can be noticed that the product

$A_s^*(z)A_i(z)P(z)$ can be identified with the RBED $\rho_{RB}(z)$. For $k_{i(s)}L_z \ll 1$ (i.e. nano-sized layer thickness), $A_s^*(z)A_i(z)$ is rather constant and thus it is mainly the photoelastic coefficient profile that determines the Raman-Brillouin spectra in the photoelastic model. That is why, in the following, a direct comparison between $\rho_{RB}(z)$ and $P(z)$ is shown.

First, as can be seen in Figure 2.7, the RBED is far from being constant within the layer; it vanishes at the film surfaces because only the first confined transitions significantly contribute to the RBED (Figure 2.6).

In other words, if all transitions could equally contribute to the light scattering, the RBED would approach a step-like profile. This is of course not the case since high energy transitions are far away from the optical excitation, thus leading to very small resonance factors.

The top panel in Figure 2.7 presents a comparison between the RBED distribution, the step-like profile usually adopted for the photoelastic coefficient and a proposed trapezoid-like profile. This comparison is performed for fixed excitation energy ($E_i = 4.075$ eV) and homogeneous broadening ($\gamma = 25$ meV). The parameter used to evaluate the deviation of the RBED from the step-like or from the trapezoid-like profile is defined as:

$$\xi_{\text{step(trap)}} = \frac{\left|S_{\text{step(trap)}} - \int |\rho_{RB}(z)|\, dz\right|}{\int |\rho_{RB}(z)|\, dz}, \tag{2.12}$$

where $S_{\text{step(trap)}}$ is the integral of the step-like (resp. trapezoid-like) profile over the layer thickness. The amplitude of the step-like and trapezoid-like profiles are fixed to the maximum value of the RBED inside the layer (cf. Figure 2.7).

It is clear that the step-like profile shows strong deviations from the RBED for very narrow layers (less than 10 nm). The trapezoid-like profile fits much better the RBED distribution. In other words, by forcing the photoelastic coefficient to vanish at the layer surfaces, the quantum nature of the thin film is, in that artificial way, taken into account (the thin layer is no longer considered simply as a part of a bulk material from the point of view of the optical properties). For $L_z \gtrsim 30$ nm the RBED starts to oscillate (cf. plot for $L_z = 100$ nm in Figure 2.7). It strongly deviates from the step-like and trapezoid-like profiles because the spatial variation of $A_s^*(z)A_i(z)$ is not taken into account when only the photoelastic coefficient is plotted.

Second, by studying the variation of the RBED as a function of L_z it is possible to propose trapezoid-like profiles that fit the RBED for layer thicknesses ranging from 2 nm to 25 nm; the parameters z_- and z_+ defined in Figure 2.7 are $z_- = 0.74$ nm$+0.13L_z$ and $z_+ = -0.74$ nm$+0.87L_z$, where L_z is in nanometers. Notice that for very thin layers ($L_z = 2$ nm in Figure 2.7) the trapezoid-like profile becomes a triangle-like profile and obviously it strongly deviates from a step-like profile. By comparing the RBED distribution with these profiles it clearly appears that, for layer thickness ranging from 2 nm to 25 nm, the proposed trapezoid-like profile is more realistic than the step-like profile usually assumed for the photoelastic coefficient. For larger layer thickness ($L_z \gtrsim$ 25 nm) the deviations of the step-like and trapezoid-like profiles from the RBED indicate that the $A_s^* A_i$ terms should be taken into account, even for L_z about five times smaller than the photon wavelengths.

Finally, strong deviations of the RBED distribution from the step-like and trapezoid-like photoelastic profiles are evident if resonant excitation is considered (cf. Figure 2.4): both profiles are unable to approximate the RBED for excitation close to and above the fundamental electron-hole transition. The PEM, in which a real and dispersion-less photoelastic coefficient is assumed, is valid only for excitation below the fundamental electron-hole transition. That is why the RBQM and PEM are compared for negative δ' in Figure 2.7.

The emission and absorption of acoustic vibrations will now be investigated and the inelastic light scattering spectra simulated using the RBED (quantum model) and the photoelastic model, in which either the step-like or trapezoid-like profile of the of the photoelastic constant is assumed, will be compared.

2.2.3 Simulations of Raman-Brillouin spectra

2.2.3.1 Diagonal/off diagonal contributions

Figure 2.9 presents Raman-Brillouin spectra calculated using Equation 2.10. The peaks in the Stokes and anti-Stokes regions are due to emission and absorption of confined acoustic vibrations (their frequencies scale as the inverse of the layer thickness L_z). For each L_z the spectra simulated with either diagonal or off-diagonal RBED are shown in Figure 2.8. One must however keep in mind that the overall scattered intensity is the coherent sum of the diagonal and off-diagonal contributions.

As mentioned above, for $L_z = 2$ nm, 10 nm and 25 nm the Raman-Brillouin spectra are mainly determined by the diagonal part of the RBED. Off-diagonal RBED contributes only a little to the light scattering. It also means that, for $k_{i(s)} L_z \ll 1$, mainly diagonal electron-vibration matrix elements are responsible for the inelastic light scattering. This can be deduced directly from Equation 2.1 by letting the intermediate states e and e' be the same. With increasing layer thickness off-diagonal electron-vibration matrix elements come out since the excited electronic state e can be different from the one, e', giving rise to the optical emission of the scattered photon. The off-diagonal contribution to the

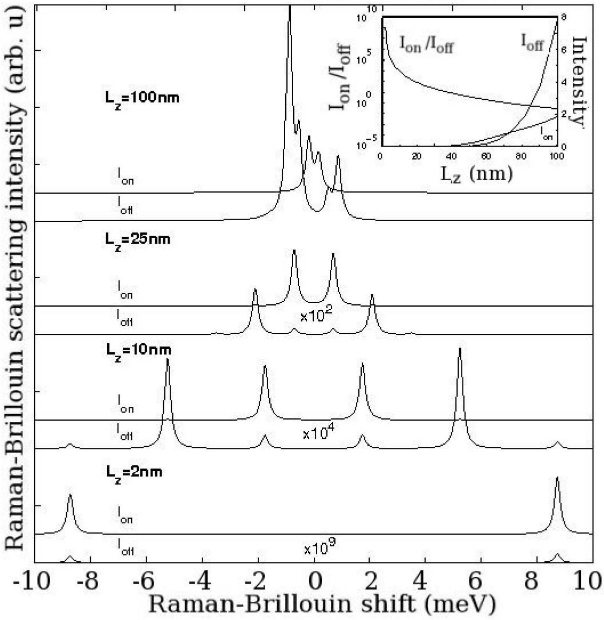

Figure 2.9: Inelastic light scattering spectra simulated according to the Raman-Brillouin quantum model for fixed $\delta' = -7$ and $\gamma' = 1.2$. For each thickness L_z, the scattered intensity has been separated into diagonal (I_{on}) and off-diagonal (I_{off}) contributions. When it is too weak I_{off} has been multiplied by the indicated rescaling factor. Calculations were performed for a limited number of low-frequency confined modes. The inset shows the evolution of I_{on}, I_{off} and $I_{\mathrm{on}}/I_{\mathrm{off}}$ as a function of layer thickness. For these plots the intensities were integrated over the whole spectrum

Raman-Brillouin spectra becomes dominant for $k_{i(s)}L_z \gg 1$ (cf. plots for $L_z = 100$ nm in Figure 2.9). For infinite systems the diagonal contribution is forbidden whereas the off-diagonal contribution gives a single scattered peak: a Brillouin peak located at the acoustic vibration frequency of the wavevector $k_m = k_i - k_s$.

The inset in Figure 2.9 shows the evolution of the diagonal (I_{on}) and off-diagonal (I_{off}) Raman-Brillouin intensities as a function of the layer thickness. These curves are particularly important for analyzing experimental data. Indeed, since the intensity ratios between the Raman-Brillouin lines, due to confined acoustic vibrations, strongly depend on the spatial distribution of the electronic density it is important to evaluate, for a given layer thickness, the relative contributions of diagonal and off-diagonal RBED as both do not have the same spatial distribution (Figure 2.8). From the evolution of I_{on} and I_{off} it can be noticed that for ($L_z \lesssim 30$ nm) the contribution of the off-diagonal RBED to the

Raman-Brillouin scattering can be neglected.

Notice that for $L_z = 25$ nm and 100 nm the anti-Stokes intensity is larger than the Stokes intensity because of the stronger outgoing resonance for the anti-Stokes scattering. As a matter of fact, $\delta' = -7$ and $\gamma' = 1.2$ correspond to detuning $\delta = -1.25$ meV and homogeneous broadening $\gamma = 0.25$ meV for $L_z = 100$ nm. These values indicate that the energy separation between the Stokes and anti-Stokes frequencies is comparable to the detuning and smaller than the homogeneous broadening. In that case strong differences between outgoing resonances in the Stokes and anti-Stokes regions can indeed be expected.

2.2.3.2 Step-like, trapezoid-like and RBED profiles

Figure 2.10 shows the spectra calculated in the framework of the Raman-Brillouin quantum model and of the photoelastic model for a layer thickness $L_z = 10$ nm. The trapezoid-like photoelastic coefficient used in the PEM is the one that fits the RBED for $L_z = 10$ nm (cf. Figure 2.7). Each spectrum was normalized to the intensity of the first low-frequency peak. Some differences in the peak intensity ratios can be noticed. These differences lie in the spatial distribution of the RBED and of the photoelastic coefficient profiles.

As indicated in Figure 2.10, the intensity ratios of the peaks generated with the PEM using either the step-like or the trapezoid-like profile are different. The wavelengths of the lowest frequency peaks associated with the $m = 1$ and $m = 3$ confined modes (cf. Equation 2.6) are comparable to the layer thickness. They are less sensitive to the details of the photoelastic coefficient profile than the vibration modes at higher frequencies. Indeed, the Raman-Brillouin intensities of the high frequency peaks due to the $m = 5$, 7, 9 and 11 modes are overestimated by the step-like photoelastic profile.

In Figure 2.11 the trapezoid-like/step-like Raman-Brillouin intensity ratios is shown as a function of layer thickness L_z. These ratios are calculated using the analytical expression

$$\frac{I_{trap}}{I_{step}} = \left[\frac{\sin(k_m z_-)}{k_m z_-}\right]^2 \tag{2.13}$$

which is a simple squared *sinc* function, where $k_m = m\pi/L_z$. The trapezoid-like profiles (characterized by z_-) are those discussed in the previous section, and plotted in Figure 2.7. These profiles were obtained for a fixed excitation energy ($E_i = 4.075$ eV) and homogeneous broadening ($\gamma = 25$ meV), and for layer thickness ranging from 2 nm to 25 nm (plotted range in Figure 2.11). It can be seen that the convergence between the trapezoid-like and step-like models is rather rapid for the first confined mode $m = 1$. The intensity ratio is around 0.4 for $L_z = 2$ nm and reaches 0.9 for $L_z = 17$ nm. For the $m = 3$ mode this ratio is only 0.33 at $L_z = 17$ nm and less than 0.05 for the $m = 5$ and 7

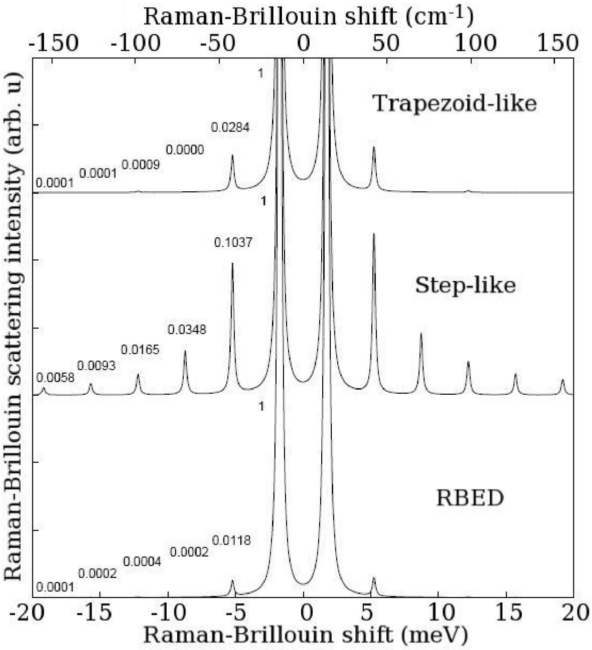

Figure 2.10: Inelastic light scattering spectra simulated according to the Raman-Brillouin quantum model ($\delta' = -7$ and $\gamma' = 1.2$) and using the photoelastic model with step-like and trapezoid-like profiles of the photoelastic coefficient. The layer thickness is 10 nm. Each spectrum has been normalized to the intensity of the first low-frequency peak (out of the vertical scale). The intensity ratios, with respect to the first peak, are indicated for the anti-Stokes scattering.

modes. The shorter the wavelength is (in comparison with z_-) the greater the sensitivity to the photoelastic profile is.

In most of the published works [30; 64], the photoelastic model, with the crude assumption of a step-like photoelastic coefficient, succeeded in simulating the acoustic vibrations induced Raman-Brillouin scattering and the modulation of the optical response observed in time-resolved pump-probe experiments. However, in some cases, for instance in short period superlattices (i.e. with layer thicknesses smaller that the acoustic wavelengths), or for excitation close to optical resonances [161], strong deviations between measured and calculated Raman-Brillouin intensities are noticed. In these situations the photoelastic profile can strongly deviate from a step-like profile as shown in Figures 2.4, 2.6 and 2.7. Therefore, we propose to improve the PEM (in the high vibration frequency range) by using trapezoid-like, instead of step-like, profiles for the photoelastic coefficient. The dependence of these profiles on the layer thickness is also relevant and has been discussed

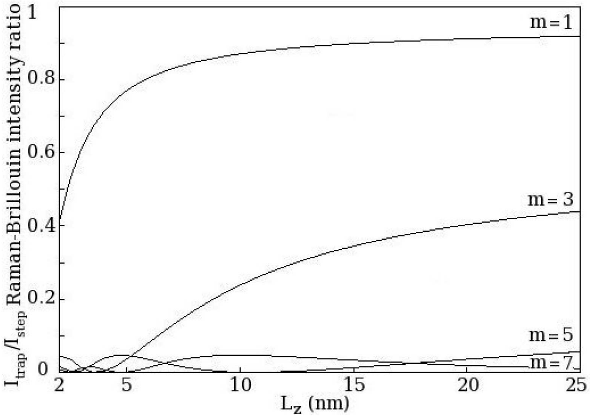

Figure 2.11: Raman-Brillouin intensity ratio I_{trap}/I_{step} as a function of the layer thickness L_z, calculated using the PEM with either the trapezoid-like or the step-like photoelastic profiles. The trapezoid-like profiles are those fitting the RBED for excitation energy $E_i = 4.075$ eV and homogeneous broadening $\gamma = 25$ meV. Results are shown for the $m = 1$, 3, 5, and 7 confined vibration modes.

in the previous section. Nevertheless, it is important to keep in mind that these profiles depend on the excitation energy.

Moreover, experimental data were reported in Reference [172] on silicon membranes with thicknesses ranging from 24 nm to 32 nm (cf. Figure 2.1). The light scattering was excited below the fundamental direct transition. It has been shown that the PEM with a step-like photoelastic constant, well accounts for the Raman-Brillouin intensities associated to the first confined acoustic vibrations. However, some deviations of the simulated spectra from the measured ones can be noticed for the high frequency confined vibrations (cf. Figure 2.1b). According to Figure 2.7 differences between the Raman-Brillouin intensities calculated with the trapezoid-like and step-like profiles are indeed expected for such thin layers. It is worthwhile to mention that due to the low scattering efficiency of very thin layers, experiments are usually performed close to resonance with some optical transitions involving confined electronic states. This enhances the Raman-Brillouin scattering but the latter can no longer be described in the framework of the PEM independently of the profile of the photoelastic constant used (trapezoid-like or step-like). As shown in Figure 2.4 the RBQM is more appropriate in the case of resonant excitation.

It is worthwhile to underline that the experimental Raman-Brillouin peak intensities strongly depend on the incident and scattered photon fields [172], i.e. on the scattering configuration (forward and backward scattering). In these calculations a simple standing electromagnetic waves (cosine functions) were considered. More complete modeling of the optical properties is required to compare directly with experiments.

The scattered intensities calculated with the RBQM differ from those obtained with the PEM for both the step-like and trapezoid-like profiles. Although, the latter is based on a good approximation of the RBED distribution inside the layer, it does not take into account explicitly outgoing resonance effects. Indeed, the RBED depends on the excitation energy, optical transitions (energy, homogeneous broadening) and also on the scattered photon energy, i.e. on the vibration mode energy (resonance factor for the outgoing photons in Equation 2.9). This was not taken into account while fitting the RBED with trapezoid-like profiles. In other words, the vibration energies were assumed to be smaller than the homogeneous broadening of the electronic transitions and thus identical resonance factors for the incident and scattered photons are considered. It can be noticed from Figure 2.10 that the explored vibration energy range (40 meV in both Stokes and anti-Stokes regions) is larger than the homogeneous broadening ($\gamma = 25$ meV) of the optical transitions. Thus, strictly speaking, for a given layer thickness and excitation energy, a particular trapezoid-like profile should be determined for each scattered photon energy (i.e. for each emitted or absorbed vibration mode) for the description to be fully correct. This points out the limitations of the PEM to describe acoustic vibrations, even if size-dependent trapezoid-like profiles are included.

The limitations of the PEM pointed out, as well as the improvements proposed in this chapter are of importance for the interpretation of Raman-Brillouin scattering measurements in more complex nanostructures. An application of the theoretical approach will be further discussed in the case of semiconductor superlattices in the following chapter.

Chapter 3

Raman-Brillouin Electronic Density in Superlattices

Contents

In the previous chapter, I have introduced a Raman-Brillouin electronic density (RBED) by combining the electronic transitions and electronic states of a system according to their relative contribution to the light scattering process [80; 128]. This approach allows to generate electronic density profiles that capture the physics of the electron-vibration interaction, and related Raman-Brillouin spectra, even though thousands of electronic transitions may be involved. Indeed, the RBED is useful when a large number of electronic transitions are excited by the optical probe. This is for instance the case of semiconductor quantum dots excited close to E_1 transitions characterized by flat valence and conduction band dispersions (i.e. large effective masses) [80]. In that situation, interferences between the numerous scattering paths take place, thus blurring the connexion between the Raman-Brillouin spectral features and the excited electronic states. Moreover, it has been shown that the RBED is the link between the widely used Photoelastic model of the Raman scattering and quantum models which account for optical resonance effects.

The present chapter is devoted to the implementation of the Raman-Brillouin electronic density for two-dimensional periodic nanostructures [188]. Indeed, short period GaAs/AlAs superlattices (SL) are considered here as a model system where the utility of the RBED can be tested [98]. Direct comparison between simulated and measured spectra will be presented. For each SL, the spatial distribution of the RBED will be studied for various excitation energies. It is shown how these RBED profiles, combined with the symmetry of the acoustic vibration modes, allow for a clear understanding of the resonant Raman-Brillouin scattering in complex nanostructures where periodicity, quantum confinement, layering of the vibrational properties and optical selection of electronic transitions are simultaneously present. Moreover, the RBED profiles are compared to the step-like profile of the Photoelastic coefficient. I show why the profile of this coefficient underestimates or overestimates the electron-vibration interaction thus leading to erroneous Raman-Brillouin scattering intensities of folded acoustic vibrations. The originality of the work presented in this chapter lies in the implementation of the RBED as a theoretical tool to understand and interpret the main tendencies observed experimentally in complex nanostructures. With use of this formalism it is possible to describe variations of acoustic vibration features, such as doublets in the spectrum that were not possible to explain previously and fell out of the scope of the standard photoelastic model [92].

3.1 GaAs/AlAs superlattices

In this section superlattice systems that consist of periodic GaAs/AlAs quantum wells will be considered (cf. Figure 3.1). Three GaAs/AlAs superlattices with nearly the same nominal folding frequency $(d_{GaAs}/v_{GaAs} + d_{AlAs}/v_{AlAs})^{-1} = 1.2$ THz and different GaAs (d_{GaAs}) and AlAs (d_{AlAs}) thicknesses are studied. v_{GaAs} and v_{AlAs} are the longitudinal sound velocities in GaAs and AlAs. In Table 3.1 the nominal parameters characterizing both materials, as well as the parameters deduced from X-Ray diffraction are shown. The measured thicknesses are very close to the nominal ones. It is well known that changing the well/barrier thickness ratio in SLs leads to strong variations of the associated Raman signature (cf. Section 3.2.1) [30]. Our samples correspond to three different values of the well/barrier thickness ratio ($\frac{d_{GaAs}}{d_{AlAs}} \approx 2.32$, 0.82 and 0.28) while the SLs period $d = d_{GaAs} + d_{AlAs}$ is almost the same (around 4.4 nm). The samples SL1, SL2, and SL3 were chosen to allow for a detailed investigation of their Raman-Brillouin scattering properties covering the three situations $\frac{d_{GaAs}}{d_{AlAs}} < 1$, $\frac{d_{GaAs}}{d_{AlAs}} = 1$ and $\frac{d_{GaAs}}{d_{AlAs}} > 1$.

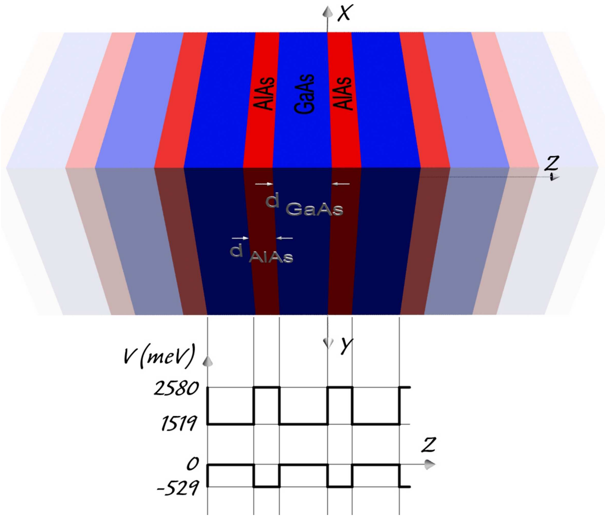

Figure 3.1: Sketch of GaAs/AlAs superlattice and potential profile of conduction and valence bands along the growth direction (z-direction).

Table 3.1: Parameters describing three periodic GaAs/AlAs superlattices, SL1, SL2, and SL3. Number of periods, nominal and measured thicknesses $d_{GaAs(AlAs)}$ of the GaAs (resp. AlAs) layer, and type of the three superlattices.

Sample	Number of periods	d_{GaAs} (nm) nominal	d_{GaAs} (nm) measured	d_{AlAs} (nm) nominal	d_{AlAs} (nm) measured	$\overline{x}_{AlAs}$ measured	Type
SL1	200	2.954	2.90	1.173	1.25	0.3	I
SL2	200	1.969	2.00	2.346	2.43	0.54	II
SL3	200	0.985	0.99	3.519	3.55	0.78	II

An optical evidence of the direct-to-indirect-gap transition in GaAs-A1As short-period superlattices has been evidenced has been pointed out by Danan *et al* [**?**]. The optical properties of the studied superlattice allow them to distinguish direct type-I SL on the one hand, or indirect type-II SL, on the other hand.

Raman-Brillouin measurements have been performed by Bernard Jusserand and co-workers at the Institut des NanoSciences de Paris [98]. The spectra have been recorded at room temperature, in near-backscattering (BS) configuration, using a Dilor XY800 triple spectrometer in the subtractive mode and a CCD detector. Six excitation wavelengths from an Argon ion laser and from a near infrared tunable Ti:Sa laser have been used. The Stokes Raman spectra, normalized either to the first (SL1) or to the second (SL2 and SL3) acoustic mode, are shown in Figure 3.2. In agreement with the design of the

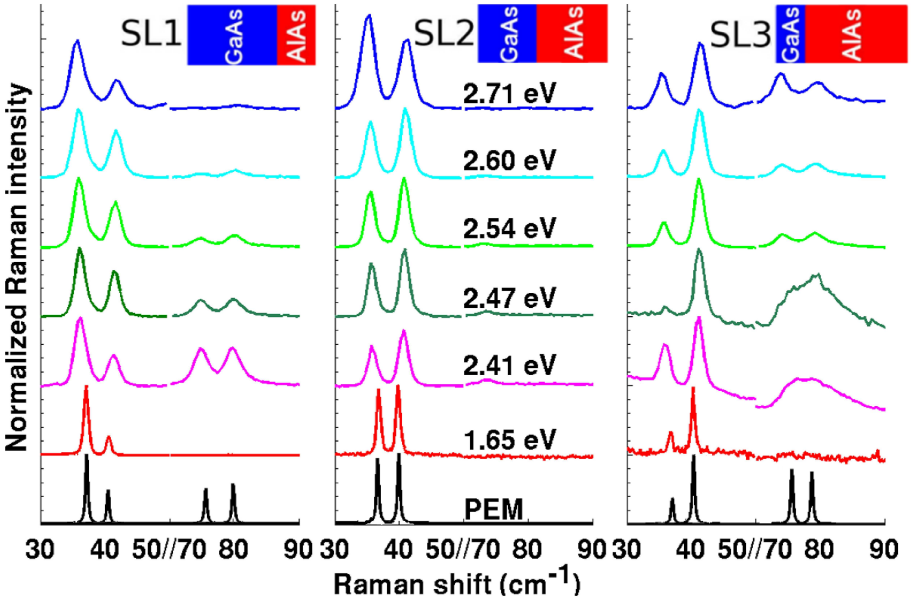

Figure 3.2: Color plots: Raman-Brillouin spectra recorded from the three superlattices SL1, SL2, and SL3. The excitation energies E_i are indicated in the central panel. The black spectra have been calculated using the PEM at E_i =1.65 eV. The drawings at the top of the panels help to visualize the GaAs(blue)/AlAs(red) thickness ratio. Raman-Brillouin measurements performed by B. Jusserand and co-workers at the Institut des NanoSciences de Paris.

samples (constant period), the average Raman shift of the acoustic vibration doublets is nearly the same for the three SLs and independent on the excitation energy, while the doublet splitting reflects the energy dependence of the vibration wavevector probed in BS and the slight variation of the average sound velocity from sample to sample. The relative intensity of the first and second doublets and of the two components of each doublet displays strong variations from sample to sample: changes of the intensity ratio between the spectral components of the first acoustic doublet and the scattering by the second acoustic doublet [21; 159; 160].

3.2 Raman-Brillouin electronic density formalism

The experimental results shown in Figure 3.2 can be interpreted using either the Photoelastic Model (PEM) or the Raman-Brillouin Quantum Model (RBQM), as described in detail in the previous chapter. In the RBQM, the SL electronic eigenstates are taken into account explicitly.

3.2.1 Photoelastic model

For scattering by longitudinal acoustic (LA) vibrations, the Raman-Brillouin intensity is given by Equation 2.11. For superlattices, the photoelastic coefficient $P(z)$ is now a step-like periodic function along the superlattice axis, given by $P(z) = 0.48$ in GaAs and $P(z) = 0.005$ in AlAs [37]. The displacement fields of LA vibrations are calculated as a linear combination of reflected and transmitted waves using the transfer matrix method as described in References [76] and [180]. The displacement field $u_m(z)$ is normalized over the whole superlattice. Dispersion relation of the LA vibrations in the case of infinite superlattice is given by [30]:

$$\cos(qd) = \cos\left[\omega_q\left(\frac{d_{GaAs}}{v_{GaAs}} + \frac{d_{AlAs}}{v_{AlAs}}\right)\right] - \frac{\epsilon^2}{2}\sin\left(\omega_q\frac{d_{GaAs}}{v_{GaAs}}\right)\sin\left(\omega_q\frac{d_{AlAs}}{v_{AlAs}}\right), \tag{3.1}$$

where q is the LA vibration wavevector and

$$\epsilon = \frac{\varrho_{GaAs}v_{GaAs} - \varrho_{AlAs}v_{AlAs}}{\sqrt{\varrho_{GaAs}v_{GaAs}\varrho_{AlAs}v_{AlAs}}} \tag{3.2}$$

is a parameter describing the contrast between the acoustic impedances $\varrho_{GaAs(AlAs)}$ of both materials. The LA vibration dispersion is shown in Figure 3.3 for the three studied superlattices (considered as infinite). Equation 3.1 allows for extracting the eigenfrequencies ω_q of the LA vibration modes.

For both PEM and RBQM, an incident (resp. scattered) electromagnetic field $A_{i(s)}(z)$ of the form $\exp(ik_{i(s)}z)$ is considered, where $k_{i(s)}$ is the incident (resp. scattered) photon wavevector component along the z-direction. The in-plane component $\vec{k}_{||}$ of the incident and scattered wavevectors are neglected.

In Figure 3.2, the Raman-Brillouin spectra calculated using the PEM (Equation 2.11) are shown as solid black lines at the bottom. The PEM spectra were generated with a transferred wavevector corresponding to the near infrared excitation (E_i=1.65 eV). The PEM intensities do not depend strongly on the excitation energy. In contrast, it is very clear from the measured spectra (Figure 3.2) that significant variations of the Raman-Brillouin intensities with excitation energy are observed experimentally. These variations cannot be described by the photoelastic model. The most evident discrepancy is the absence of the second doublet in the near infrared spectra of SL1 and SL3 (red line in Figure 3.2). Moreover, strong intensity variations of the second acoustic doublet

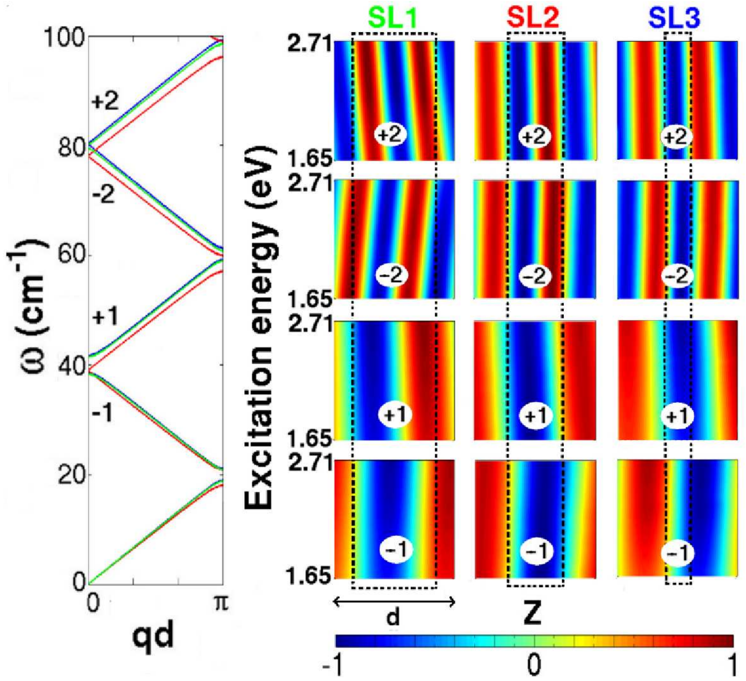

Figure 3.3: Left panel: Dispersion of LA vibrations for the superlattices, SL1 (green), SL2 (red) and SL3 (blue), calculated from Equation 3.1. The acoustic branches are identified as (±1) and (±2). Right panels: Deformation field div$[u_m(z)] = \frac{\partial u_m(z)}{\partial z}$ of the modes (±1) and (±2), calculated using the transfer matrix method for each finite superlattice and excitation energy. The deformations are shown within a unitary cell, centered on the GaAs layer. The black dashed lines indicate the GaAs/AlAs interfaces.

and of the intensity ratio within the first acoustic doublet are observed depending on the excitation energy.

3.2.2 Raman-Brillouin quantum model

Similarly to the PEM, the RBQM introduced in Chapter 2, and in particular Equation 2.1, can be adapted to the case of the superlattices. e, e' and h are now the electron and hole eigenstates of the GaAs/AlAs superlattices. The electron-photon interaction Hamiltonian is given by Equation 2.5, where $\vec{A}_{i(s)}$ is the potential vector of the incident (resp. scattered) light within the superlattice. The deformation-potential interaction between the electronic states and the LA vibrations is now given by $H_{e-vib} = D_{e(h)}(z)\text{div}\left[\vec{u}_m(z)\right]$, where $D_{e(h)}(z)$ is a step-like periodic function describing the electron (resp. hole) deformation potential [184; 189].

The sum in Equation 2.1 runs over all intermediate conduction states e and e' and initial valence states h. For the sake of simplicity, only zero in-plane wavevector electron-hole transitions will be considered. Each state is described by a Bloch wavefunction $\Psi_{e(h)}(\vec{r}) = \upsilon_{e(h)}(\vec{r})\phi_{e(h)}(z)$ where $\upsilon_{e(h)}(\vec{r})$ is the atomic-like wavefunction of the electrons (resp. holes) and $\phi_{e(h)}(z)$ the envelope wavefunction along the superlattice axis. The latter is calculated by solving Schrödinger equation numerically and assuming parabolic dispersion of the valence and conduction bands (cf. Figure 1.4). The validity of this Krönig-Penney model [87; 91] is discussed further. Calculations are performed for the real superlattices: the fact that the SL size is limited by the surface and substrate presence has been taken into account. However, the superlattices length was limited to 40 periods to keep within reasonable computation time. As a matter of fact, it is possible to check that the results do not differ significantly when changing the number of periods from 20 to 40. Figure 3.4 shows the calculated subbands for electrons (blue) and holes (red) in SL1. A zoom-in of the first electron subband helps to visualize the spatial localization as well as the symmetry of the first five electron states within the SL.

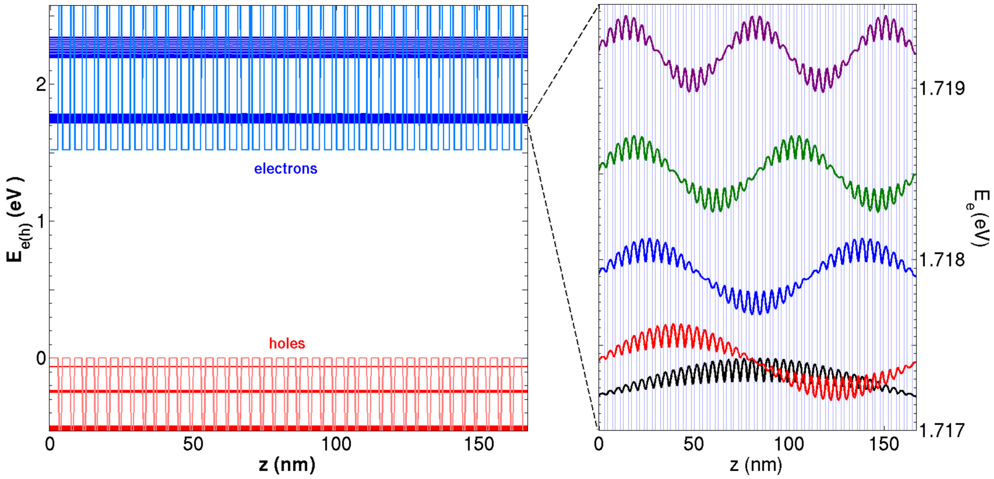

Figure 3.4: Left panel: Electronic subbands calculated using the parabolic band approximation in SL1. The electron (blue) and hole (red) subbands are shown in the potential profiles of the valence and conduction bands. Right panel: Zoom-in showing the first five electron states of the first subband.

Similarly to the case of the thin films, it is possible to introduce a Raman-Brillouin electronic density which combines the superlattice wavefunctions of the intermediate electronic states according to their incoming and outgoing resonance factors by rewriting the inelastic light scattering efficiency (Equation 2.1). However, contrary to Chapter 1, the RBED is here split into two different components: the electron RBED ρ^e_{RB} and the hole RBED ρ^h_{RB}. For a scattering process mediated by the conduction electrons, the normalized RBED is

$$\rho^e_{RB}(z) = \frac{1}{\mathcal{R}} \sum_{e,e',h} R^s_{h,e'} \phi^*_{e'}(z) R^i_{e,h} \phi_e(z), \tag{3.3}$$

where the resonance factors $R^i_{e,h}$ and $R^s_{h,e'}$ are given by:

$$R^i_{e,h} = \frac{\langle e| H^i_{e-pht} |h\rangle}{E_i - E_{e-h} + i\gamma_{e-h}} \tag{3.4a}$$

$$R^s_{h,e'} = \frac{\langle h| H^s_{e-pht} |e'\rangle}{E_s - E_{e'-h} + i\gamma_{e'-h}}. \tag{3.4b}$$

The scattering paths involving hole-vibration interactions give rise to:

$$\rho^h_{RB}(z) = \frac{1}{\mathcal{R}} \sum_{e,h,h'} R^s_{e,h'} \phi^*_{h'}(z) R^i_{h,e} \phi_h(z), \tag{3.5}$$

where $\mathcal{R}$ is given by Equation 2.9. The overall Raman-Brillouin scattering rate is now given by:

$$\mathcal{P}(\vec{k}_i, \vec{k}_s, \vec{k}_m) = \frac{2\pi}{\hbar} \left| \mathcal{R} \int \left[D_e(z)\rho^e_{RB}(z) + D_h(z)\rho^h_{RB}(z) \right] \frac{\partial u_m(z)}{\partial z} dz \right|^2 \delta(E_s \pm \hbar\omega_m - E_i). \tag{3.6}$$

From Equation 3.6, $\mathcal{R}\rho^{e(h)}_{RB}(z)$ appears as the electronic density distribution interacting with the vibration modes and giving rise to the Raman-Brillouin scattering. $\mathcal{R}\rho^{e(h)}_{RB}(z)$ are complex functions (Equation 3.4) because of the homogeneous broadening of the electron-hole transitions (Table 3.2) and because the photons potential vectors are complex.

Similarity between Equations 2.11 and 3.6 can be noticed. $\mathcal{R}D_{e(h)}(z)\rho^{e(h)}_{RB}(z)$ in Equation 3.6 plays the same role as $A^*_s(z)A_i(z)P(z)$ in Equation 2.11. Since $\mathcal{R}D_{e(h)}$ is constant and $A_{i(s)}$ is nearly constant within each layer ($d_{GaAs(AlAs)} \ll \lambda_{i(s)}$), $\rho^{e(h)}_{RB}(z)$ can be compared to $P(z)$. However, $\rho^{e(h)}_{RB}(z)$ includes the electromagnetic fields and the electronic structure of the system and is therefore well suited for the analysis of the resonant light scattering process. As discussed in the previous chapter, the RBED is the link between the Raman-Brillouin quantum model and the Photoelastic model.

Table 3.2: Damping parameters of the electron-hole transitions γ_{ij} and electron D_e and hole (averaged) D_h deformation potentials in GaAs and AlAs. The ij subindices refer to the electron and hole subbands. Deformation potentials are taken from References [184] and [189].

γ_{11}	γ_{22}	γ_{13}	GaAs		AlAs	
			D_e	D_h	D_e	D_h
10 meV	200 meV	500 meV	7.17 eV	2.72 eV	5.64 eV	2.61 eV

3.3 Results and discussion

3.3.1 Comparison between measured and simulated spectra

In this section I compare the measured RB spectra with those calculated using the Photoelastic model and the Raman-Brillouin quantum model. The aim of this chapter is to point out some limitations of the PEM and to show that the Raman-Brillouin quantum model gives a more accurate and complete description of the experimental spectra and of their changes with excitation energy (resonance effects). This is particularly important because it ensures that the RBED, which will be described and discussed in the next section, is indeed a description giving a good agreement with experiments.

Figures 3.5, 3.6 and 3.7 show the Raman-Brillouin spectra of the three superlattices calculated using the RBQM (Equation 3.6) and for excitation energy ranging from 1.65 eV to 2.75 eV. The calculated electron-heavy hole (e-hh) and electron-light hole (e-lh) transition energies are indicated in each figure. The optical indices used in these calculations were extracted from ellipsometry measurements and depend on the excitation energy. The electron-hole transition dampings γ_{ij} used in the simulations as well as the deformation potentials $D_{e(h)}$ are quoted in Table 3.2. The dampings selected are those giving the best agreement with the experimental results, and with the work by Kushibe *et al* [92].

Since the Raman-Brillouin peak frequencies of the (±1) and (±2) doublets are well reproduced by both the PEM and RBQM, the comments will be focused on the scattered intensities and on the comparison with the experiments.

For SL1 (Figure 3.5), the most remarkable point concerns the scattering by the second doublet (±2). Indeed, the spectrum calculated using the RBQM (Equation 3.6) shows no activation of the second doublet (±2) for red excitation (E_i =1.65 eV) and up to 2.2 eV. This is in a very good agreement with the spectrum measured with excitation at 1.65 eV (Figure 3.2). Scattering by the second doublet is indeed completely absent. On the contrary, the spectrum calculated using the PEM (lower spectrum in Figure 3.2) exhibits scattering by both first and second doublets with similar intensities for any excitation energy (not shown here). Indeed, only small variations of the scattered intensities are expected due to small changes of the exchanged wavevector (cf. Equation 2.11). Moreover, scattering by the second doublet is clearly activated for excitation at 2.41 eV in the experiments and then decreases with increasing energy (Figure 3.2). This behaviour is well reproduced by the calculated spectra in Figure 3.5. The intensity of the second doublet is maximum at 2.55 eV and then decreases with further increase of the excitation energy. The appearance of the second doublet coincides with the resonant excitation of the electron-heavy hole $e_2 - hh_2$ and electron-light hole $e_2 - lh_2$ transitions (indicated in Figure 3.5). For GaAs quantum wells of few monolayers, as those in the SLs investigated in this chapter, the parabolic band approximation (Figure 3.4) overestimates the electronic subband energies. Therefore the calculated electronic transitions may be larger than the actual ones. This results in an underestimation of the interference effects, thus leading to an overestimation of the Raman-Brillouin intensity of the second doublet. This could explain why the calculated intensity maximum of the second doublet occurs at higher excitation energy (2.55 eV) than experimentally observed (2.41 eV).

Concerning the scattering by the first doublet (±1) the experimental intensity ratio I_{+1}/I_{-1} increases from 0.25 at 1.65 eV to 0.7 at 2.54 eV and then decreases to 0.45 at 2.71 eV (Figure 3.2). This variation is also connected with the resonant excitation of $e_2 - hh_2$ transitions and is well reproduced by the simulations based on the RBQM (cf. Figure 3.5).

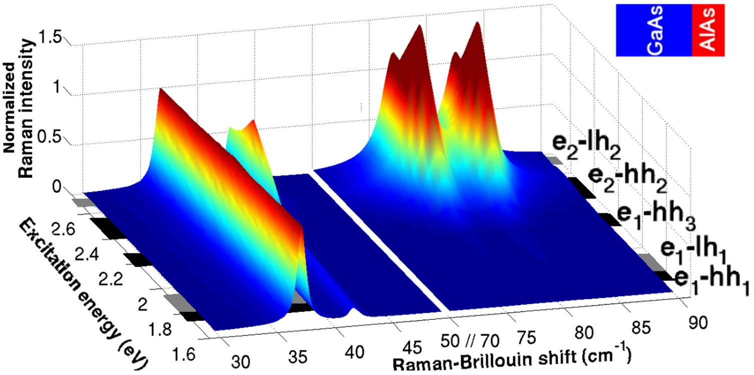

Figure 3.5: Raman-Brillouin spectra of SL1 calculated using the RBQM for different excitation energies E_i. For each excitation energy the scattered intensity is normalized to the first peak (−1). Calculated electron-hole transition energies involving the different subbands are marked to the right.

For SL2, the scattering by the second doublet (±2) is predicted to be very small (with respect to scattering by the first doublet (±1)) by both the RBQM (Figure 3.6) and the PEM (Figure 3.2) in agreement with the measurements (Figure 3.2). However, the RBQM shows that a small activation is expected for excitation energies close to the $e_2 - hh_2$ transitions (2.88 eV< $E_{e_2-hh_2}$ <2.97 eV). This is indeed observed experimentally for E_i ≈2.47 eV (Figure 3.2). As mentioned above, the parabolic bands approximation may explain the shift between the calculated and observed excitation energies for this activation.

The scattering by the first doublet shows an inversion of the I_{-1}/I_{+1} intensity ratio (Figure 3.2) that occurs when changing the excitation energy from 2.41 eV to 2.71 eV: I_{-1}/I_{+1} =0.72 at 2.41 eV and I_{-1}/I_{+1} =1.37 at 2.71 eV. This behaviour is reproduced by the RBQM even though the intensity ratio is reversed compared to the experimental one. This discrepancy can be explained by the fact that, for SL2, the GaAs and AlAs thicknesses are very similar and very small. Indeed, a difference of only one monolayer between the nominal and the actual average thicknesses can be responsible for the inversion of the I_{-1}/I_{+1} intensity ratio [85].

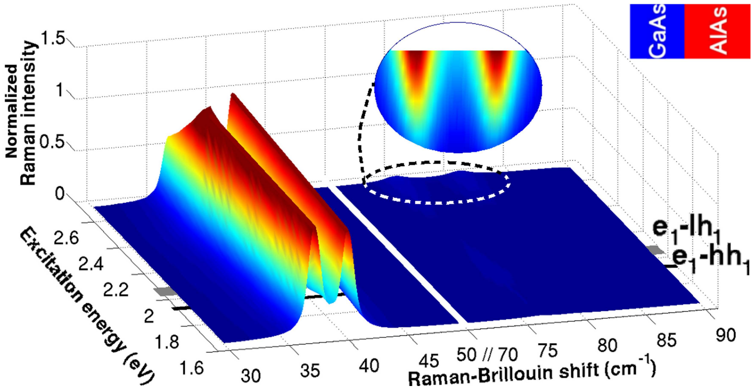

Figure 3.6: Raman-Brillouin spectra of SL2 calculated using the RBQM for different excitation energies E_i. For each excitation energy the scattered intensity is normalized to the first peak (+1). The inset is a zoom-in (color scale multiplied by 20) of the excitation energies for which the small activation of the second doublet (±2) is predicted. Calculated electron-hole transition energies involving the different subbands are marked to the right.

For SL3, the RBQM simulations are also in good agreement with the experimental data. First, the measured I_{-1}/I_{+1} intensity ratios are very close to the calculated ones (cf. Figures 3.2 and 3.7). Even the oscillatory-like variation of the I_{-1}/I_{+1} ratio with excitation energy is well reproduced by the simulations: the measured I_{-1}/I_{+1} oscillates between 0.2 (excitation at 2.45 eV) and 0.6 (excitation at 2.71 eV). This behaviour is well reproduced by the RBQM.

Scattering by the second doublet (±2) is predicted by the RBQM (Figure 3.7). The calculated intensity ratio $I_{\pm 2}/I_{+1}$ is around 0.2 compared to 0.6 experimentally. It reaches a maximum for excitation around E_i =2.45 eV, close to the resonances with the $e_1 - hh_1$ and $e_1 - lh_1$ transitions (cf. inset in Figure 3.7), in agreement with the experiments (Figure 3.2). The discrepancy between measured and calculated $I_{\pm 2}/I_{+1}$ intensity ratio, like for SL1, is mostly due to the overestimation of the electronic subbands energies which weaken the interference effects. Moreover, close to the maximum of the second doublet, a broadening of the (±2) Raman bands is predicted (cf. inset in Figure 3.7). This effect can explain the broad band observed experimentally (cf. Figure 3.2) for an excitation at E_i =2.47 eV. Since the QWs of SL3 are very narrow, the symmetries of the deformation fields associated to the acoustic modes are not as well defined as in SL1 and in SL2. Indeed, a slight shift of the nodes with respect to the center of the QW changes significantly the overlap between the deformation field and the RBED. This leads to a bad selection of the wavevector q, resulting in a broadening of the (±2) Raman bands. Such effect appears for the second doublet because the associated deformation fields are strongly varying, and therefore they are more sensitive than for the to the first doublet.

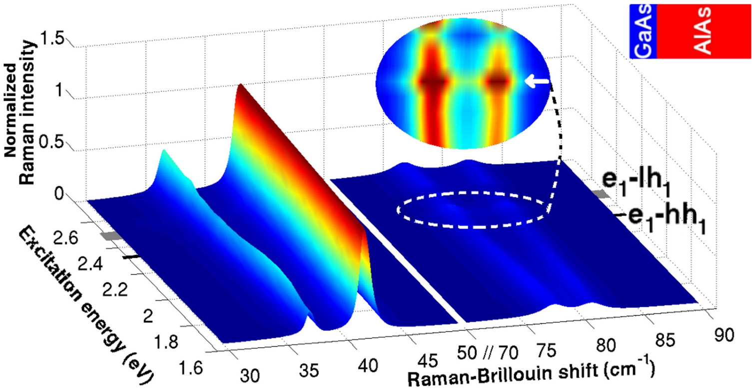

Figure 3.7: Raman-Brillouin spectra of SL3 calculated using the RBQM for different excitation energies E_i. For each excitation energy the intensity is normalized to the first peak (+1). The inset is a zoom-in (color scale multiplied by 20) of the excitation energies for which the broadening of the second doublet (±2) is predicted. Calculated electron-hole transition energies involving the different subbands are marked to the right.

3.3.2 Raman-Brillouin electronic density

In order to understand better the resonant Raman-Brillouin scattering, it is necessary to consider the symmetry of the acoustic vibration modes and their coupling to the optically excited electronic states.

According to the GaAs thicknesses, and to the number of periods in the SLs (used in the simulations), there are about 4500 electron-hole transitions that may significantly contribute to the light scattering process depending on the considered SL (symmetry forbidden transitions such as $e_1 - hh_2$, $e_1 - lh_2$, $e_2 - hh_1$ and $e_2 - lh_1$ can be excluded). Since finite superlattices are considered here, there is no translational invariance because of the presence of the surface and of the substrate [133]. Therefore, there is no wavevector conservation in the three interaction steps (Equation 2.1) of the light scattering process, and thus no (spatial) selection of electronic transitions. Wavevector conservation progressively and naturally comes out in the simulations when increasing the SLs length with respect to the optical wavelength (i.e. when translational invariance is recovered). Hence, due to the huge number of possible interfering scattering paths, it is very difficult to connect the electronic structure of the SLs to the changes of the Raman-Brillouin spectral features. The Raman-Brillouin electronic density introduced in Section 3.2.2, allows to overcome this difficulty by combining the thousands scattering paths into a single effective electronic density.

The RBED generated for electrons (Equation 3.3) and for holes (Equation 3.5) are very similar due to the fact that both are mostly confined within the GaAs quantum wells (type I SLs) [188]. Only small differences are found in their spatial extension around the QWs due to their different effective masses, thus we can focus on the RBED generated for the electrons only. Moreover, since the RB scattering amplitude is proportional to the RBED $\mathcal{R}\rho^e_{RB}(z)$ (cf. Equation 3.6), we will analyze the properties of this quantity rather than those of the normalized RBED $\rho^e_{RB}(z)$ (Equation 3.3).

Figures 3.8 to 3.10 show the Raman-Brillouin electronic density $\mathcal{R}\rho^e_{RB}(z)$ profiles along the z-axis of the three superlattices and for excitation energies ranging from 1.6 eV to 2.85 eV. The real $\mathrm{Re}\left\{\mathcal{R}\rho^e_{RB}(z)\right\}$ and the imaginary $\mathrm{Im}\left\{\mathcal{R}\rho^e_{RB}(z)\right\}$ parts of the RBED as well as its modulus $|\mathcal{R}\rho^e_{RB}(z)|$ are shown. The modulation along the superlattice axis z is due to the spatial variation of the electromagnetic fields and to the spatial distribution of the electronic states. The modulus of the RBED is mainly localized in the QWs and reflects the SLs periodicity. The RBED profiles (Figures 3.8 to 3.10) strongly depend on the excitation energy due to optical resonances with the electron-hole transitions involving the different SL subbands. Moreover, it can be noticed that for some excitation energies the RBED profiles (real and imaginary parts and modulus) exhibit minima. These minima occur around 1.7 eV and 1.9 eV in Figure 3.8 for instance. They arise from destructive interferences between scattering paths from the $e_1 - hh_1$, $e_1 - lh_1$ and $e_1 - hh_3$ transitions. Let us examine how the RBED captures the essential physics of the resonant Raman-Brillouin scattering for each superlattice.

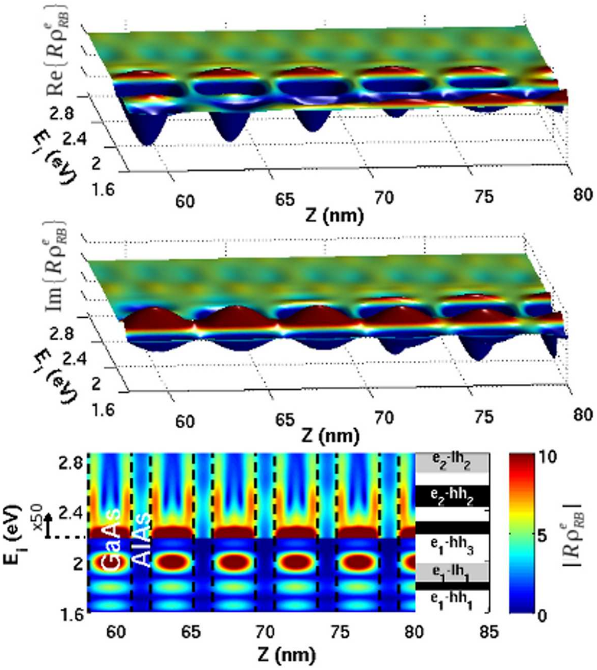

Figure 3.8: Raman-Brillouin electronic density (RBED) $\mathcal{R}\rho^e_{RB}(z)$ spatial distribution for SL1 for different excitation energies E_i. From top to bottom the real, imaginary parts and the amplitude of the RBED are shown within a few periods of the SL. The color scale of the real and imaginary parts is the same. In the lower panel (modulus of $\mathcal{R}\rho^e_{RB}(z)$), the color scale for energies above 2.2 eV should be divided by 50. The dashed lines show the barrier/well interfaces. The electron-hole transition energies are marked to the right of the lower panel.

For SL1, the RBED profiles (real and imaginary parts and modulus in Figure 3.8) exhibit maxima or minima (for the real and imaginary parts) centered on each quantum well for excitation energy 1.8 eV< E_i <2.2 eV, i.e. close to resonance with the $e_1 - hh_1$, $e_1 - lh_1$ and $e_1 - hh_3$ transitions (cf. Figure 3.5). Therefore, the coupling of the RBED to the acoustic mode (-1) is optimum since the associated deformation field is mainly symmetric with respect to the center of the QWs (cf. Figure 3.3 and Equation 3.6).

On the other hand, it can be noticed from Figure 3.3, that the deformation field of the (+1) mode is mainly antisymmetric leading to a weaker overlapping with the RBED. The corresponding Raman-Brillouin scattering is less intense than that of the (−1) mode (cf. simulated spectra in Figure 3.5), in agreement with the measured spectra (Figure 3.2).

For excitation close to resonance with the $e_2 - hh_2$ transitions (2.4 eV< E_i <2.6 eV), the RBED profiles (real and imaginary parts and modulus in Figure 3.8) are double peaked with maxima close to the edges of the GaAs QWs. This gives rise to a good overlapping with the deformations $\frac{\partial u_{\pm 2}(z)}{\partial z}$ associated with the second acoustic doublet (±2) since these deformations are symmetric with two nodes in the QW (cf. Figure 3.3). As a consequence, Raman-Brillouin scattering by the second acoustic doublet is activated (cf. Figures 3.2 and 3.5).

Moreover, scattering by the (±2) doublet does not come out (cf. Figures 3.2 and 3.5) for red excitation (E_i =1.65 eV) because, although mainly symmetric, the associated deformations has negative and positive values (cf. Figure 3.3) that cancel the overlapping with the single peaked symmetric RBED (cf. Figure 3.8).

It is worthwhile to mention that the RBED profiles reported in Figure 3.8 point out the reason why the PEM, with a step-like variation of the Photoelastic coefficient (Equation 2.11), fails to describe the Raman-Brillouin scattering in SL1 even for non-resonant excitation (red line in Figure 3.2). Indeed, scattering by the second acoustic doublet (±2) is overestimated by the PEM with respect to the experimental data. Due to its step-like shape, the PE coefficient strongly overlaps with the symmetric deformations of the (±2) doublet leading to overestimation of the corresponding Raman-Brillouin intensity.

For SL2, the RBED profiles are symmetric with respect to the center of each GaAs QW. As for SL1, the RBED modulus is maximum at the center of the GaAs QWs for excitation close to resonance with the $e_1 - hh_1$ and $e_1 - lh_1$ transitions, whereas for excitation close to resonance with $e_2 - hh_2$ transitions (2.88 eV< $E_{e_2 - hh_2}$ <2.97 eV), the maxima occur close to the edges of the QWs (cf. real and imaginary parts in Figure 3.9). The latter occurs at higher energy than in SL1 because of the smaller GaAs thickness. It is worthwhile to mention that, for energies around 2.8 eV, part of the RBED is delocalized within the AlAs barriers.

In SL2, the deformation fields of the (±2) vibration modes are mainly antisymmetric with respect to the center of the QWs (Figure 3.3). Therefore, their overlapping with the symmetric RBED is very small (in comparison with the case of SL1) and the corresponding Raman-Brillouin scattering is very weak (cf. Figures 3.2 and 3.6). As noticed in the previous section, a small activation of the (±2) doublet is observed experimentally (Figure 3.2) for excitation energy around 2.41 eV and is well reproduced by the simulations

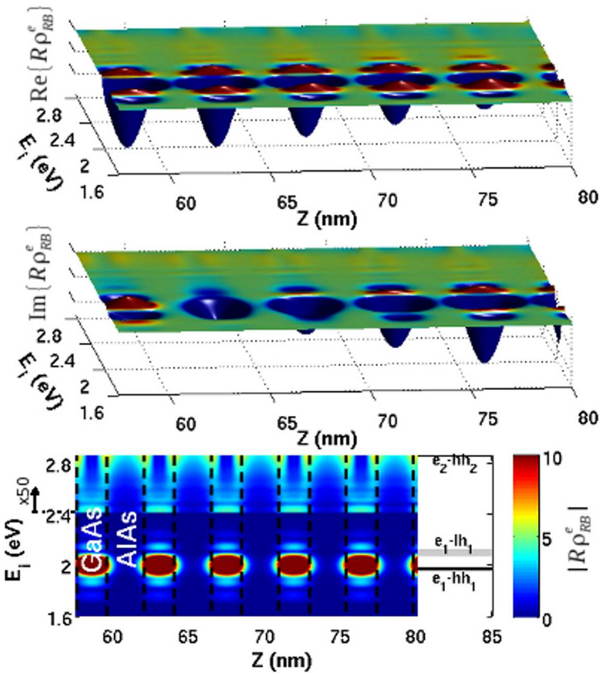

Figure 3.9: Raman-Brillouin electronic density (RBED) $\mathcal{R}\rho^e_{RB}(z)$ spatial distribution for SL2 for different excitation energies E_i. From top to bottom the real, imaginary parts and the amplitude of the RBED are shown within a few periods of the SL. The color scale of the real and imaginary parts is the same. In the lower panel (modulus of $\mathcal{R}\rho^e_{RB}(z)$), the color scale for energies above 2.4 eV should be divided by 50. The dashed lines show the barrier/well interfaces. The electron-hole transition energies are marked to the right of the lower panel.

around 2.6 eV (Figure 3.6).

Moreover, the change of the I_{-1}/I_{+1} intensity ratio with excitation energy, noticed in the previous section, arises from slight changes in the symmetry of the (± 1) vibration modes. Indeed, from Figure 3.3 it can be clearly seen that the nodes of the deformation fields are shifted with respect to the center of the GaAs QW so leading to different overlapping with the RBED and to the intensity inversion observed in Figure 3.2 when changing the excitation energy.

For SL3, since the QW thickness is only 0.99 nm, the e_2 nor hh_2 subbands are at high energies and therefore there are well above the quantum wells; the RBED is constructed with e_1, hh_1 and lh_1 subbands only. Therefore, the modulus of the RBED, as well as its real and imaginary parts, are symmetric and exhibit a single lobe with respect to the center of the GaAs QW independently of the excitation energy (Figure 3.10). From Figure 3.3 it can be noticed that the (-1) vibration mode is mainly antisymmetric with respect to the center of the GaAs QW whereas the $(+1)$ mode is mainly symmetric. Hence, the overlapping of the $(+1)$ mode with the RBED (Figure 3.10) is larger than that of the (-1), giving a stronger Raman-Brillouin intensity as observed experimentally (Figure 3.2) and in the simulations (Figure 3.7).

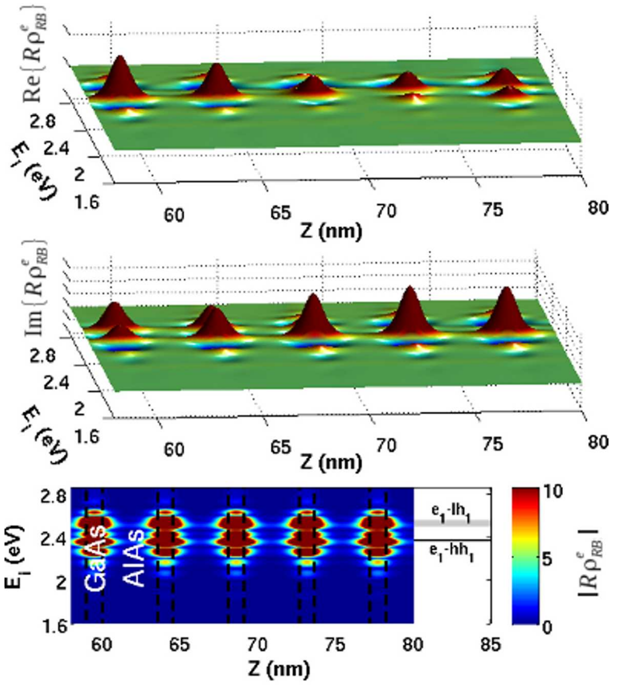

Figure 3.10: Raman-Brillouin electronic density (RBED) $\mathcal{R}\rho^e_{RB}(z)$ spatial distribution for SL3 for different excitation energies E_i. From top to bottom the real, imaginary parts and the amplitude of the RBED are shown within a few periods of the SL. The color scale of the real and imaginary parts is the same. The dashed lines show the barrier/well interfaces. The electron-hole transition energies are marked to the right of the lower panel.

The deformation fields associated with the (± 2) modes are mainly symmetric with a single maximum located around the center of the GaAs QW (cf. Figure 3.3). Their overlapping with the symmetric RBED gives rise to the activation of the Raman-Brillouin scattering observed in Figure 3.2. It is worthwhile to notice that, once again, the PEM overestimates the scattering by the second acoustic doublet with respect to the experimental data (spectra of SL1 and SL3 in Figure 3.2) and to the simulation performed with the RBQM (Figures 3.5 and 3.7; red excitation E_i =1.65 eV).

Finally, it is interesting to mention that, according to the spatial distribution of the RBED in the superlattices studied (Figures 3.8 to 3.10), we can conclude that the light scattering process originates mainly from the GaAs QWs. This is the reason why the empirical assumption $P_{AlAs} \ll P_{GaAs}$ has been often used in the PEM to describe the RB scattering in such nanostructures. These examples based on the three SLs described in this chapter stress the importance of the RBED as a very useful tool to interpret the physical origin of many spectral features in the Raman-Brillouin spectroscopy of such nanostructures.

Summary Part I

An effective electronic density has been introduced in the framework of the Raman-Brillouin quantum model. It allows to discuss, in a direct and a rather simple way, resonance effects and size dependence of the Raman-Brillouin spectra even when a large number of intermediate electronic states are involved in the light scattering. In particular, in the case of thin films, the importance of diagonal electron-vibration interaction matrix elements for nano-sized objects has been pointed out, as they are responsible for the main contribution to the Raman-Brillouin scattering. The Raman-Brillouin electronic density (RBED) also serves to investigate the validity of the step-like profile of the photoelastic coefficient usually assumed in the photoelastic model. It has been shown that for layer thickness smaller than 25 nm the trapezoid-like profile is more realistic than the step-like profile. The Raman-Brillouin spectra calculated using both profiles are comparable for the lowest frequency vibration mode ($m = 1$ confined mode) and for layer thickness larger than 17 nm. The profile of the photoelastic coefficient has strong impacts on the Raman-Brillouin intensities of the highest frequency confined modes (m =3, 5, 9, ...), particularly for very thin layers (below 10 nm). As a matter of fact, it has been pointed out that the intensities of the m =5, 9, 11, ... vibration modes are overestimated by a step-like profile. No convergence between the intensities calculated with the step-like and trapezoid-like profiles was observed for layer thickness up to 25 nm. Moreover, it has been shown in this part of the thesis that due to optical selection of confined electronic states, neither the step-like nor the trapezoid-like profiles are able to approximate the RBED for resonant excitation.

Furthermore, in the case of complex nanostructures such as quantum wells superlattices, it has been shown that the information given by the spatial distribution of the RBED along the superlattice axis, combined with the symmetry of the acoustic vibrations, allow for a full understanding of the activation (or the absence) of light scattering for resonant and non resonant excitation of the optical transitions. The electronic properties of the superlattices were described in the framework of the envelope wavefunction approximation, using parabolic dispersions of the valence and conduction bands. Despite this simple model, which becomes questionable for very short superlattice periods, the agreement between measured and simulated Raman-Brillouin spectra is very satisfactory and the observed resonances behaviour is well accounted for. Comparison and analogy between the profiles of the photoelastic coefficient and those obtained with used of the RBED have been presented and discussed. In particular, the impact of the step-like variation of the photoelastic coefficient on the electron-vibration interaction has been pointed out: because the photoelastic coefficient is constant within each quantum well the electron-vibrations interaction can be overestimated or underestimated depending on the considered excitation energy. This leads to important discrepancies between the spectra simulated using the PEM and the measured ones even for non resonant excitation, i.e. in a situation where the PEM is commonly assumed to work. Finally, it is worthwhile to note that the concept of RBED as a theoretical tool for the interpretation of the Raman-Brillouin scattering is general and can be extended to analyze the Raman-Brillouin scattering in a variety of low-dimensional semiconductor and metallic systems. It is very useful when several electronic transitions may be resonantly and simultaneously excited by the probe light. Moreover, since the RBED depends only on the electronic properties, it can be used for the analysis of the resonant Raman scattering by optical vibrations.

Part II - Acousto-Plasmonics of Metallic Nano-Objects

Noble metals sustain localized surface plasmons when downsized to the nanoscale. These collective oscillations produce optical resonances associated with intense and localized electromagnetic fields. They can be spectrally and spatially fine tuned by controlling the size, the shape, and the structure of the nano-objects as well as by the interaction between nano-objects [65; 115; 145; 166]. These exceptional properties are pushing the synthesis of new plasmonic nano-objects (e.g. nanospheres, nanorods [83; 145], nanodisks [95], nanorice [187], nanorings [136], nanopyramids, nanostars [70]) and the fabrication of new electronic and optical devices [13; 132; 141] for applications in various scientific fields: nano-antennas [96; 164], negative refraction lenses, metamaterials, surface wave guides for the control of the light emission [41; 63; 196], chips for bio- and chemical sensing [42; 101], nano-objects for medical applications (imaging, diagnostic, therapy, and assisted surgery) [93; 111; 139]. In particular, closely-spaced nanoshells, nanorods, or nanoparticles arrays are suitable templates for Surface Enhanced Raman Scattering (SERS) [19; 104; 105; 181; 195] as well as for Surface-Enhanced Infrared Absorption (SEIRA) spectroscopy [4; 104; 178], where large electromagnetic field enhancements at selective spatial locations can be tuned by controlling the small interparticle distances. Tunable plasmonic nanostructures consisting of periodic arrays of interacting disks, rings and concentric ring-disk particles are also promising candidates for efficient chemical and bio-sensing [8; 97; 107; 178; 181]. One important challenge in the field of plasmonics is the ability to synthesize and fabricate metallic nano-objects and nanostructures with targeted optical properties on demand [97]. The influence of morphology on the optical properties of small metallic nanoparticles has been studied both theoretically and experimentally by several groups [44; 66; 70; 99; 100; 108; 117; 125; 140; 145]. Due to small defects, or to shape and size changes, strong variations in the optical properties of metallic nano-objects are expected and can be experimentally observed [86; 178; 181; 183].

Since part of my work has been devoted on the dynamical properties surface plasmons, Chapter 4 will introduce some basic aspects of acoustic vibrations and surface plasmons in metallic nano-objects. Plasmonic properties of metallic nano-objects will then be studied for concentric ring-disk nanosensors [97] and photoconductively loaded optical nanoswitches [96] in Chapter 5. I will show how the understanding of the optical properties of some of the commonly used nanoparticles, such as nanorings, nanodisks, and nanorods is still quite challenging and needs to be investigated further. Chapter 6 is devoted to the acousto-plasmonic dynamics in metallic nano-objects [99; 100; 181]. A study of the interaction process between low frequency acoustic vibrations and localized surface plasmons sustained by the metallic nano-ojects will be developed to conveniently describe Raman-Brillouin spectroscopy of metallic nano-objects.

Chapter 4

Acousto-Plasmonics: Basics

Contents

4.1 Acoustic vibrations

Acoustic vibrations in small metallic nanoparticles have been extensively investigated both theoretically and experimentally [15; 17; 40; 130; 134; 162; 163]. More specifically, some of these works focused on the Raman-Brillouin scattering by acoustic vibrations confined in metallic nano-objects [15; 17; 51].

4.1.1 Lamb's model

The free oscillations of a homogeneous, isotropic, and elastic sphere have been early studied mathematically by Horace Lamb in 1881 [94] (Figure 4.1) using elasticity theory [112] (cf. Chapter 1).

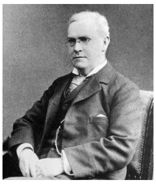

Figure 4.1: Sir Horace Lamb (1849-1934)

This approach is based on solving Navier-Stokes' equation (Equation 1.1) for the particular geometry. The general solution to this equation (Equation 1.3), in spherical coordinates, is given by

$$\begin{aligned}\vec{u}_{l,m}(\vec{r},t) &= A_l\,\overrightarrow{\text{grad}}\,[j_l(Q_L r)Y_{lm}(\theta,\phi)] \\ &+ B_l\,\overrightarrow{\text{rot}}\,[j_l(Q_T r)Y_{lm}(\theta,\phi)\vec{r}] \\ &+ C_l\,\overrightarrow{\text{rot}}\left\{\overrightarrow{\text{rot}}\,[j_l(Q_T r)Y_{lm}(\theta,\phi)\vec{r}]\right\}, \qquad (4.1)\end{aligned}$$

where $Q_{L(T)} = \omega_{vib}/v_{L(T)}$ are wavevectors related to the longitudinal (L) and transverse (T) sound velocities, j_l are the spherical Bessel's functions of order l, and Y_{lm} are the spherical harmonics, l being an integer ($-l \leq m \leq l$). Each vibration eigenfrequency is five-fold degenerated ($2l+1$).

Equation 4.1 involves two types of vibration modes: (i) torsional modes associated with the B_l coefficient, and (ii) spheroidal modes described by the A_l and C_l coefficients. In the following, I will focus only on the spheroidal modes which are the Raman active modes [15; 51].

In spherical coordinates, the force at the surface of the nanoparticle is given by [17]:

$$\vec{F} = \left[\lambda\ \text{div}\ \vec{u}_{l,m} + \mu\frac{\vec{u}_{l,m}\cdot\vec{e_r}}{r}\right]\vec{e_r} + \mu\ \overrightarrow{\text{grad}}\,(\vec{u}_{l,m}\cdot\vec{e_r}) + \mu\frac{\partial\vec{u}_{l,m}}{\partial r} - \mu\frac{\vec{u}_{l,m}}{r}, \qquad (4.2)$$

where $\vec{e_r}$ is the unitary radial vector. λ and μ are known as Lamé coefficients [112]. The coefficients A_l and C_l in Equation 4.1 are determined by the boundary conditions of the nanoparticle surface. For a free standing nanoparticle of radius R, the external force at the surface is null $\vec{F}(R\cdot\vec{e_r}) = \vec{0}$. The effect of the presence of a surrounding medium on the vibration modes has already been investigated [130].

Figure 4.2 shows the amplitude of the displacement due to the fundamental acoustic vibration modes ($n = 1$, $l = 0,\ 1,\ 2$), where n is the number of nodal spheres (i.e. where the motion is null), and l is the number of nodal lines at the surface. A breathing mode ($l = 0$) corresponds to a radial displacement of the nanoparticle surface (Figure 4.2a). This acoustic vibration mode preserves the spherical symmetry of the nanoparticle. Dipolar ($l = 1$) and quadrupolar ($l = 2$) modes exhibit nodes at the surface, leading to the breaking of the spherical symmetry of the nanoparticle. Indeed, while parts of the surface are displacing outward, other parts are displacing inward (Figures 4.2b and 4.2c). The amplitude of the displacement is given by the normalization factor $\sqrt{\hbar/(2\rho V \omega_m)}$.

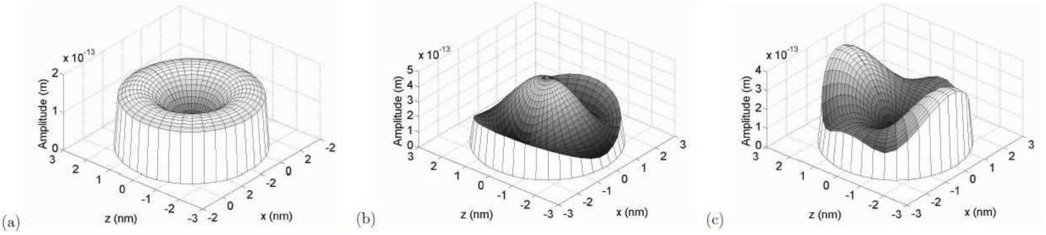

Figure 4.2: Amplitudes of the displacement in a cross section of a spherical nanoparticle of the first three fundamental eigenmodes ($n = 1$): (a) breathing mode ($l = 0$), (b) dipolar mode ($l = 1$) (c) quadrupolar mode ($l = 2$). Figure taken from Reference [15].

Using Lamb's model, one obtains that the eigenfrequencies of the vibration modes are inversely proportional to the nanoparticle diameter D. For an homogeneous and continuous sphere, the frequencies can be written as $\nu = Sv/D$ where S is a mode dependent coefficient, and v is the transverse sound velocity (or longitudinal for the spheroidal $l = 0$ modes). Typical relationships for the eigenfrequencies of the $l = 0$ and $l = 2$ fundamental spheroidal modes of a free nanoparticle are [162]:

$$\nu_{n=1}^{l=0} = 0.9\frac{v_L}{D} \tag{4.3a}$$

$$\nu_{n=1}^{l=2} = 0.84\frac{v_T}{D}. \tag{4.3b}$$

In addition to Lamb theory, atomistic approaches can also be used to describe the physics of the acoustic vibrations. Both theoretical approaches have been investigated and compared recently in the work by Nicolas Combe and Lucien Saviot in small metallic nanoparticles [40]. In this work, the importance of the anisotropy of the stiffness tensor in elastic calculations has been pointed out. A good agreement between the two approaches has been found for breathing and quadrupolar modes of silver nanoparticles larger than 2 nm. However, the applicability of the linear elasticity depends on the considered vibration mode and the nanoparticle size, and does not strongly depend on the actual shape of the nanoparticle. Moreover, critical sizes depend on the material.

4.1.2 Experimental techniques

Two main experimental techniques are commonly used to access the acoustic vibrations in metallic nanostructures. The first technique is based on ultrafast spectroscopy (pump-probe experiment), designed to measure time resolved optical transmission spectra and their modulation by acoustic vibrations (cf. left panel in Figure 4.3a) [74; 75]. Typical spectra are shown in the right panel of Figure 4.3a [28; 29]. They are obtained by taking the Fourier transform of the temporal signal since this technique gives access to the transitory regime of the system.

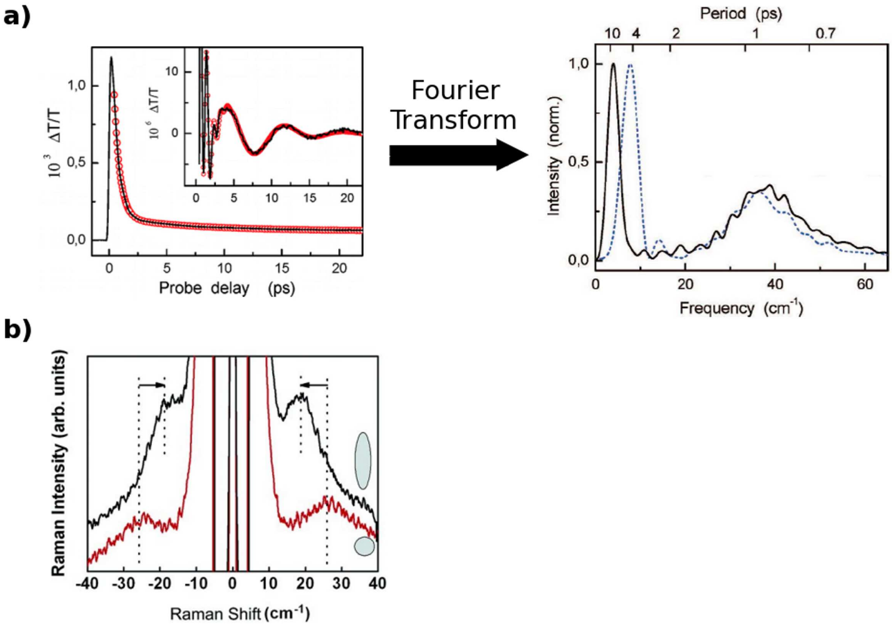

Figure 4.3: (a) Left panel: Time dependence of the transmission change $\Delta T/T$ measured in self-assembled silver nanocolumns. The oscillating component of the signal is shown in the inset. Right panel: Fast Fourier transform of the oscillating component of $\Delta T/T$ obtained for two silver nanocolumn samples. Figures taken from Reference [29]. (b) Raman spectra recorded for spherical silver nanoparticles (red line) and self-assembled silver nanocolumns (black line). Both Stokes and anti-Stokes components are shown in the spectra. Figure taken from Reference [116].

The second technique that gives access to the vibrational properties of nano-objects, is the Raman-Brillouin spectroscopy (cf. Chapter 1) [17]. An example of low frequency Raman-Brillouin spectra of silver spherical nanoparticles and nanocolumns is given in Figure 4.3b [116].

Time resolved femtosecond spectroscopy and Raman-Brillouin spectroscopy are complementary techniques since they give access to different vibration modes due to different selection rules, i.e. different electron-vibration coupling mechanisms (to be discussed in Chapter 6).

4.2 Surface plasmons

Noble metals have shown interesting optical properties since the beginning of the history giving for example particular colors in paintings like in Notre Dame Cathedral in Paris and in the Lycurgus Cup. The Lycurgus Cup (Figure 4.4) is one of the first historical evidence of the use of gold and silver nanoparticles for the coloring of stain glasses. This cup changes its color depending on the illumination. When it reflects light the cup appears green (Figure 4.4a), while in transmission it shows a reddish color (Figure 4.4b). Nowadays, it is well known that the coloration of the Lycurgus Cup is due to the excitation of surface plasmons (SP) of the metallic nanoparticles embedded into the glass. Their energies and associated electromagnetic field can be obtained from Maxwell's equations [24; 119; 125; 126; 166]:

$$\vec{\nabla} \cdot \vec{D} = 0 \tag{4.4a}$$

$$\vec{\nabla} \cdot \vec{B} = 0 \tag{4.4b}$$

$$\vec{\nabla} \times \vec{E} = -\frac{\partial \vec{B}}{\partial t} \tag{4.4c}$$

$$\vec{\nabla} \times \vec{H} = \frac{\partial \vec{D}}{\partial t}. \tag{4.4d}$$

Surface plasmons, exist at the interface between two materials where the real part of the dielectric function ε changes sign across the interface (e.g. a metal-dielectric interface) [3; 115; 138; 166]. The existence of surface plasmons was first predicted in 1957 by Rufus H. Ritchie [156] and then experimentally observed in 1960 by Cedric J. Powell [149; 150] using electron-energy loss spectroscopy (EELS).

Since their prediction, a large variety of studies have been devoted to the understanding of the fundamental aspects of surface plasmons [69] such as substrate effects on the

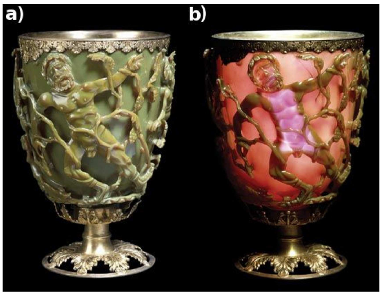

Figure 4.4: Roman Lycurgus Cup (British Museum, 4^{th} century A.D.): (a) illuminated from outside (reflection) appears in greenish color and (b) illuminated from inside (transmission) appears in redish color.

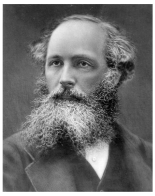

Figure 4.5: James Clerk Maxwell (1831-1879) published his equations in 1873 in "*A Treatise on Electricity and Magnetism*" [119].

plasmonic properties [89; 106; 185], Fano resonances [63; 72; 73; 103; 113; 171], lifetime [82; 167], higher order modes [86], retardation effects [61; 62], hybridization [137; 151; 190], and non local effects [6; 78]. I will briefly describe the optical properties of noble metals and remind here the basic physics of surface plasmons.

4.2.1 Optical properties of noble metals

The optical properties of metals are determined by (i) the free motion of the conduction electrons within the bulk materials, and (ii) electronic interband transitions. The collective response of the free-electron gas to the optical excitation gives rise to a macroscopic polarization:

$$\vec{P}(\omega) = \varepsilon_0 \chi_e(\omega) \vec{E}(\omega), \tag{4.5}$$

where $\chi_e = \varepsilon(\omega) - 1$ and ε are the electric frequency-dependent susceptibility and dielectric function of the medium

Experimental real and imaginary parts of the dielectric function of gold and silver, taken from Johnson and Christy [84], are shown in Figures 4.6 and 4.7, respectively (black stared lines).

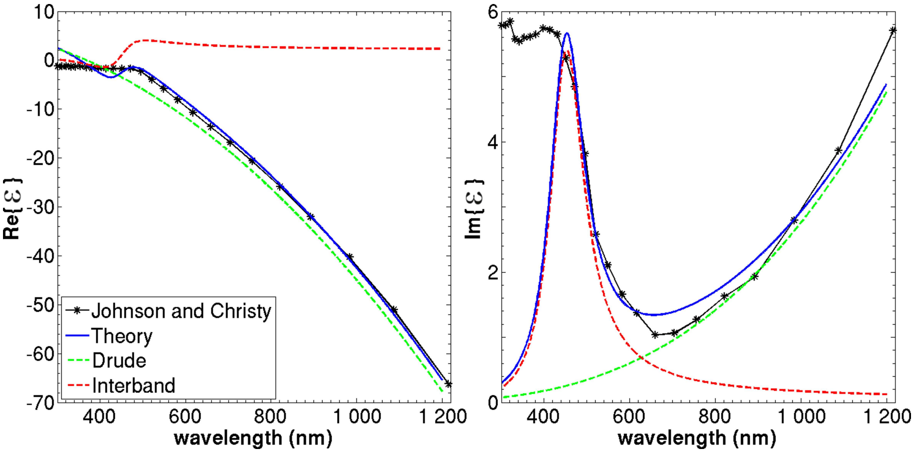

Figure 4.6: Experimental dielectric function of gold taken from Johnson and Christy [84] (black stared line) compared to the Drude dielectric function (green dashed line) and to the interband contribution (red dashed line). The dielectric function resulting of the summation of the Drude and interband contributions is also shown (blue line). Left panel: Real part of the dielectric function (Re$\{\varepsilon\}$). Right panel: Imaginary part of the dielectric function (Im$\{\varepsilon\}$). The physical parameters used for the Drude and interband contributions are quoted in Table 4.1.

4.2.1.1 Drude-Sommerfeld theory

The frequency-dependent dielectric function can be described by the Drude-Sommerfeld model [87; 115]. According to Drude-Sommerfeld model for the free-electron gas (electron of the conduction band), the equation of motion can be written as:

$$m_e \frac{\partial^2 \vec{r}}{\partial t^2} + m_e \gamma \frac{\partial \vec{r}}{\partial t} = e\vec{E}_0 e^{-i\omega t}, \tag{4.6}$$

where e and m_e are the charge and the effective mass of the free-electron, and ω and $\vec{E}_0$ are the frequency and the amplitude of the external electric field. $\gamma = v_F/l$ is a damping term depending on the Fermi velocity v_F and on the electron scattering mean free-path

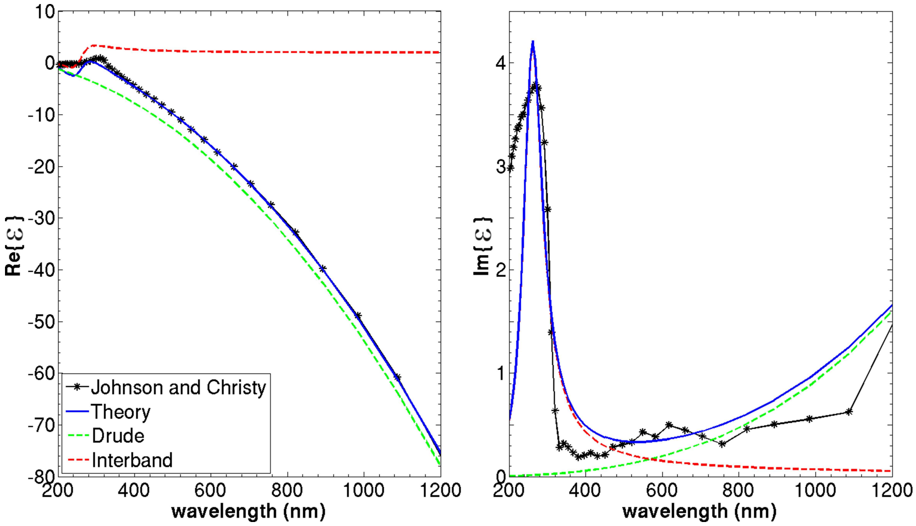

Figure 4.7: Experimental dielectric function of silver taken from Johnson and Christy [84] (black stared line) compared to the Drude dielectric function (green dashed line) and to the interband contribution (red dashed line). The dielectric function resulting of the summation of the Drude and interband contributions is also shown (blue line). Left panel: Real part of the dielectric function (Re{ε}). Right panel: Imaginary part of the dielectric function (Im{ε}). The physical parameters used for the Drude and interband contributions are quoted in Table 4.1.

l. The solutions of Equation 4.6 lead to:

$$\varepsilon_{Drude}(\omega) = 1 - \frac{\omega_p^2}{\omega^2 + i\gamma\omega}, \tag{4.7}$$

where $\omega_p = \sqrt{\frac{n_e e^2}{m_e \varepsilon_0}}$ is the bulk plasma frequency, n_e being the electronic density. Table 4.1 gives the bulk plasma frequencies and damping of gold and silver [84; 140]. Real and imaginary parts of the Drude dielectric function are shown in Figures 4.6 and 4.7 for gold and silver, respectively (green dashed line).

4.2.1.2 Interband transitions

Drude-Sommerfeld theory gives an accurate description of the optical properties of metals in the infrared spectral range (cf. Figures 4.6 and 4.7), or for some metals like aluminium where the contribution of interband transitions is negligible. For gold and silver, it is

Table 4.1: Fermi velocity v_F, electronic density n_e, plasma energy $\hbar\omega_p$, damping γ, and g_s coefficient (Fermi velocity to particle radius ratio) for gold and silver [84; 140]. Parameters for the interband contributions $\tilde{\omega}_p$, $\tilde{\gamma}_p$, and ω_0 are also given for both materials.

Metal	v_F (cm.s^{-1})	n_e (cm^{-3})	$\hbar\omega_p$ (eV)	$\hbar\gamma$ (meV)	$\hbar\tilde{\omega}_p$ (eV)	$\hbar\tilde{\gamma}$ (meV)	$\hbar\omega_0$ (eV)	g_s (eV.nm)
Au	1.40×10^{8}	5.90×10^{22}	8.9488	69.09	2.96	0.59	2.76	0.915
Ag	1.39×10^{8}	5.86×10^{22}	9.17	21	5.27	1.14	4.47	0.918

necessary to take into account the contribution of the electronic interband transitions in order to fully describe the optical properties of these metals in the visible range [115; 138].

In a first approximation, the contribution of the response of the bound electrons to the dielectric function of the metal can be described by means of simple a Lorentz oscillator of frequency ω_0, adding an harmonic force $\vec{F}_{Lorentz} = -m_e\omega_0^2\vec{r}$ to Equation 4.6. The resulting equation of motion, can then be solved with proper parameters $\tilde{\omega}_p$, $\tilde{\gamma}_p$, and ω_0 (quoted in Table 4.1). In this description, the interband dielectric function ε_{Inter} is given by:

$$\varepsilon_{Inter}(\omega) = 1 + \frac{\tilde{\omega}_p^2}{(\omega_0^2 - \omega^2) - i\tilde{\gamma}\omega}, \tag{4.8}$$

where $\tilde{\omega}_p = \sqrt{\frac{\tilde{n}_e e^2}{m_e\varepsilon_0}}$, $\tilde{n}_e$ being the density of the bound electrons (Drude-Lorentz theory). Real and imaginary parts of the interband contribution to the dielectric function are shown in Figures 4.6 and 4.7 for gold and silver, respectively (red dashed line). From the interband contributions, a clear resonant behaviour from the imaginary part can be observed (right panels in Figures 4.6 and 4.7) while a dispersive behaviour is observed from the real part (left panels in Figures 4.6 and 4.7). From wavelengths below ≈600 nm for gold (resp. ≈500 nm for silver), interband contributions obviously become significant while a Drude-Sommerfeld tendency is observed for wavelengths ≈600 nm for gold (resp. ≈500 nm for silver). The dielectric function of noble metals can finally be expressed as:

$$\begin{aligned} \varepsilon(\omega) &= 1 + \chi_{Intra}(\omega) + \chi_{Inter}(\omega) && (4.9a)\\ \Leftrightarrow \varepsilon(\omega) &= 1 - \frac{\omega_p^2}{\omega^2 + i\gamma\omega} + \frac{\tilde{\omega}_p^2}{(\omega_0^2 - \omega^2) - i\tilde{\gamma}\omega}, && (4.9b)\end{aligned}$$

where $\chi_{Intra(Inter)}(\omega) = \varepsilon_{Intra(Inter)}(\omega) - 1$ is the intraband (resp. interband) contribution to the electric susceptibility. Although the Lorentz oscillator model is widely cited in the litterature [24; 115; 138], it does not allow to correctly describe the interband

Table 4.2: Fitting parameters for the interband contribution (Equation 4.11) to the Johnson and Christy dielectric function of gold [84] taken from References [55; 56].

C_1/ω_1	ϕ_1 (rad)	$2\pi c/\omega_1$ (nm)	$2\pi c/\gamma_1$ (nm)	C_2/ω_2	ϕ_2 (rad)	$2\pi c/\omega_2$ (nm)	$2\pi c/\gamma_2$ (nm)
1.27	$-\pi/4$	470	1900	1.1	$-\pi/4$	325	1060

contributions in gold and silver unless a sufficiently large number of Lorentz oscillators are artificially added.

Following Pablo G. Etchegoin *et al* [55; 56], the contribution of the interband transitions to the dielectric function are obtained substracting the Drude contribution (Equation 4.7) to the experimental values [84]. The so extracted interband contribution can then be compared to the analytical models for these transitions. In the case of gold, an analytical expression of the dielectric function has been proposed [55; 56]:

$$\varepsilon(\omega) = \varepsilon_{bulk} + \varepsilon_{Drude} + G_1(\omega) + G_2(\omega) \tag{4.10}$$

with

$$G_i(\omega) = C_i \left[e^{i\phi_i} \left(\omega_i - \omega - i\gamma_i\right)^{\nu_i} + e^{-i\phi_i} \left(\omega_i + \omega + i\gamma_i\right)^{\nu_i} \right] \tag{4.11}$$

the contributions of the interband transitions. C_i, ϕ_i, ω_i, γ_i, and ν_i are the amplitude, the phase, the frequency associated to the gap, the damping, and the order of the pole, respectively. These parameters are adjusted in order to account for the interband contribution to the dielectric function. The G_i functions give a more accurate approximation of the interband transitions than a Lorentz oscillators model (Equation 4.8) [115; 138]. The results obtained using Equation 4.10 are shown in Figure 4.8 for gold (red lines) and compared to experimental values (black stared lines). The fitting parameters extracted from References [55; 56] for gold are quoted in Table 4.2.

Furthermore, the limitation of the electron mean free-path inside the nanoparticle implies interactions of the electrons with the particle surface that result in a size-dependent term in the damping parameter [45; 68; 115; 146]:

$$\gamma(\omega, R) = \gamma_0 + g_s(\omega)\frac{v_F}{R}, \tag{4.12}$$

where the parameter g_s is close to 1 eV.nm and is weakly dependent on ω [45; 68]. The

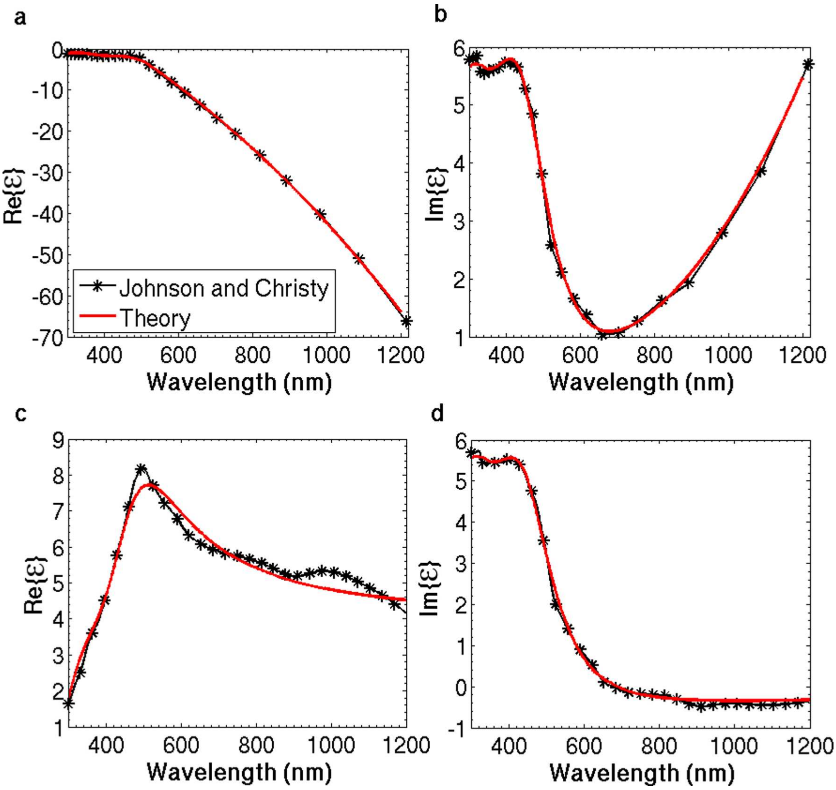

Figure 4.8: Upper panels: (a) Real Re$\{\varepsilon\}$, and (b) imaginary Im$\{\varepsilon\}$ parts of the analytical dielectric function ε of gold (red line) compared to Johnson and Christy data [84] (black stared line). Lower panels: (c) Real Re$\{\varepsilon\}$, and (d) imaginary Im$\{\varepsilon\}$ parts of the analytical interband contribution (red line) compared to the Johnson and Christy data (black stared line).

size-dependent dielectric function used in the simulations is then given by:

$$\varepsilon(\omega) = \varepsilon_{bulk} - \varepsilon_{Drude} - \frac{\omega_p^2}{\omega^2 + i\gamma(\omega, R)\omega}. \tag{4.13}$$

The values of the g_s coefficient and of the Fermi velocity v_F for gold and silver are quoted in Table 4.1.

4.2.2 Localized surface plasmons

In bulk materials, the collective motion of the electrons can be described by Equation 4.6. Under an external electromagnetic excitation (e.g. electric field, electrons), the electrons are collectively displaced with respect to the positive charges of the metal (cf. Figure 4.9a). The electron-electron Coulomb interaction is responsible for this collective and coherent motion of the electrons. A restoring force is exerted, due to Coulomb interaction, by the positive charges on the electron gas. The result of these two effects leads to a collective harmonic oscillation of frequency ω_p of the electrons, named bulk plasmon.

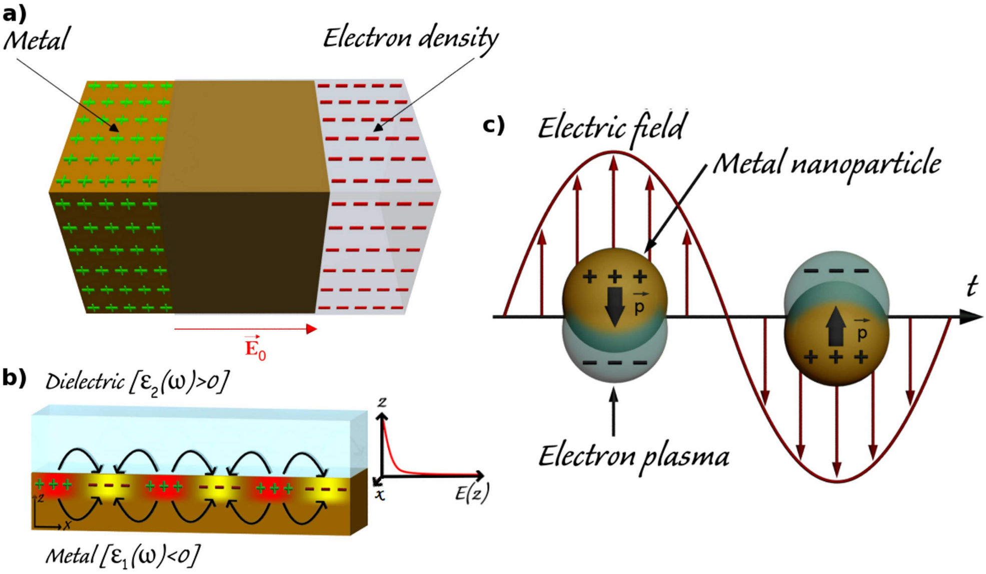

Figure 4.9: (a) Schematics of bulk plasmons: the electron density in metal oscillates under an external electric field $\vec{E}_0$. (b) Schematics of SPP at a metal/dielectric interface, propagating along the x-direction and confined in the z-direction. (c) Schematics of localized surface plasmons: the charge distribution of a metallic nanoparticle oscillates under an external electric field, inducing a dipole moment $\vec{p}$.

When a 2D metal/dielectric interface is introduced, Maxwell's equations can be solved with proper boundary conditions. The solutions obtained support surface electromagnetic waves propagating along the metal/dielectric interface, known as surface plasmon polaritons (cf. Figure 4.9b) [115; 138; 166]. Due to the dispersion of such electromagnetic modes, it is impossible to excite with light SPP on planar surfaces. Indeed, the momentum conservation cannot be fulfilled simultaneously for light and for SPP. However, there are several ways to bring additional momentum to couple light with SPP. One of the possibilities consists of coupling light with the plasmon excitations in a metallic particle where the finite size provides additional momentum to ensure the momentum conservation.

The optical response of a spherical metallic nanoparticle can be described in the same way (cf. Section 4.2.1). Localized non-propagating collective excitations of the free-electron gas, known as localized surface plasmons (LSPs), are obtained (cf. Figure 4.9c) [115; 138; 166]. For a spherical nanoparticle of radius $R \ll \lambda$, the spatial evolution of the electromagnetic field can be neglected, i.e. no retardation effect occurs (electrostatic limit)The electromagnetic solutions to this problem can be found, in the frequency domain, by solving Laplace's equation $\vec{\nabla}^2\Phi_j = 0$. The electric field is then given by $\vec{E}_j = -\vec{\nabla}\Phi_j$, where Φ_j is the scalar potential and j refers to the medium inside ($j = 1$) and to the medium outside ($j = 2$) the sphere.

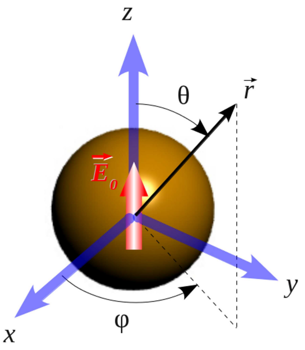

Figure 4.10: Framework adopted in this section. The incident electric field $\vec{E}_0$ is indicated by the red arrow.

The potentials satisfying simultaneously Laplace's equation and the proper boundary conditions are

$$\Phi_1 = -E_0\frac{3\varepsilon_2(\omega)}{\varepsilon_1(\omega)+2\varepsilon_2(\omega)}r\cos\theta \tag{4.14a}$$

$$\Phi_2 = -E_0 r\cos\theta + E_0R^3\frac{\varepsilon_1(\omega)-\varepsilon_2(\omega)}{\varepsilon_1(\omega)+2\varepsilon_2(\omega)}\frac{\cos\theta}{r^2}, \tag{4.14b}$$

where $\vec{E}_0$ is an external field, and $\varepsilon_{1(2)}$ is the dielectric function of the metal (1) and of the surrounding medium (2), respectively. The corresponding expressions for the electric field, deduced from $\vec{E}_j = -\vec{\nabla}\Phi_j$, are

$$\vec{E}_1(r) = E_0 \frac{3\varepsilon_2(\omega)}{\varepsilon_1(\omega) + 2\varepsilon_2(\omega)} \left(\cos\theta \vec{e_r} - \sin\theta \vec{e_\theta}\right) \tag{4.15a}$$

$$\vec{E}_2(r) = E_0 \left(\cos\theta \vec{e_r} - \sin\theta \vec{e_\theta}\right) + E_0 \frac{\varepsilon_1(\omega) - \varepsilon_2(\omega)}{\varepsilon_1(\omega) + 2\varepsilon_2(\omega)} \frac{R^3}{r^3} \left(2\cos\theta \vec{e_r} + \sin\theta \vec{e_\theta}\right) \tag{4.15b}$$

The electric field outside the sphere $\vec{E}_2$ is a superposition of the incident field and the field induced by an elementary electric dipole located at the center of the sphere. The induced dipole moment (cf. Figure 4.9c) is given by:

$$\vec{p} = \alpha(\omega)\vec{E}_0, \tag{4.16}$$

where α is the frequency-dependent polarizability given by:

$$\alpha(\omega) = 4\pi\varepsilon_0 R^3 \frac{\varepsilon_1(\omega) - \varepsilon_2(\omega)}{\varepsilon_1(\omega) + 2\varepsilon_2(\omega)}. \tag{4.17}$$

The spherical nanoparticle exhibits a localized surface plasmon resonance (LSPR) for the Fröhlich condition $\varepsilon_1 = -2\varepsilon_2$ which corresponds to the dipolar surface plasmon of the nanoparticle. For a spherical nanoparticle consisting of a metal described by a Drude-like dielectric function (Equation 4.7) in vacuum, Equation 4.17 leads to:

$$\alpha(\omega) = 4\pi\varepsilon_0 R^3 \frac{\varepsilon_1(\omega) - 1}{\varepsilon_1(\omega) + 2}. \tag{4.18}$$

The Fröhlich condition is then satisfied for $\omega_{l=1} = \omega_p/\sqrt{3}$.

When going beyond the electrostatic approximation, the electric field induced by an oscillating electric dipole of frequency ω with dipolar moment $\vec{p}$ is given by [24; 115; 138]:

$$\vec{E}(r) = \frac{1}{4\pi\varepsilon_0}\left[k^2\left(\vec{n}\times\vec{p}\right)\times\vec{n}\frac{e^{ikr}}{r} + \left(3\vec{n}\left(\vec{n}\cdot\vec{p}\right) - \vec{p}\right)\left(\frac{1}{r^3} - \frac{ik}{r^2}\right)e^{ikr}\right]e^{i\omega t}, \tag{4.19}$$

where $\vec{n} = \frac{\vec{r}}{r}$. Using Equation 4.19 it is now possible to distinguish two regions for the electric field: (i) the near-field region ($r \ll \lambda$), and (ii) the far-field region ($r \gg \lambda$). For an incident plane wave, the electric field can be described by Equation 4.20a in the near-field region and by Equation 4.20b in the far-field region.

$$\vec{E}(r) = \frac{1}{4\pi\varepsilon_0}\frac{3\vec{n}(\vec{n}\cdot\vec{p})-\vec{p}}{r^3}e^{-i\omega t} \tag{4.20a}$$

$$\vec{E}(r) = \frac{k^2}{4\pi\varepsilon_0}\frac{(\vec{n}\times\vec{p})\times\vec{n}}{r}e^{i(kr-\omega t)}. \tag{4.20b}$$

The scattering C_{sca} and absorption C_{abs} cross-sections can be obtained from the polarizability (obtained using Poynting's theorem) [24; 126]:

$$C_{sca}(\omega) = \frac{k^4}{6\pi\varepsilon_0}|\alpha(\omega)|^2 = \frac{8\pi}{3}k^4R^6\left|\frac{\varepsilon_1(\omega)-\varepsilon_2(\omega)}{\varepsilon_1(\omega)+2\varepsilon_2(\omega)}\right|^2 \tag{4.21a}$$

$$C_{abs}(\omega) = \frac{k}{\varepsilon_0}\ \mathrm{Im}[\alpha(\omega)] = 4\pi kR^3\ \mathrm{Im}\left[\frac{\varepsilon_1(\omega)-\varepsilon_2(\omega)}{\varepsilon_1(\omega)+2\varepsilon_2(\omega)}\right], \tag{4.21b}$$

where k is the wavevector in the surrounding medium. The extinction cross section is then simply given by: $C_{ext} = C_{abs} + C_{sca}$. It is interesting to notice that C_{sca} scales with R^6/λ^4 whereas C_{abs} scales with R^3/λ. Consequently, the extinction cross section for large particles is dominated by scattering, whereas for small particles it is dominated by absorption. Moreover, scattering becomes stronger at shorter wavelengths.

Electrostatic limit is a first approximation and other methods are needed to analyze larger objects ($R \not\ll \lambda$). The exact electromagnetic solutions to this problem can be obtained using Mie theory [24; 122]. Mie theory takes into account retardation effects due to the spatial variation of the electromagnetic field within the object. Surface plasmons are then obtained. The $R = 0$ limit of Mie theory gives the quasi-static limit: $\omega_l = \sqrt{\frac{l}{2l+1}}\omega_p$. Nevertheless, when the geometry of the object strongly differs from the spherical shape, the use of numerical methods is required to solve this electromagnetic problem. In the following chapters, the numerical calculations have been performed using the Boundary Element Method (BEM), presented in Appendix B.

For gold and silver nanoparticles, the Localized Surface Plasmon Resonances fall into the visible range of the electromagnetic spectrum. Several interesting properties of the LSPs make them valuable materials in nanophotonics [115; 145]: (i) localization of the electromagnetic fields close to the particle surface on subwavelength dimensions (beyond the diffraction limit) [63], (ii) field enhancement induced by charge piling at the surface of the particle [4], (iii) tunability of the LSPRs by changing the geometry of the particle, the environment and the interaction with other nanostructures [103].

Chapter 5

Localized Surface Plasmons in Nano-Optics

Contents

In this chapter, two examples of plasmonic applications will be discussed: concentric ring-disk nanosensors [97] for chemical and biological sensing [101] or field-enhanced spectroscopies [178; 181], and photoconductively loaded optical nanoswitchers [96] as highly integrated optical devices [96; 164]. I will show how the understanding of the optical properties of some of the commonly used nanoparticles, such as nanorings, nanodisks, and nanorods is still quite challenging and need to be investigated further.

5.1 Nano-antennas: optical switchers

5.1.1 Principle of the photoconductive optical switch

The functionality of plasmonic nano-antennas as novel building blocks for ultracompact nonlinear photonic devices. I propose that the small footprint, large light-matter interaction strength, and fast dynamics of single plasmonic nano-antennas can be used to design a new type of optical switches for controlling both the far-field and near-field distribution of light [144]. Tunability of the antenna by impedance loading of its nanogap using a dielectric medium has recently been described theoretically [10] and experimentally [23]. An early work by Auston *et al* described a “novel approach” to generate and detect of THz waves which are characterized by their high sensitivity and phase coherence [14]. Although the signal levels generated in these pionneer experiments are relatively low they opened the road to new optical devices using intense optical pulses. In this section I explore a related but conceptually very distinct approach using photoconductive loading of the antenna gap. As many concepts in nanoplasmonics, photoconductive switching draws on analogies in the radiowave regime [142]. The principle is based on the transition from capacitive to conductive coupling between two plasmon modes when bringing two nanoparticles into physical contact [12; 157]. Recently near-field investigations have shown control over progressive loading of a nano-antenna, which could be understood within the framework of circuit theory [164]. We show here that free-carriers photoexcited by an external laser source can be used to short circuit the antenna arms, leading to a strong modification of both the spectral resonance structure and near-field mode-profile. As the plasmonic antenna switch is based on a strong confinement of optical fields in space rather than in time, the antenna switch can operate at very low switching energy while potentially reaching a much faster response than microphotonic switching devices [9; 176].

The response of cylindrical gold nano-antennas is calculated using the boundary element method. The nano-antennas consist of two closely spaced cylindrical rods with their long axes aligned parallel as shown schematically in Figure 5.1. The rods have hemispherical endcaps. For the antenna switches the interparticle gap is loaded with amorphous silicon (a-Si). Amorphous silicon is chosen for its large electronic bandgap of 1.6 eV, high free-carrier nonlinearity, and further for its wide application range and compatibility with many technological processes (e.g. C-MOS process) [81]. The nonlinear optical response of crystalline silicon has been shown to be dominated by free-carrier absorption, with a much weaker contribution from gap filling and band structure renormalization [54; 170].

As similar arguments hold for a-Si, the dielectric function $\tilde{\varepsilon}(\omega)$ of photoexcited a-Si has been calculated by combining experimental dielectric function $\tilde{\varepsilon}_{\text{exp}}$ taken from Aspnes *et al.* [11] with the free-carrier Drude response [170], resulting in

$$\tilde{\varepsilon}(\omega) = \tilde{\varepsilon}_{\text{exp}}(\omega) - \left(\frac{\omega_{\text{pl}}}{\omega}\right)^2 \frac{1}{1 + i\frac{1}{\omega\tau_D}}, \tag{5.1}$$

where $\omega_{\text{pl}} = \sqrt{N_{eh}e^2/\varepsilon_0 m^*_{\text{opt}} m_e}$ denotes the plasma frequency of the photoexcited carriers, with N_{eh} the free-carrier density, $m^*_{\text{opt}} = (m_e^{*-1} + m_h^{*-1})^{-1}$ the optical effective mass of the carriers, and $\tau_D \sim 10^{-14}$ s the Drude relaxation time. The optical effective mass for a-Si, $m^*_{\text{opt}} = 0.17$, is close to the value for crystalline silicon [170]. The dielectric function $\tilde{\varepsilon}(\omega)$ was calculated from Equation 5.1 for values of the free-electron density N_{eh} ranging from 0 to 10^{22} cm^{-3}. Results are shown in Figure 5.2b, where the real and imaginary part of the complex index $\tilde{n} = \sqrt{\tilde{\varepsilon}} = n + i\kappa$ are plotted. For values of N_{eh} above 10^{21} cm^{-3}, a strong modification of the refractive index occurs corresponding to the formation of a free-carrier plasma. A critical density N_{eh}^{crit} can be defined as the transition from a primarily capacitive (dielectric) to primarily conductive (metallic) loading of the antenna gap, given by the condition $\text{Im}(\sqrt{\tilde{\varepsilon}}) > \text{Re}(\sqrt{\tilde{\varepsilon}})$. This condition yields an expression for the critical density:

$$N_{eh}^{\text{crit}}(\omega) = \frac{\text{Re}[\tilde{\varepsilon}_{exp}(\omega)]\varepsilon_0\, m^*_{opt}}{e^2}\left(\omega^2 + \frac{1}{\tau_D^2}\right). \tag{5.2}$$

The critical threshold depends quadratically on the optical frequency ω, while the influence of τ_D becomes prominent for $\tau_D < 1/\omega \sim 10^{-15}$ s, where it results in an overall shift of N_{eh}^{crit} to higher carrier densities.

The principle of operation of the nano-antenna switch is illustrated in Figure 5.1. In the unswitched case (cf. Figure 5.1a), the antenna supports half wavelength resonances over its individual arms [27; 59]. For gap sizes below S =50 nm, these half-wave modes are hybridized into a symmetric combination by the capacitive interaction between the two rods [151]. Figure 5.1b shows the response of the same antenna above the free-carrier switching threshold. As the antenna arms are conductively coupled, the antenna now supports a half-wave resonance over the full antenna length. As it will be shown below, the conductive gap loading results in strong modifications of both the far-field antenna response and the near-field mode-profiles.

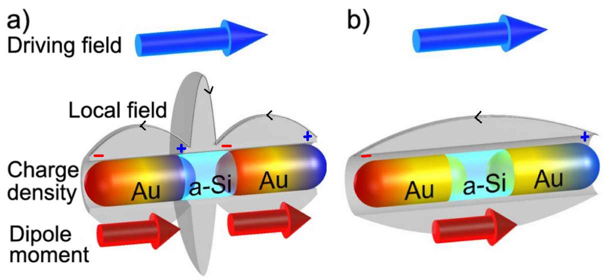

Figure 5.1: Illustration of the principle of antenna switching using a photoconductive gap, showing the fundamental mode of an unswitched (a) and a switched (b) nano-antenna.

5.1.2 Photoconductive far-field switching

Figure 5.2 presents the effect of photoconductive switching on the far-field resonances of a nano-antenna with a gap width S of 50 nm. The effect of a stationary carrier density are presented here, and dynamic effects will be discussed further below. For this antenna, the capacitive interaction between the two nanorods is relatively weak and the resonances resemble those of the individual nanorods. Far-field extinction spectra were calculated for free-carrier densities N_{eh} below (0 cm^{-3}, solid blue) and far above (10^{22} cm^{-3}, dashed red) the switching threshold. The unswitched antenna shows a strong resonance at a wavelength $\lambda_1 = 980$ nm, which can be attributed to the fundamental dipole modes of the uncoupled antenna arms [4]. Photoconductive switching induces a shift of the resonance position from λ_1 to λ'_1 over 350 nm, or a relative shift $(\lambda'_1 - \lambda_1)/\lambda_1$ of 36%. This switching effect is many times larger than that typically observed using dielectric loading [23; 191]. Importantly, the sharp resonance profile of a dipole antenna results in a large switching contrast of the extinction $\sigma_{\text{on}}/\sigma_{\text{off}}$ of 44 at the new resonance wavelength $\lambda'_1 = 1.33$ μm and inverse contrast $\sigma_{\text{off}}/\sigma_{\text{on}}$ of 11 at $\lambda_1 = 980$ nm. Calculated far-field radiation patterns corresponding to the two resonances of the unswitched and switched antenna are shown in the inset of Figure 5.2a. As both resonances correspond to a dipolar mode, no change is observed in the angular distribution pattern apart from an overall increase in radiative efficiency. As the radiated power is roughly proportional to the particle volume squared, this increase can be attributed to the addition of the photoconductive segment to the total antenna size.

Figure 5.3 explores into more details the antenna far-field response with progressive conductive loading for antennas with varying gap dimensions. The optical extinction of nano-antennas has been calculated with gap sizes S ranging from 0 nm to 50 nm. The dashed white lines in Figures 5.3a to 5.3f indicate the strongly wavelength dependent

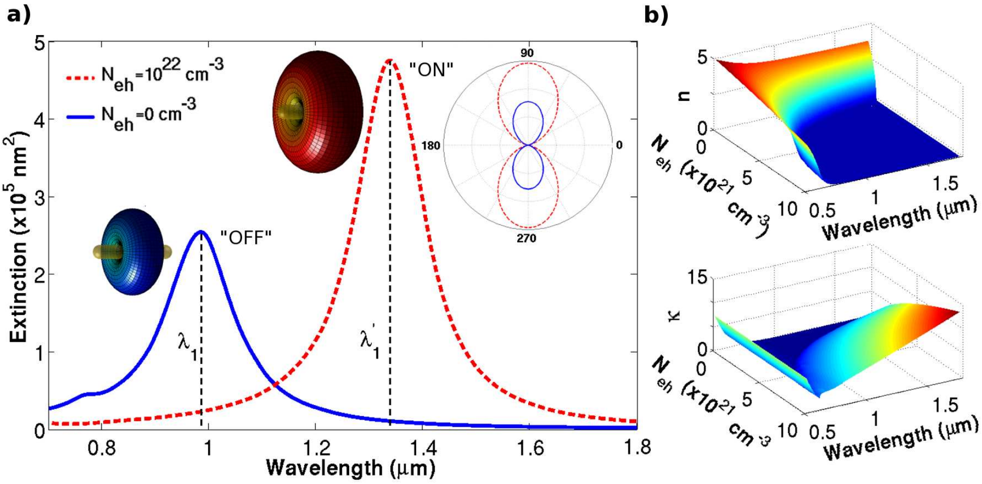

Figure 5.2: (a) Extinction spectra for an $S = 50$ nm antenna, under unswitched (blue) and switched (red, dash) conditions, corresponding to respective carrier densities of $N_{eh} = 0$ cm^{-3} and 10^{22} cm^{-3}. The 3D radiation patterns are associated to the λ_1 and λ_1' resonances of each switching mode. The inset represents the 2D cross section of these radiation patterns. (b) Real n and imaginary κ parts of the refractive index $\tilde{n} = n + i\kappa$, calculated using Equation 5.1 as a function of the wavelength and the photoexcited free-carrier density N_{eh}.

switching threshold for N_{eh}^{crit} introduced in Equation 5.2. The results shown in Figure 5.3f correspond to the antenna of Figure 5.2. The general behavior of the resonance structure with increasing free-carrier density can be understood using basic circuit theory [10; 164]. The blue-shift of the antenna resonance below the switching threshold can be understood using a simple resistor model. One can think of this coupled-antenna resonance as a pure capacitive cavity where the positive and negative polarization charges act as a capacitor. As the carrier density increases in the bottleneck of the cavity, there is a reduction of the charges (reduction of the Coulomb interaction), and there will be a blue-shift which is proportional to the reduction of the area of the capacitive coupling. There is a point where the current flow is so large, that this capacitive mode at the cavity cannot be sustained any more, thus it gets completely damped and dies out.

The emergence of a new resonance at longer wavelengths above the critical switching threshold corresponds to the transition of a capacitively coupled to a conductively coupled cavity, where the strong dispersion results from the peculiar charge density pattern which piles up positive and negative charges at the end of the antenna (cf. Figure 5.6). Starting from the purely conductive mode at 10^{22} cm^{-3}, as the carrier density decreases and

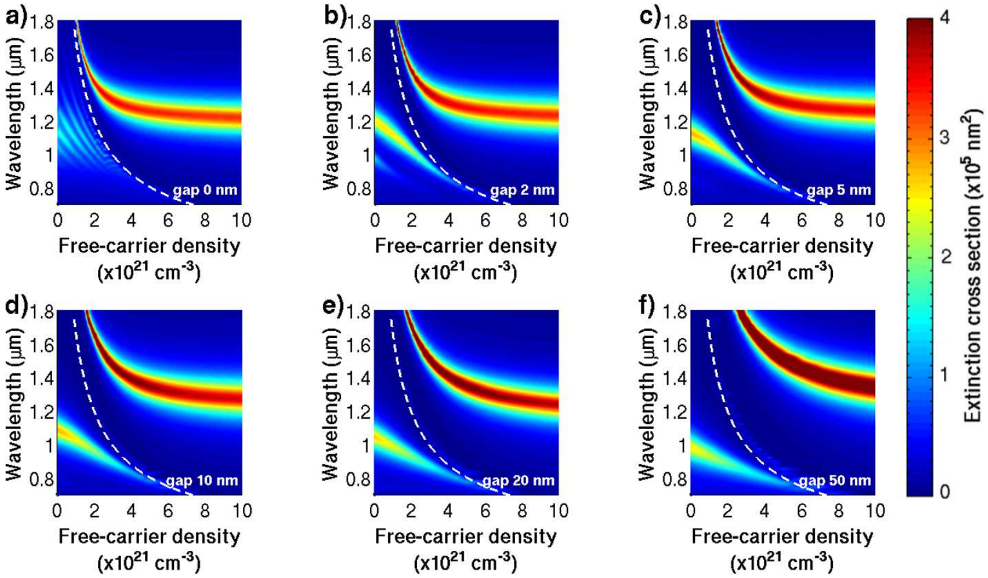

Figure 5.3: Color density maps of the antenna spectral response as a function of photoexcited free-carrier concentration N_{eh}, for antennas with gap sizes 0 nm (a), 2 nm (b), 5 nm (c), 10 nm (d), 20 nm (e) and 50 nm (f).

therefore the gap becomes less conductive, this mode would present net charge in one of the arms of the antenna and negative in the other. As this configuration is not physically possible, this modes shifts dramatically to longer wavelengths, and eventually damps and dies out [157; 164]. We point out that the spectral mode in the strongly dispersive regime is relatively narrow, which indicates a reduced damping of this mode. As a consequence of the strong wavelength dependence of N_{eh}^{crit}, the antenna can be simultaneously switched and unswitched in different parts of the spectrum. In this transitional regime, the antenna supports both conductively coupled modes at longer wavelength and capacitive modes at shorter wavelengths, which could be of interest for device applications.

The $S = 50$ nm gap width (Figure 5.3f) represents the virtually uncoupled regime, where capacitive interaction is very weak. For these wide-gap antennas, the far-field photoconductive switching effect is the strongest, firstly because of the absence of the redshift associated with capacitive coupling, and secondly because the total antenna length is the largest, leading to a longer wavelength fundamental mode. In comparison, for the $S = 2$ nm antenna (Figure 5.3b), switching from the capacitive to conductive state does not produce a marked wavelength shift. For the $S = 0$ nm antenna (Figure 5.3a), the presence of a conductive singularity results in a strongly renormalized mode structure [157].

Photoconductive antenna switching in this case strongly modifies the conductive area between the antenna arms, allowing a proper antenna mode to be formed.

5.1.3 Photoconductive near-field switching

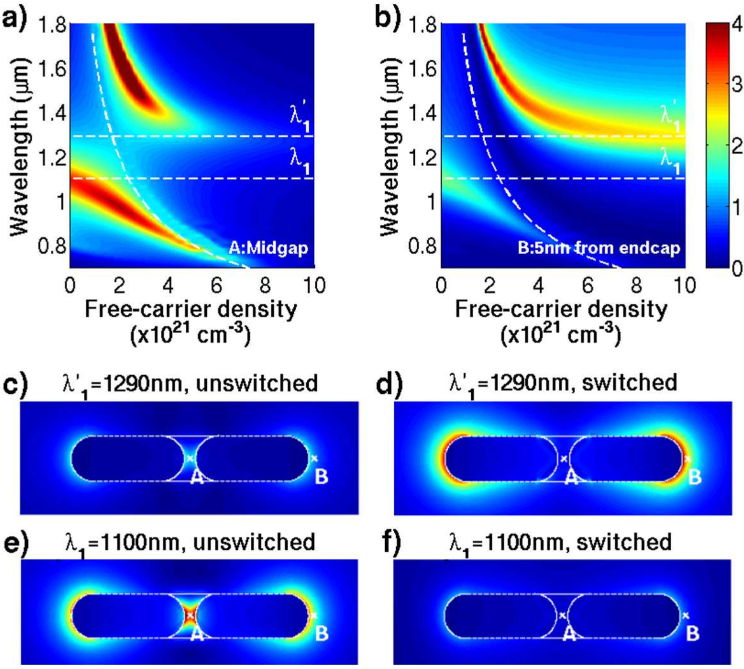

Figure 5.4: Near-field intensity maps calculated for an antenna of $L = 100$ nm arm length and $S = 10$ nm gap size, as function of wavelength and free-carrier density, for the antenna midgap (a) and 5 nm away from the antenna arms (b). (c-f) Near-field intensity maps around the antenna of (a) for resonance wavelength λ_1'(c, d) and λ_1 (e, f), under unswitched ($N_{eh} = 0$ cm^{-3}) (c, e) and switched ($N_{eh} = 10^{22}$ cm^{-3}) (d, f) conditions.

Together with the switching of the far-field radiative properties, active control over the near-field distribution and the associated local density of states will be of enormous importance. The near-field intensity has been calculated at various positions around a photoconductive antenna switch. Figures 5.4a and 5.4b show the intensity at the center of the antenna gap and 5 nm from the antenna ends for a dimer antenna with $S = 10$ nm gap width. This narrow-gap antenna supports a fundamental mode at a wavelength $\lambda_1 = 1100$ nm with a high local intensity enhancement of around 35 times the incident intensity in the gap region. The mode-profile of this antenna resonance can be observed in detail in the near-field maps of Figures 5.4e and 5.4f. Photoconductive switching of the antenna results in a strong quenching of the midgap intensity by an order of magnitude, due to the redistribution of charges associated with the suppression of the gap capacitor (Figure 5.4f). A new mode is formed at a wavelength $\lambda_1' = 1290$ nm, where the intensity is mainly concentrated around the endpoints of the antenna and the midgap intensity is absent (Figure 5.4d). Remarkably, Figure 5.4a shows that a transitional regime exists above N_{eh}^{crit} where the new mode shows a large midgap intensity, even exceeding that of the purely capacitive antenna. It should be noted that here the semiconductor still is partly dielectric, as otherwise the fields in the gap would be suppressed. The physical origin of this enhancement is again related to the particular charge distribution in the antenna in the cross-over regime as discussed above.

5.1.4 Figures of merit

For the rational design of antenna switches, figures of merit of antenna performanceare defined for respectively far-field extinction and near-field intensity enhancements. For applications requiring large spectral shifts and extinction contrast, the relative resonance shift $(\lambda_1' - \lambda_1)/\lambda_1$ and the on-off extinction ratio $\sigma_{\text{on}}/\sigma_{\text{off}}$ at λ_1 and λ_1' are calculated. For the near-field switching, key parameters of interest are the on-off ratios of the local intensity at the midgap and antenna end positions A and B respectively. Resulting values are shown in Figures 5.5a and 5.5b for the antennas with various gap widths. The increasing capacitive loading for decreasing gap width S drives the individual particle resonances λ_1 toward that of the half-wave antenna λ_1' [129], resulting in a reduced far-field switching performance. Therefore, for far-field switching, antennas with a large gap are favorable for achieving a large spectral shift and high switching contrast. We should bear in mind though that antennas with a large gap require more energy for switching and do not benefit as much from reduced switching thresholds at antenna resonances. For the near-field switching, antennas with a narrow gap are more favorable as they produce higher local field enhancements. Active manipulation of the local near-fields around plasmonic nano-antennas will be of importance for applications involving coherent control over local field amplitudes and phases [2] and for active manipulation of quantum emitters [7].

The free-carrier densities required for nano-antenna switching at near-infrared wavelengths are higher than those in the terahertz range [34; 77]. However such densities are routinely achievable using ultrafast laser excitation of an electron-hole plasma. [54; 170] In order to compare the switching energies required for photoconductive antenna switch-

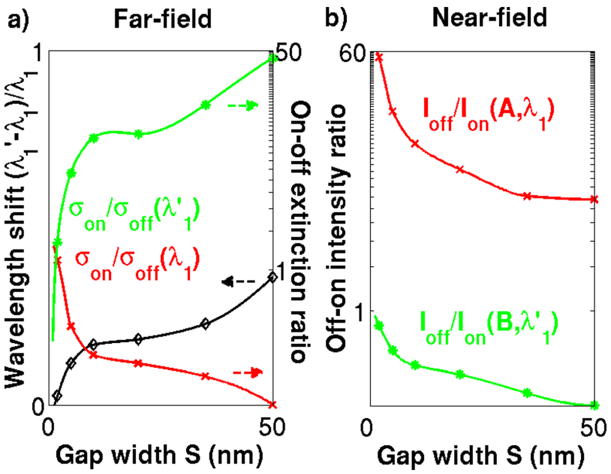

Figure 5.5: Figures of merit for switching operation in far-field (a) and near-field (b). (a) Relative resonance shift $(\lambda_1' - \lambda_1)/\lambda_1$ (left scale bar) and on-off extinction ratios $\sigma_{\mathrm{on}}/\sigma_{\mathrm{off}}$ at wavelengths λ_1 and λ_1' (inverse off-on ratio), versus antenna gap width S. (b) Near-field intensity off-on ratios $I_{\mathrm{off}}/I_{\mathrm{on}}$ at λ_1, point A (midgap) and λ_1', point B (5 nm from tip, inverse off-on ratio).

ing with state-of-the-art microphotonic devices, the pumping energies has been estimated for direct and 2-photon optical excitation. In this estimate, dynamical effects occurring on the timescale of the optical pump pulse, which will be discussed further below, were not considered. For pulsed optical excitation on a time scale much shorter than carrier relaxation process in the system, the free-carrier density N_{eh} can be estimated from the incident optical fluence F_0 using [81]

$$N_{eh} = \frac{F_0}{\hbar\omega}\left(\alpha_0 + \frac{\beta F_0}{2\sqrt{2\pi}t_0}\right), \tag{5.3}$$

where $\omega = 2\pi/\lambda$, α_0, and β are the linear and two-photon absorption coefficients, and t_0 the time duration of the pulse. For excitation of a-Si in the telecommunication range using an ultrafast laser, a critical density N_{eh}^{crit} of around 10^{21} cm^{-3} is achieved via two-step absorption ($\beta \approx 120$ cm/GW) at a fluence of $F_0 = 0.73$ mJ.cm^{-2} [81]. Similar switching fluences are obtained using linear absorption above the bandgap, where $\alpha_0 > 10^5$ cm^{-1} [54]. For excitation using a diffraction-limited spot of around 1 μm^2 area, the above fluence gives a switching energy of 7.3 pJ. This compares well to values achieved using microphotonic ring resonators [9] and photonic crystal nanocavities [176], which are however intrinsically several orders of magnitude slower than plasmonic devices [114]. The above switching energies are valid for ultrafast pulsed excitation. Under stationary pumping conditions, the carrier density will be limited by different relaxation mechanisms such as surface recombination, Auger processes, and electron diffusion. The ultrafast response of a-Si thin films has been extensively studied by Esser *et al.* [54], who have shown that carrier densities in the 10^{21} cm^{-3} can be achieved using ultrafast laser absorption. Carrier-trapping into localized states leads to a considerable reduction of the free-carrier lifetime for a thin film compared to bulk crystalline Si. Above densities of 8×10^{19} cm^{-1} another contribution to the relaxation time appears due to Auger processes involving spatially overlapping electron-hole pairs. The combined processes result in a relaxation time of the order of 100 fs at carrier densities around 10^{21} cm^{-3} [54]. An additional limiting factor to the carrier concentration is carrier diffusion out of the gap region. For a 20 nm gap region and an electron diffusion constant of 36 $\mathrm{cm}^2.\mathrm{s}^{-1}$, electron diffusion will contribute to a relaxation time of around 100 fs.

These relaxation processes limit the carrier density that can be achieved using stationary excitation; however they also provide the ultrafast time response of the nano-antenna switch. Eventually all the energy deposited into the system will be converted into heat by electron-phonon relaxation on a time scale of picoseconds [131]. In the extreme case that all this energy is dissipated entirely in the nano-antenna, it produces a temperature rise of around 30 K. For this calculation, the lattice heat capacity of gold $C_L \simeq 2.5 \times 10^6$ $\mathrm{J/m^3K}$ and a total amount of 10^6 generated electron-hole pairs per antenna and per pump pulse has been used. Effects of heat piling up can be substantially reduced by embedding the antenna into an environment with a good thermal conductivity.

The combination of strong optical resonances with a high local field enhancement in the antenna gap opens up opportunities for optical pumping employing the mode structure and its dynamic modulation. Since only a nanometer-sized active volume has to be pumped, which is strategically located in the antenna gap, the estimated pump intensity required for switching can be significantly reduced through funneling of pump energy into the resonant antenna mode. Considering a typical resonant intensity enhancement in the antenna gap of order 10^2 [4; 129], an ultimate switching energy is estimated around 100 fJ. In addition, it may be possible to employ the strong resonant enhancement of nonlinear optical phenomena in the feed gap, such as second harmonic and supercontinuum generation [129; 165], to produce a nonlinear absorption complementary to two-step absorption. The above resonant reduction of the pumping threshold assumes that this energy can be deposited into the resonant mode before the switching itself changes the antenna mode structure. In the other limit of stationary resonant pumping, the dynamic switching of the antenna will result in optically bistable behavior [1]. We propose that the nano-antenna switch can thus be used as a saturable absorber element. This application may hold substantial promise for semiconductor lasers, which currently operate in the sub-100 fs pulsed regime [153]. The exact conditions for successful operation of plasmonic saturable absorbers will require extensive modeling which goes beyond the work presented in this thesis.

5.2 Gold ring-based nanoresonators

Among the wide variety of plasmonic nanoresonators, ring-disks are very interesting nano-objects because they allow for a high tunability of the LSPR owing to the interaction between the nanoring walls [5; 19; 71; 73; 101; 136; 173]. Moreover, it has been shown that small structural symmetry breaking of such nano-objects leads to strong variations of the LSPRs [72; 73; 171]. In this section, the dependence of the surface plasmon properties of ring-disks on fine shape details, namely the wall sharpness and profile of the nanoring and of the nanodisk are investigated experimentally and numerically. A comparison between numerical and experimental results, combined with high-resolution scanning electron microscopy (HRSEM) and atomic force microscopy (AFM) is presented.

5.2.1 Nanofabrication and optical measurements

Two gold nanoring-disk samples NRD240 and NRD280, consisting in periodic arrays of concentric nanodisk (ND) and nanoring (NR), have been studied. The samples were fabricated using a protocol combining electron beam lithography (EBL) and thermal evaporation of Au(25 nm)/Cr(3 nm) on quartz substrates [107; 178; 181]. The ND and NR have a nominal height of h =28 nm and were processed on a 100 μm $\times$100 μm area. Figure 5.6 shows HRSEM (a), AFM (b, d) images, and an AFM profile scan (c) of a typical nanoring-disk. The average size parameters extracted from the HRSEM and AFM measurements are quoted in Table 5.1. The axis to axis separation between ring-disks is 480 nm and 560 nm for samples NRD240 and NRD280, respectively. For such large separation, the electromagnetic near-field interactions between adjacent ring-disks can be neglected [157].

The fine details of the shape of a typical ring-disk are revealed by the AFM measurements (Figures 5.6c and 5.6d). The fabrication process leads to two main features: i) the side walls of the NR and ND are not vertical but slightly tilted, ii) the NR and the ND do

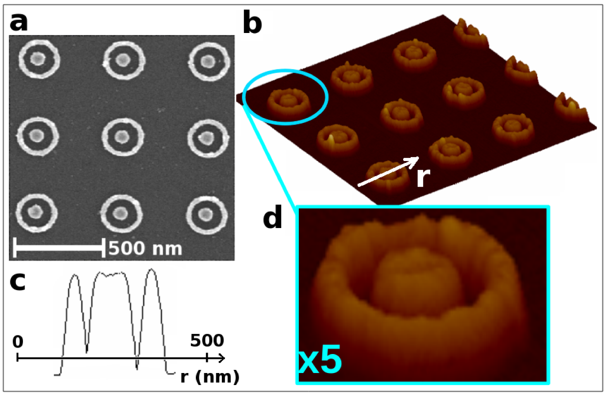

Figure 5.6: HRSEM (a) and AFM (b, d) images of the NRD240 ring-disk sample. AFM profile scan (c) of a typical ring-disk.

Table 5.1: Average size parameters from samples NRD240 and NRD280. $D_{NR,out}$, $D_{NR,in}$ and w are the outer and inner diameters and wall thickness of the NR, respectively. D_{ND} is the nanodisk diameter. The pitch, i.e. axis to axis separation between nanoring-disks, is also indicated.

Samples	$D_{NR,out}$ (nm)	$D_{NR,in}$ (nm)	w (nm)	D_{ND} (nm)	Pitch (nm)
NRD240	240 ±3	180 ±3	30 ±3	90 ±3	480
NRD280	280 ±3	202 ±3	39 ±3	112 ±3	560

not present the ideal profile characterized by flat surfaces and sharp edges. They rather exhibit a rounded surface on top and smooth edges. Defects resembling small bumps and craters on the top of the ring-disk are also visible. One must keep in mind that the AFM resolution is limited by the tip size and by the response time of the experimental setup. The AFM image and topography profile in Figures 5.6d and 5.6c were acquired at low speed ($\tilde{v}_{tip} \approx 5\ \mu$m/s) in order to reduce those limitations.

Figure 5.7 shows the optical density (OD) spectra of samples NRD240 and NRD280 obtained as $OD = -\log(T)$, where T is the measured transmittance. Spectra were recorded in the 400-1700 nm spectral range and do not extend further into the infrared due to limitation of the spectrophotometer. The incident light was unpolarized. The transmitted light was collected through a 36X long working distance microscope objective with 0.5 numerical aperture. The probed area is around 250 μm^2 located at the center of the 100 μm $\times$100 μm processed area. The number of probed nano-objects is about 1100 and 800 in the case of ring-disks separated by 480 nm and 560 nm, respectively. As observed in Figure 5.7, the OD spectra exhibit two resonances: one in the visible (around 670 nm) and another in the infrared (around 1550 nm and 1700 nm, depending on sample) which are associated to disk-like and ring-like LSPRs, respectively [71; 137; 151; 190]. The measured LSPR wavelengths and linewidths are quoted in Table 5.2. The ring-disks showed a good uniformity as attested by the weak dependence of the LSPR wavelengths on the probed point of the 100 μm $\times$100 μm area.

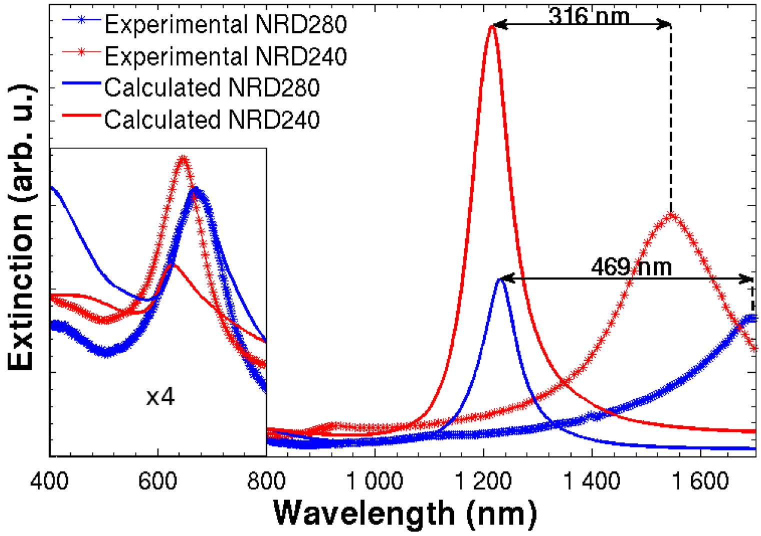

Figure 5.7: Experimental (dots) and calculated (full lines) spectra of the NRD240 (red) and NRD280 (blue) nanoring-disk samples. The BEM simulations assume perfect ring-disks with NR and ND showing flat surfaces and sharp edges. The scale in the range 400-800 nm is multiplied by a factor of 4.

5.2.2 Simulations and comparison with experiments

To compare the experimental results with the calculations, the surface plasmon properties of ring-disks have been calculated using the boundary elements method (BEM) [4; 5; 61; 62]. The bulk dielectric function of gold used in the calculations has been taken from Johnson and Christy [84]. Calculations were performed for a single ring-disk with characteristic dimensions corresponding to samples NRD240 and NRD280 (cf. Table 5.1). The ring-disk is located on the top of a quartz substrate (optical index from Reference [182]), and the incident electric field $\vec{E}_i$ is propagating at normal incidence with polarization in the plane of the ring-disk. The 3 nm-Cr layer (optical index from Reference [143]), that allows for improving the attachment of the ring-disk to the quartz substrate, is taken into account in the simulations.

The spectra presented in Figure 5.7 were calculated for a perfect ring-disk, i.e. for NR and ND with sharp edges and flat surfaces as sketched in Figure 5.8a. The wavelength of the disk-like LSPR is correctly described by the calculations (cf. Table 5.2). On the contrary, the discrepancy between measured and calculated wavelengths of the ring-like LSPR is considerable. Indeed, the ring-like LSPR measured for samples NRD240 and NRD280 are red-shifted by 316 nm and 469 nm, respectively, in comparison with the calculated LSPRs (Figure 5.7). Such differences cannot be explained by variations in the ND and NR sizes. Indeed, it would be necessary to double the NR diameter in order to account for the measured ring-like LSPR wavelengths.

Since the ring walls are here very thin (30 nm and 39 nm for NRD240 and NRD280, respectively), their actual shape may strongly influence their surface plasmon resonances. In particular, the ring walls exhibit a rounded shape on top, rather than being ideally flat, as observed by AFM imaging and topography profiles (Figures 5.6c and 5.6d). Therefore, ring-disks with more realistic profiles, i.e. shapes mimicking those observed by AFM, are considered (Figure 5.8b). Instead of being vertical and sharp, the NR and ND walls are now tilted and have a rounded shape on top.

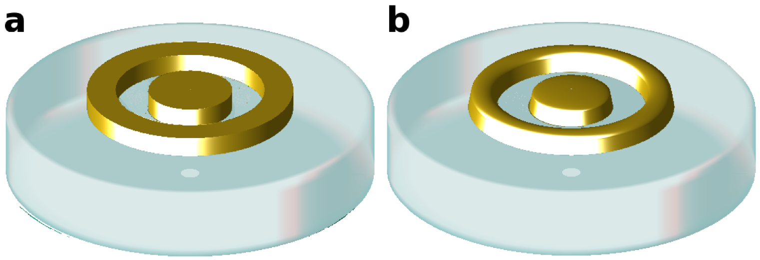

Figure 5.8: Model profiles of ring-disks (a) with flat surfaces and sharp edges, and (b) with rounded surfaces and smooth edges.

Figure 5.9 presents extinction spectra of NRD240 and NRD280 ring-disks simulated for various ND and NR profiles. The disk-like LSPR λ_{ND} is only slightly affected by the change in shape: a maximum red-shift of only 11 nm with respect to the ideal sharp profile is found. Intuitively, this can be understood in terms of small shape deformation compared to the large disk size (either 90 nm or 112 nm in diameter). On the contrary, the infrared ring-like LSPR λ_{NR} red-shifts by several hundreds of nanometers with increasing

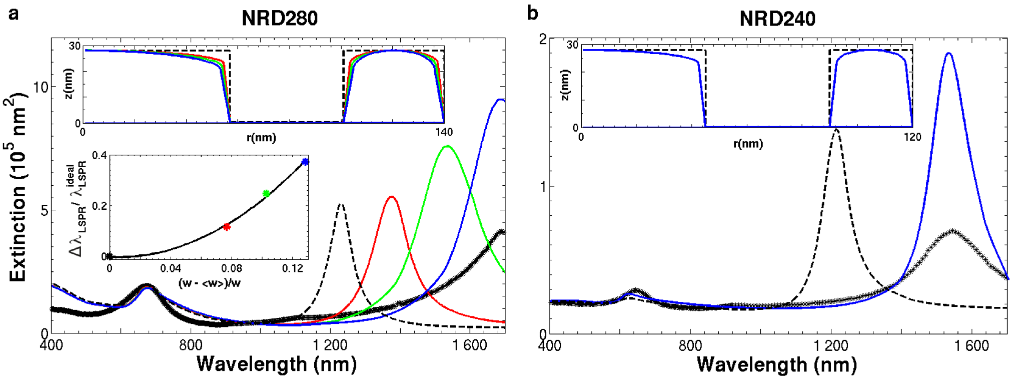

Figure 5.9: Extinction spectra of NRD280 (a) and NRD240 (b) calculated for the various profiles of the ring-disks shown in the insets (only half the ring-disk is sketched). The spectrum corresponding to each profile is color-encoded. The profiles of the perfect ring-disks with sharp edges and flat surfaces and the corresponding spectra are shown in black dashed lines. The measured optical density spectra $[OD = -\log(T)]$ are plotted with black dots. The inset in panel (a) shows the relative LSPR shift $\Delta\lambda/\lambda_{LSPR}^{\mathrm{ideal}}$ as a function of the relative deviation of the mean NR wall thickness $(w - \langle w\rangle)/w$.

deformation (Figure 5.9a). This significant spectral shift is directly connected to the interaction between inner and outer NR walls [5]. Indeed, by rounding the ring, both walls are slightly tilted and so result in a decrease of the mean wall thickness, thus leading to an increase of the inter-walls interaction. The smoother the edges are, the thinner the ring is, and the stronger the interaction becomes. This is the reason why the ring-like LSPR red-shifts when the rounded shape of the NR becomes more and more pronounced. The inset in Figure 5.9a shows the dependence of the relative spectral shift of the LSPR $\Delta\lambda/\lambda_{LSPR}^{\mathrm{ideal}}$, $\lambda_{LSPR}^{\mathrm{ideal}}$ being the LSPR wavelength of the ideally flat ring-disk exhibiting sharp edges, as a function of the deviation of the mean NR wall thickness $\langle w\rangle$ from the nominal wall thickness w of the ideal NR. It can be noticed from this figure of merit that a 10% decrease of the mean wall thickness induces a 25% spectral red-shift of the ring-like LSPR. The strong sensitivity of the ring-like LSPR to small shape variations is due to the small ring wall thickness (either 30 nm or 39 nm). This point is specifically addressed further with the near-field study. Figure 5.9b presents a comparison between the measured optical density (OD) spectrum and the extinction spectra calculated for both the ring-disk with sharp edges and the ring-disk with the rounded shape that accounts for the observed ring-like LSPR wavelength. This comparison is presented for sample NRD240 for which the infrared ring-like LSPR is clearly observed. The calculated LSPR wavelengths and linewidths are quoted in Table 5.2.

Table 5.2: Calculated and measured LSPR wavelengths λ and linewidths Γ from the two ring-disk samples: NRD240 and NRD280. The accuracy of the wavelength determination is ±2 nm.

	NRD280				NRD240			
	λ_{ND} (nm)	Γ_{ND} (nm)	λ_{NR} (nm)	Γ_{NR} (nm)	λ_{ND} (nm)	Γ_{ND} (nm)	λ_{NR} (nm)	Γ_{NR} (nm)
Measured	676	115	~1700	~300	645	88	1546	223
Calculated	675	87	1688	210	630	61	1530	117

The experimental spectra are acquired from 1100 and 800 ring-disks in case of samples NRD240 and NRD280, respectively (cf. Section 5.2.1). The quantitative analysis of the ring-like LSPR allows for determining the average shape of those probed ring-disks as shown in Figure 5.9. Furthermore, it is interesting to notice that the calculated ring-like LSPR is narrower and nearly three times more intense than the measured LSPR (Table 5.2 and Figure 5.9b) in case of sample NRD240. This difference can be attributed to the fact that the bulk dielectric function of gold is used in the simulations whereas our ring-disks present a high surface to volume ratio, which deviates from the bulk approximation. Moreover, size and shape fluctuations of the ring-disk as well as the roughness (bump and crater defects) visible in the AFM images (Figures 5.6b and 5.6d) have already been studied [140]. It has been shown that a distribution of about 360 bumps and craters with diameters ranging from 8 nm to 20 nm on the surface of a nanoshell induces a spectral red-shift of about 20 nm and contributes to the inhomogeneous broadening of the LSPR. The eccentricity of the ring-disks has also been studied both experimentally and theoretically [72; 73; 171]. A 17 nm displacement of the ND with respect to the NR center induces a spectral red-shift of the order of 25 nm. Considering the good quality of the studied samples, and the relatively small influence of the two effects (relative spectral shifts of the order of 2%), it is possible to conclude that neither the presence of some defects (bumps and craters) nor the very small eccentricity of the ring-disks can be responsible for the significant spectral shift of the ring-like LSPR reported here.

Figure 5.10 compares the model profiles, extracted from the quantitative analysis of the extinction spectra (cf. Figure 5.9), to the top part of the AFM profiles (cf. Figure 5.6). The latter were obtained by averaging AFM-profile scans measured from 10 ring-disks of samples NRD240 and NRD280 (green full line). The general feature of the realistic rounded ring-disk profiles (blue dashed line) is in good agreement with the measured topography profiles (green full line). In particular, the rounded shape of the NR top surface is well accounted for, though the actual AFM profiles appear broader due to

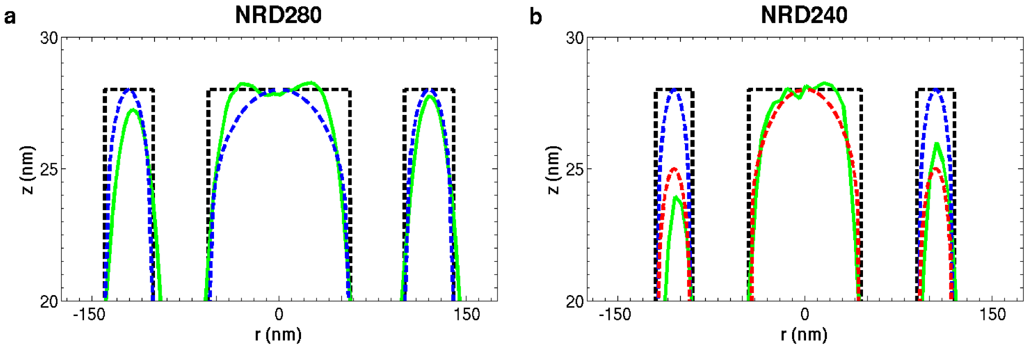

Figure 5.10: Top part of the average AFM topography profiles (green lines) and of the model ring-disk profiles having both flat surfaces with sharp edges (black dashed lines), and rounded surface with smooth edges (blue dashed lines) for both samples NRD280 (a) and NRD240 (b). For NRD240, a profile with h_{NR} =25 nm< h_{ND} =28 nm is also shown in red dashed line.

experimental limitations, specially at the ring-disk base (cf. Section 5.2.1). However, the HRSEM image (cf. Figure 5.6a) shows a clear gap between the NR and the ND, thus supporting this AFM resolution limit. From the simulations, it has been found that a 3 nm broadening of the NR base (corresponding to the experimental accuracy) leads to a blue-shift of the ring-like LSPR of about 15 nm. This value is much smaller than the shift induced by the rounded shapes (Figure 5.9). Furthermore, it can be noticed that for NRD240, the experimental NR height (h_{NR}) is slightly lower than that of the ND (h_{ND}). The calculations performed with a profile taking into account this mismatch (h_{NR} =25 nm< h_{ND} =28 nm, red dashed line in Figure 5.10b) show that the ring-like LSPR red-shifts by only 30 nm (with respect to the LSPR obtained with the ideal profile). Indeed, since the ring-like surface plasmon modes are related to the inter-walls interaction, the LSPRs only weakly depend on the NR and ND height fluctuations.

It is worthwhile to determine the impact of the ring-disk shape on the surface plasmon near-field distribution. To do so, the local field enhancement $|\vec{E}_{loc}|/|\vec{E}_i|$ has been calculated for both ring-disks with sharp edges and ring-disks with the rounded shape that accounts for the observed LSPRs (blue dashed line in Figure 5.10). The results are presented in Figure 5.11 for the ring-disk NRD240. The near-field distributions are shown for resonant excitation of the disk-like (Figures 5.11a and 5.11b) and ring-like (Figures 5.11c and 5.11d) LSPRs. For resonant excitation with the visible LSPR, only the dipolar surface plasmon mode of the ND is activated, thus supporting the disk-like nature of this LSPR. Similarly, the resonant excitation of the infrared LSPR generates a strong field localization around the NR. This surface plasmon mode corresponds to the interaction between the NR walls. Moreover, part of the local field is also localized within the NR-ND gap due to the interaction between the NR and the ND. The spatial distributions of the near-field intensity around the NR support the ring-like nature of the surface plasmon modes. Though slight amplitude changes can be noticed in Figures 5.11c and 5.11d, when rounding the NR and ND shapes, the general feature is preserved. These little changes arise from the sharpness of the NR edges. Indeed, in the sharp NR, there is a strong surface charge density localization on top of the NR sustained by the edges, while in the rounded NR it is quasi-uniformly distributed all over the NR wall. This effect reflects in the near-field distribution (upper panels in Figures 5.11c and 5.11d). Furthermore, it is worthwhile to notice that the electric near-field is more localized around the ring-disk with rounded surfaces and smooth edges (Figure 5.11d) due to stronger NR inter-wall interaction (as compared to Figure 5.11c). Figure 5.11e shows the near-field distribution around the ring-disk with smooth edges and rounded surfaces with an incident wavelength in resonance with the LSPR of the ring-disk presenting sharp edges and flat surfaces ($\lambda_{LSPR}^{\mathrm{ideal}} = 1214$ nm). From these near-field maps it can be noticed that the excitation is now out of resonance (lower local field enhancement) and that the ring-like behavior is lost (near-field more localized within the NR-ND gap). Indeed, the LSP mode excited at 1214 nm is now the result of a mixing between the disk-like and the ring-like LSPRs.

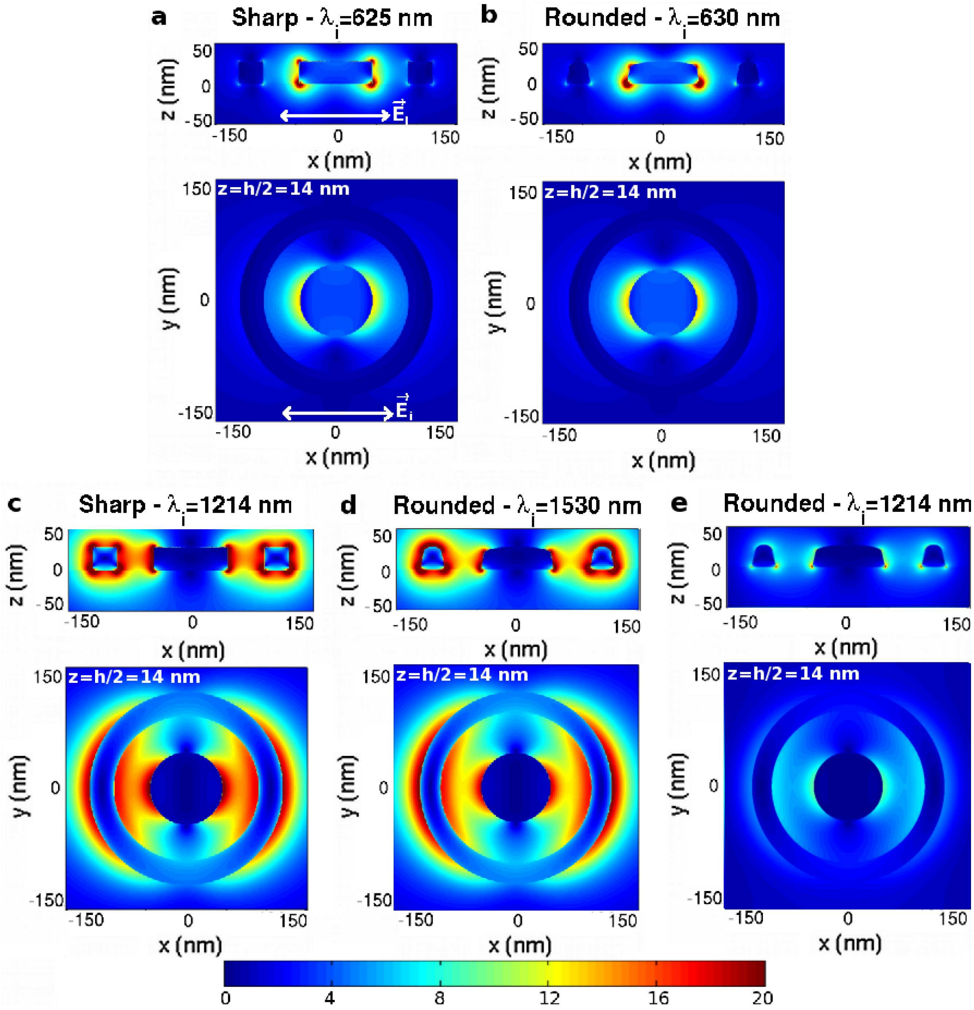

Figure 5.11: All the upper panels show a side view at $y = 0$ and all the lower panels show a top view at $z = h/2 = 14$ nm of the calculated near-field distributions for both sharp (a, c) and rounded (b, d) ring-disks (NRD240) associated to both disk-like (a, b) and ring-like (c, d) LSPRs. Panel (e) shows the near-field distribution around the rounded ring-disk (NRD240) excited in resonance with the ring-like LSPR of the sharp ring-disk. The white arrow indicates the polarization of the incident field $\vec{E}_i$ which propagates along the z-direction. The color scale refers to the field enhancement factor $|\vec{E}_{loc}|/|\vec{E}_i|$.

Chapter 6

Acousto-Plasmonic Dynamics and Raman-Brillouin Scattering

Contents

Localized surface plasmons have been extensively studied both theoretically and experimentally in objects and nanostructures [4; 105; 137; 138; 155; 157; 175; 192]. Only few experimental techniques address the dynamics of surface plasmons of vibrating nano-objects. In this section I report on the importance of analyzing the interaction between localized surface plasmons and acoustic vibrations for understanding of their inelastic light scattering properties, in particular resonant Raman-Brillouin scattering [15; 116].

6.1 Raman-Brillouin scattering in metals

In metallic nanostructures, surface plasmons play the role of intermediate states in the three-steps resonant Raman-Brillouin scattering process [17]: absorption of the incident photon, absorption or emission of a vibration mode and emission of the scattered photon. The scattering rate intoduced in Equation 2.1 is now expressed for localized surface plasmons:

$$\mathcal{P}(\vec{k}_i, \vec{k}_s) = \tfrac{2\pi}{\hbar}\delta(\hbar\omega_s \pm \hbar\omega_{vib} - \hbar\omega_i) \times \tag{6.1}$$
$$\left|\sum_{a,b} \frac{\left\langle n_{\vec{k}_s}+1, n_b \middle| H^s_{pl-pht} \middle| n_{\vec{k}_s}, n_b \right\rangle \langle n_b+1, n_a | H_{pl-vib} | n_b, n_a+1 \rangle \left\langle n_{\vec{k}_i}, n_a+1 \middle| H^i_{pl-pht} \middle| n_{\vec{k}_i}+1, n_a \right\rangle}{(\hbar\omega_s - \hbar\omega_b + i\Gamma_b)(\hbar\omega_i - \hbar\omega_a + i\Gamma_a)}\right|^2,$$

where $n_{\vec{k}_{i(s)}}$ is the number of incident (resp. scattered) photons with wavevector $\vec{k}_{i(s)}$ and energy $\hbar\omega_{i(s)}$. $n_{a(b)}$, $\hbar\omega_{a(b)}$ and $\Gamma_{a(b)}$ are the occupation numbers, energy and homogeneous broadening of the intermediate localized surface plasmon states (labelled a and b) involved in the optical absorption and emission steps. $H^{i(s)}_{pl-pht}$ is the interaction Hamiltonian between the LSP and the incident (resp. scattered) light. H_{pl-vib} is the interaction Hamiltonian between the localized surface plasmons and the acoustic vibrations and is given by [17; 100]:

$$\langle n_b + 1, n_a | \, H_{pl-vib} \, | n_b, n_a + 1 \rangle = - \int_{NCl} \vec{E}_b(\vec{r}) \cdot \delta_{vib} \vec{P}_a(\vec{r}) dV, \tag{6.2}$$

where $\delta_{vib}\vec{P}_a(\vec{r})$ is the modulation of the optically excited polarization by the acoustic vibrations and $\vec{E}_b(\vec{r})$ is the electric field of the LSP state b emitting the scattered photon.

6.1.1 Deformation potential coupling mechanism

Starting from $\vec{P}_a = \epsilon_0 \chi \vec{E}_a$, the modulation of the induced polarization can then be expressed as [15; 17]:

$$\delta_{vib}\vec{P}_a(\vec{r}) = \epsilon_0 \delta_{vib}\chi(\vec{r})\vec{E}_a(\vec{r}) + \epsilon_0 \chi(\vec{r})\delta_{vib}\vec{E}_a(\vec{r}). \tag{6.3}$$

The first component of Equation 6.3, i.e. $\epsilon_0 \delta_{vib}\chi(\vec{r})\vec{E}_a(\vec{r})$, is called Deformation Potential coupling mechanism. Similar to the DP coupling mechanism introduced for semiconductors in Chapter 2, the modulation of the interband dielectric susceptibility χ_{inter} contributes to the modulation of the optically induced polarization. In principle, both intraband and interband components of the dielectric susceptibility may be modulated via DP mechanism. However, because the single particle intraband excitations fall in the infrared range, the effect of their interaction with acoustic vibrations on the collective intraband response is negligible in the visible range [17]. The contribution of the DP coupling mechanism to the modulation of the induced polarization is then given by:

$$\delta_{vib}\vec{P}_a^{DP}(\vec{r}) = \epsilon_0 \chi_{inter}(\vec{r}) \left(\frac{D_{e-vib}}{\hbar\omega - \hbar\Omega_{inter}} \text{div } \vec{u}_{vib}(\vec{r}) \right) \vec{E}_a(\vec{r}), \tag{6.4}$$

where $\vec{u}_{vib}$ is the displacement field associated to the acoustic vibration, $\hbar\Omega_{inter}$ is the interband transition energy, and D_{e-vib} is the deformation potential [15; 17].

6.1.2 Surface orientation coupling mechanism

The second term in Equation 6.3, i.e. $\epsilon_0 \chi(\vec{r})\delta_{vib}\vec{E}_a(\vec{r})$, is related to the modulation of the induced electric field by changes in size and shape of the nano-object. Due to a change in shape, induced by acoustic vibrations, the surface charge density of the metallic nano-object is redistributed at the surface of the nano-object. The electric field changes both in amplitude and in direction. This acousto-plasmon interaction considered here is called Surface Orientation (SO) coupling mechanism. It has been proposed by Guillaume Bachelier and Adnen Mlayah and introduced in a perpurbation approach [15; 17].

6.2 Acousto-Plasmonic dynamics in silver nanocolumns

6.2.1 Silver nanocolumns growth

Ag:Al_2O_3 nanocomposite thin films containing silver NCls were produced on glass substrates by alternate pulsed laser deposition (a-PLD) [29; 116] of Ag nanoparticles and amorphous Al_2O_3 layers (a-Al_2O_3). When the thickness of the a-Al_2O_3 layers is reduced down to a critical value, Ag nanoparticles nucleate preferentially on top of nanoparticles of the previous layers, leading to the formation of self-aligned silver NCls [116], as observed in the TEM image in Figure 6.1a. Three silver nanocolumn samples, with mean lengths of 6.5 nm, 12 nm and 13 ± 0.2 nm (labelled NCls1, NCls2 and NCls3, respectively) and a mean diameter of 2.5 ± 0.2 nm were studied.

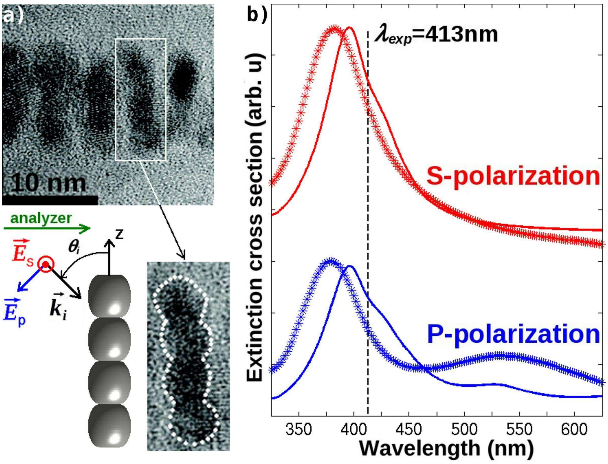

Figure 6.1: (a) TEM image cross section of the NCls and schematic of the incident light wavevector ($\vec{k}_i$) and electric fields for S- and P-polarizations. The green arrow indicates the direction onto which the scattered light is analyzed. The angle between the incident wavevector and the NCl axis is $\theta_i = 34.5°$ inside the sample. A zoom of the TEM image shows a typical NCl formed by a stacking of quasispherical NPs. This stacking is modeled by an indented NCl as displayed in the schematics. (b) Calculated (full line) and measured (stars, sample NCls2) extinction spectra for P-polarized (blue) and S-polarized (red) light. The Raman excitation wavelength (413 nm) is marked on the graph as a dashed line.

Optical extinction spectra from NCls2 were measured for both P and S incident polarizations. The experimental spectra in Figure 6.1b show a transverse localized surface plasmon resonance (around 375 nm) [108] visible for P- and S-polarizations (cf. schematics of incident polarization in Figure 6.1a), and a red-shifted broad band which has been already assigned to the longitudinal surface plasmon resonance [116] of the nanocolumns. The latter is only observed for P-polarization [117]. The longitudinal-transverse surface plasmon splitting reveals the elongated nature of these nano-objects, consistent with the TEM images.

6.2.2 Raman-Brillouin scattering and pump-probe experiments

Low frequency Raman-Brillouin scattering by confined acoustic vibrations was excited using the $\lambda_i = 413$ nm krypton laser wavelength close to the transverse surface plasmon resonance (dotted line in Figure 6.1b). The scattered light was dispersed using a customized T64000 Jobin-Yvon spectrometer which allows for low-frequency Raman-Brillouin measurements with a very high rejection of the Rayleigh scattering.

Figure 6.2 shows the Raman-Brillouin spectra recorded from the three NCls samples (NCls1, NCls2, NCls3) and from a sample consisting of five well separated layers of isolated spherical nanoparticles (NPs) grown on a Si substrate. Both P- and S-polarizations of the incident light have been used, whereas the polarization of the scattered light has been analyzed in the horizontal direction in the plane of incidence. This scattering configuration, together with the identical orientation of all the NCls allow for tracing the activation of different vibrational modes (selection rules).

The Raman-Brillouin spectra of the NCls consist of a main peak located around 23 ± 2 cm^{-1} which has been previously ascribed to scattering by quadrupolar-like confined acoustic vibrations [29; 116] (a sketch of the associated displacement field is shown in Figure 6.2). As observed in the spectra of NCls1, NCls2 and NCls3, the frequency of the quadrupolar-like Raman band is basically independent on the NCls length, with very small shifts due to differences in the lateral average dimensions of the nanocolumns. The extensional vibration mode of the NCls (shown in the sketch of Figure 6.2) can be observed only in time resolved pump-probe experiments [28; 29]. The femtosecond time resolved transient absorption measurements were performed using the pump-probe technique (excitation at 860 nm and detection at 430 nm) [29]. Only the result obtained for NCls2 is presented here for comparison with the Raman-Brillouin data. The Fourier transform (FT) of the transient absorption oscillations from NCls2 (top spectrum of Figure 6.2) exhibits a spectral line around 5 cm^{-1} due to extentional vibration modes of the NCls. This line shifts down with increasing nanocolumn length as shown in Reference [29]. Moreover, a band around 38 ± 2 cm^{-1}, identified as a breathing-like mode of the nanocolumns, can also be observed in the FT spectrum (cf. sketch on the top of

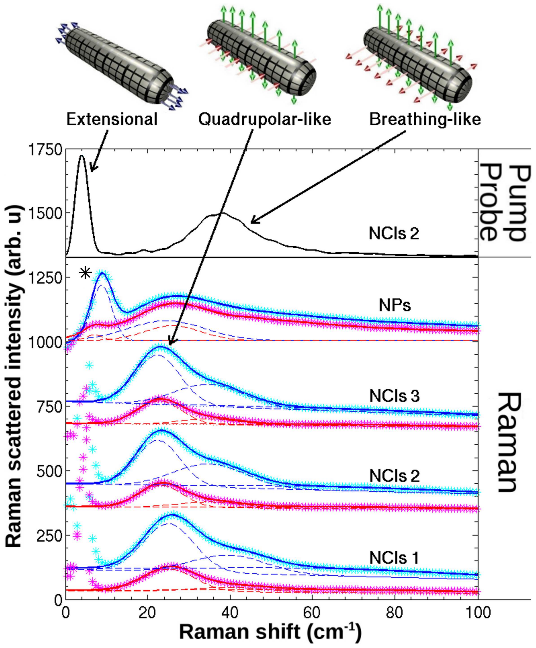

Figure 6.2: From bottom to top: Resonant Raman-Brillouin spectra (stars) of samples NCls1, NCls2 and NCls3 and of isolated nanoparticles (NPs) for P-polarized (blue) and S-polarized (red) incident light. The corresponding fits (full lines) have been obtained using two Gaussian line-shapes and a background (dashed lines). Upper spectrum is the Fourier transform of the oscillating component of the time resolved transient absorption from sample NCls2. Field displacement vectors of the vibrations are shown with the sketches in the upper part of the figure. The peak marked by a black star in the spectra corresponding to the sample containing isolated nanoparticles corresponds to the Brillouin peak of the Si substrate. Raman-Brillouin spectra recorded by Adnen Mlayah at the University of Toulouse.

Figure 6.2).

In the Raman-Brillouin spectra, remarkably, an additional band is visible on the high frequency tail of the quadrupolar-like mode for the three nanocolumn samples (NCls1, NCls2, NCls3). This band is mainly observed for P-polarization (blue line) and almost vanishes for S-polarization (red line). The observation of this “anomalous” band in the Raman-Brillouin spectra is a striking finding. By fitting the Raman-Brillouin spectra with Gaussian line shapes it is possible to extract the frequencies, bandwidths and relative intensities of the observed bands.

The Raman-Brillouin bandwidth is due to both homogeneous and inhomogeneous broadening of the vibration modes. The homogeneous broadening is due to the presence of a matrix and increases with decreasing NP size [46]. From these time resolved pump-probe experiments (Figure 6.2), the homogeneous broadening of the breathing-like mode is estimated around Γ_{hom} =16 cm^{-1}. On the other hand, the contribution of the NCls width distribution (0.4 nm) to the inhomogeneous broadening is estimated around Γ_{inhom} =4 cm^{-1}. The homogeneous broadening and the inhomogeneous broadening due to the lateral size distribution of the NCls solely cannot fully explain the observed Raman-Brillouin bandwidth which is around 20 cm^{-1}. From the TEM (Figure 6.1a) it can be noticed that the NCls may strongly differ in shape (misalignment of the NPs) and can be described by a stacking of 3-5 NPs. This shape distortion is responsible for an additional inhomogeneous broadening which gives the strongest contribution to the Raman-Brillouin bandwidths. This is the reason why Gaussian functions are used, rather than Lorentzian, for the fitting of the Raman-Brillouin spectra.

The frequency of the “anomalous” band is dispersed from 39 cm^{-1} (NCls1) to 36 cm^{-1} (NCls2) and 35 ± 2 cm^{-1} (NCls3) quasi-independently on the NCl length, similarly to the behaviour of the quadrupolar-like mode. Interestingly, the frequency of the anomalous band is very close to that of the breathing-like vibration band observed in the FT spectrum of the transient absorption (cf. Figure 6.2). Therefore, it seems natural to associate the additional band observed in the NCls Raman-Brillouin spectra to scattering by their breathing-like acoustic vibrations.

However, according to the SO coupling mechanism (cf. Section 6.1.2), which has been shown to be the most important mechanism for the Raman-Brillouin scattering in metallic nano-objects, breathing-like vibrations are not expected to have a strong Raman-Brillouin activity. Indeed, this coupling mechanism involves the modulation of the localized surface plasmon polarization field by shape deformation of the nano-object (modulation of the surface polarization charges by the acoustic vibrations). Therefore, because breathing-like vibrations produce mainly a volume change and not a shape deformation they are hardly observed by Raman-Brillouin scattering. Nevertheless, the associated volume change gives rise to deformation potential interaction with the surface plasmons. For silver nano-objects this Raman-Brillouin scattering mechanism is about one order of magnitude less efficient than the surface orientation mechanism [16; 17]. As a matter of fact, quadrupolar-like vibration modes dominate the Raman-Brillouin spectra (Figure 6.2) owing to the strong shape deformation they produce, thus leading to efficient modulation of the surface plasmon polarization [16; 17].

To further investigate the activation of the “anomalous” band, it is interesting to trace the dependence of the Raman-Brillouin spectra on polarization of the excitation light. Figure 6.3 shows the vanishing of this band when continuously changing the polarization from P to S. Figure 6.3b gives the variation of the integrated intensity of the “anomalous” band normalized to that of the quadrupolar-like vibration band. A clear cosine-like intensity evolution is observed.

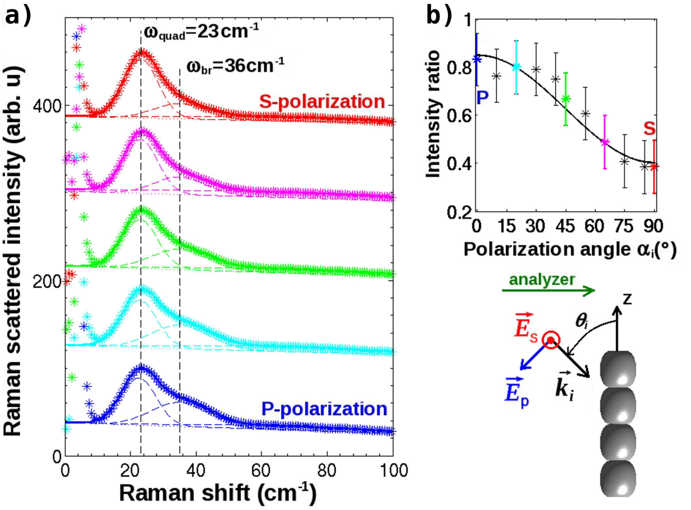

Figure 6.3: (a) Resonant Raman-Brillouin spectra (stars) from sample NCls2 and the corresponding fits (full lines) obtained with Gaussian line shapes (dashed lines), for five polarization angles from P (blue) to S (red) configurations. (b) Integrated intensity of the band at 36 cm^{-1} normalized to that of the quadrupolar-like mode as a function of the polarization angle α_i (points) defined by $\vec{E}_i = \vec{E}_P \cos\alpha_i + \vec{E}_S \sin\alpha_i$. The green arrow indicates the direction onto which the scattered light is analyzed. The line is a fit to the experimental data obtained with $0.46\cos^2\alpha_i + 0.4$.

For S-polarized incident light the electric field is perpendicular to that of the scattered and analyzed light. In this crossed configuration, only acoustic vibrations projecting the polarization vector onto the perpendicular direction (because of shape deformation) are observable. This is the case of the quadrupolar-like vibrations, which are indeed observed in both crossed and parallel configurations (Figure 6.2). On the other hand, breathing-like vibrations do not present such a projection since they do not produce shape deformation of the vibrating object. As a consequence, Raman-Brillouin scattering by breathing-like modes, if activated, would occur only in the parallel configuration. This is precisely the tendency observed in Figures 6.2 and 6.3 for the “anomalous” band (significant intensity decreases in the crossed configuration). In comparison, the line shape of the Raman-Brillouin spectra recorded from isolated nanoparticles in both crossed and parallel configurations are identical (NPs in Figure 6.2) thus indicating the absence of any contribution from breathing vibrations. The scattering in this case is dominated by the well known quadrupolar acoustic vibration modes allowed in both configurations [51]. All the above strongly support the assignment of the "anomalous" band to breathing-like acoustic vibrations of the NCls.

To address the reason why the breathing-like acoustic vibrations of the NCls efficiently scatter the light inelastically, I performed dynamical simulations of the surface plasmons near-field for these particular vibration modes. The acoustic vibration eigenmodes have been calculated in order to use their associated displacement fields as geometrical boundary inputs for the calculation of the localized surface plasmons eigenstates. The modulation of the LSP electromagnetic near-field generated in that way determines the Raman-Brillouin activity of the vibration modes.

6.2.3 Modeling of the nanocolumn vibrational properties

Two different shapes of the NCls have been modeled: (i) smooth cylindrical nanocolumns and (ii) nanocolumns with indentations. The indented nanocolumn resembles the shape of the actual NCls, as shown in Figure 6.1a due to the growth process (self-alignment of spherical NPs). Of course the exact shape may fluctuate and the indentations may be more or less pronounced depending on the NCls. Nevertheless, the theoretical results presented in this section and the interpretation of the experimental data do not depend critically on the exact NCls shape.

The acoustic vibrations of the NCls have been calculated by Lucien Saviot at the Laboratoire Interdisciplinaire Carnot de Bourgogne, in the University of Bourgogne. The calculations assume an elastic continuous medium (cf. Section 4.1) [35; 36; 39; 154] and use the Resonant Ultrasound Spectroscopy (RUS) method proposed by Visscher *et al.* [186]. Because of the polycrystalline nature of the NCls, the mechanical properties of silver were approximated by isotropic elastic constants [116]. For the sake of simplicity, in order to obtain discretized vibrational modes, the nanocolumns are considered to be in vacuum. The calculations provide both the eigenfrequencies and the eigenvectors of the vibrations. The irreducible representations as well as the volume variation, associated to each vibration mode can be determined in this way [163], thus providing a straightforward way to identify the modes. In Figure 6.4 are shown the surface displacement fields of the indented nanocolumn for four relevant acoustic vibration modes: (a) extensional mode (A_{1g} symmetry), (b) quadrupolar-like mode (E_{2g} symmetry), (c, d) two breathing-like modes (A_{1g} symmetry).

The vibration frequencies calculated for the extensional (a) and quadrupolar-like (b)

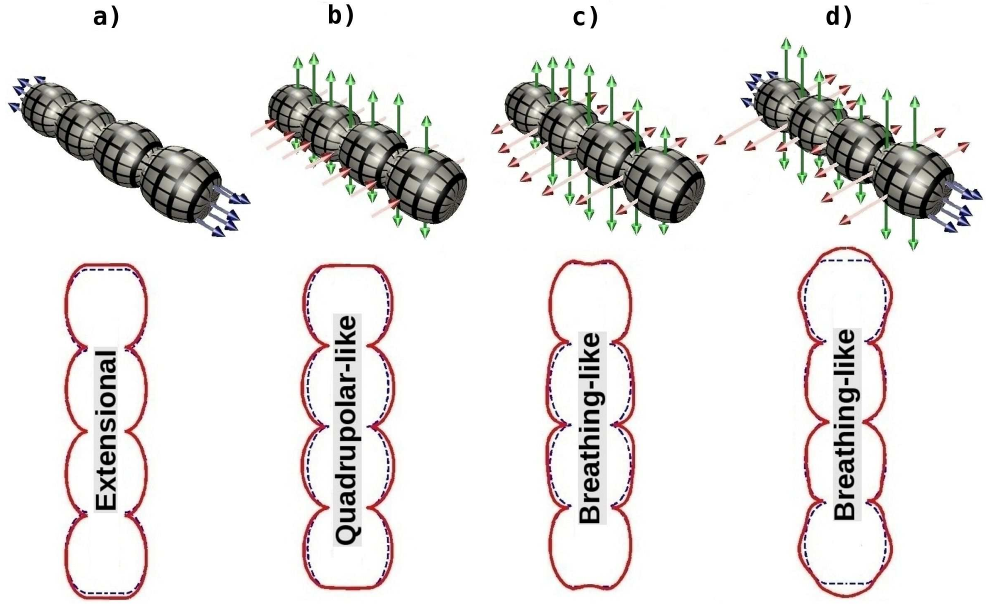

Figure 6.4: Relevant acoustic vibration modes of the indented nanocolumns. The arrows show the displacement eigenvectors at the surface of the model nanocolumn vibrating in its (a) extensional, (b) quadrupolar-like, (c, d) breathing-like eigenmodes. Cross section along the NCl main axis shows the deformed surface (red line) and the surface of the NCl at equilibrium (blue dashed line).

modes are respectively 4 cm^{-1} and 16 cm^{-1} (cf. Table 6.1) in good agreement with the band frequencies observed in time resolved FT (5 cm^{-1}) and Raman-Brillouin spectra (23 ± 2 cm^{-1}). The two breathing-like modes (Figures 6.4c and 6.4d) are radial modes mainly (A_{1g} symmetry); they give rise to the largest volume variation. The fact that two breathing-like modes are obtained, and not a single mode as for an isolated spherical particle, can be understood in terms of mixing between the spheroidal vibration modes of a spherical particle when the shape evolves from a sphere to a column [36]. The two breathing-like modes (Figures 6.4c and 6.4d) are quasi-degenerated: 34 cm^{-1} for mode (c) and 36 cm^{-1} for mode (d). Their average frequency is in excellent agreement with the frequency of the breathing-like vibration observed in the FT spectrum of the time-resolved transient absorption oscillations (Figure 6.2). More interestingly the agreement with the frequency of the "anomalous" Raman-Brillouin band is remarkable. This provides additional support for the assignment of the "anomalous" Raman-Brillouin band to scattering by breathing-like acoustic vibrations.

Table 6.1: Calculated ω_{calc} and measured ω_{exp} vibration frequencies of the extensional (a), quadrupolar-like (b) and breathing-like (c, d) acoustic vibration modes of the indented nanocolumns where a-d refer to the vibration mode shown in Figure 6.4. The technique used to extract the experimental values is indicated in the table.

Acoustic vibration mode	ω_{exp} (cm^{-1})		ω_{calc} (cm^{-1})	
Extensional	5	(Pump-Probe)	4	(a)
Quadrupolar-like	23	(Raman-Brillouin)	16	(b)
Breathing-like	36	(Raman-Brillouin)	34	(c)
	38	(Pump-Probe)	36	(b)

6.2.4 Modeling of nanocolumn plasmonic properties

The optical response and the acousto-plasmonic dynamics of the nanocolumns are now calculated using the BEM. Maxwell's equations are numerically solved for the experimental excitation conditions and for both static nanocolumns and for nanocolumns deformed by the acoustic vibrations. The calculated extinction spectra are shown in Figure 6.1b. The transverse LSPR is well reproduced by the simulations. However, a small shift (around 15 nm) between the calculated and the measured resonances can be noticed. This shift is due to interactions between the transverse LSP of the NCls that are not taken into account in these simulations [117]. This small blue-shift has been described by a simple theoretical model by J. Krenn and co-workers ??.

Because the acousto-plasmonic interaction depends on the modulation of the polarization associated to a particular vibration mode, the evolution of the near-field distribution for the relevant breathing-like modes has been calculated. All the simulations are performed at the experimental excitation wavelength, polarization (both P and S) and angle of incidence. Snapshots of the NCls at equilibrium and at maximum deformation are provided in Figure 6.5. In terms of interaction steps, this is equivalent to map the first two steps in the resonant Raman-Brillouin process described by Equation 6.1: optical excitation of the localized surface plasmon (first intermediate state) and subsequent interaction with the acoustic vibration mode given by Equation 6.2.

When these nano-objects are described as smooth cylindrical NCls, i.e. without indentations (left panels in Figure 6.5), the modulation of the surface plasmon near-field by the breathing-like vibrations is very weak both for P- and S-polarized light (cf. Figures 6.5a and 6.5b, respectively). In contrast, for the indented NCls, the surface plasmon near-field is strongly modulated by the breathing-like vibration modes (right panels in Figure 6.5). Modulation occurs for both P- and S-polarizations. The strong surface plasmon modulation is due to (i) the near-field intensity accumulation in the regions of indentations, and

a) P-polarization

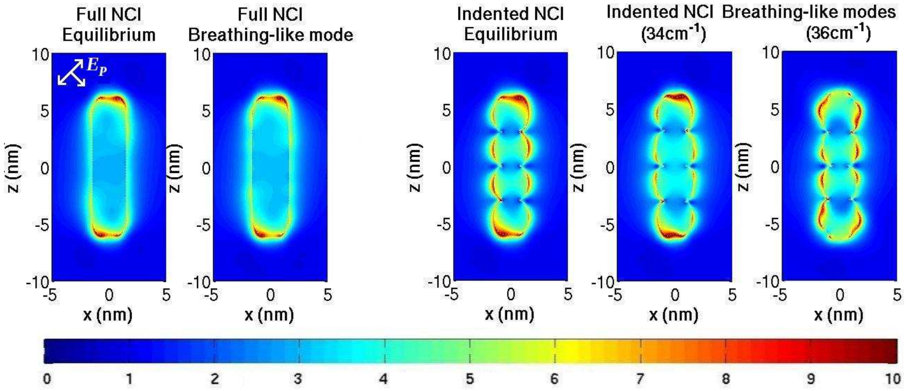

b) S-polarization

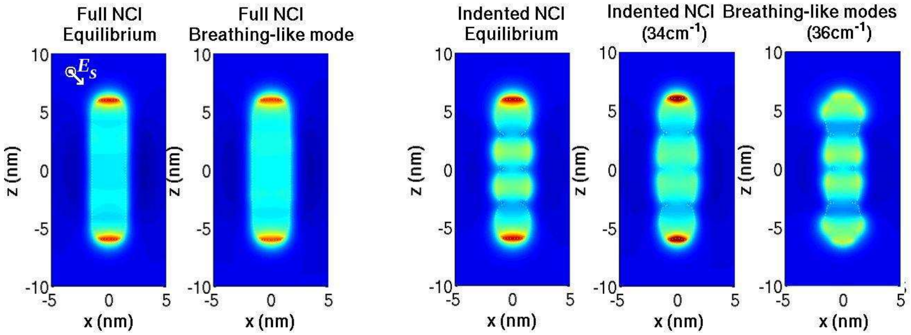

Figure 6.5: Local electric field distribution around the smooth cylindrical and indented nanocolumns calculated for the experimental configuration at $\lambda_i = 413$ nm, $\theta_i = 34.5°$, and for both P- and S-polarizations (resp. a and b). The color scale corresponds to the local field enhancement factor $|\vec{E}(\vec{r})|/|\vec{E}_i(\vec{r})|$.

to (ii) the strong local shape deformation by the acoustic displacement also mediated by the presence of indentations (cf. Figure 6.4). Following the dependence of the acoustic vibration-surface plasmon coupling strength from Equation 6.2, both effects (i and ii) enhance the modulation of the surface plasmon polarization $\delta_{vib}\vec{P}_a$ and effectively activate the Raman-Brillouin scattering by the breathing-like vibration modes.

6.2.5 Acousto-plasmonics and polarization modulation

In order to gain more insight in the understanding of the role of the NCIs shape I finally present a quantitative analysis of the acousto-plasmonic coupling. Figure 6.6 shows the spatial distribution of the relative modulations $\frac{\delta_{vib}|\vec{P}|}{|\vec{P}_0|}$ of the surface plasmon polarization by the breathing-like modes (cf. Figure 6.4) for both smooth and indented NCls; $\vec{P}_0$ and $\delta_{vib}|\vec{P}|$ (cf. Equation 6.2) are respectively the surface plasmon polarization and the modulation of its amplitude both calculated at a fixed distance of 0.5 nm from the surface of the NCls at equilibrium. The modulation of the surface plasmon polarization is once again much larger for the indented NCls than for the smooth cylindrical NCls, particularly around the regions of indentations. The spikes in $\frac{\delta_{vib}|\vec{P}|}{|\vec{P}_0|}$ arising from the strong shape deformation at the indentations can be considered as the hot-spots of the acousto-plasmonic interaction. For P-polarized light (left panels in Figure 6.6), the relative modulation $\frac{\delta_{vib}|\vec{P}|}{|\vec{P}_0|}$ ranges from -9 to 4 for the breathing-like mode at 34 cm^{-1}, and from -9 to 6 for the mode at 36 cm^{-1}, depending on the considered point. For the smooth NCls, the minimum and the maximum of $\frac{\delta_{vib}|\vec{P}|}{|\vec{P}_0|}$ are -4 and 2, respectively, and are visible only around the NCls end regions, whereas along the NCl walls $\frac{\delta_{vib}|\vec{P}|}{|\vec{P}_0|}$ presents a very small value not exceeding -0.05. Similarly, with S-polarized light (right panels in Figure 6.6), the relative modulation $\frac{\delta_{vib}|\vec{P}|}{|\vec{P}_0|}$ ranges from -9 to 9 for both breathing-like modes of the indented NCls and is larger than that calculated for the smooth NCls. As can be noticed in Figures 6.5 and 6.6, the modulation of the localized surface plasmons occurs for both P- and S-polarized incident light whereas the Raman-Brillouin scattering by breathing-like vibrations appears mainly for P-polarization (Figures 6.3 and 6.4). The reason lies in the fact that the Raman-Brillouin process does not consist only of the optical excitation of the localized surface plasmons and their modulation by the acoustic vibrations but also of the emission of the scattered photon (outgoing photon term in Equation 6.1). Indeed, the extinction of the Raman-Brillouin scattering for S-polarization is due to the fact that the scattered light is analyzed in the orthogonal direction (crossed configuration). In other words, even though the surface plasmons are efficiently excited with S-polarized incident light and strongly modulated by the breathing-like vibrations, the corresponding $\delta_{vib}\vec{P}_a$ (Equation 6.2) has no component on the direction perpendicular to $\vec{P}_a$ because of the shape conserving deformation.

The modulation of the optically induced polarization gives the strength of the acousto-plasmon coupling. Indeed, the acousto-plasmonic hot-spots (spikes visible in Figure 6.6 for the indented NCls) give rise to non-vanishing interaction matrix elements (Equation 6.2), thus leading to the activation of breathing-like vibration modes which are otherwise inefficient Raman-Brillouin scatterers. In fact, considering wall region of the indented NCls, the relative surface plasmons modulation is roughly in the range 10 times (between spikes) to 200 times (at the spikes) larger than that of the smooth NCls, depending on the considered point.

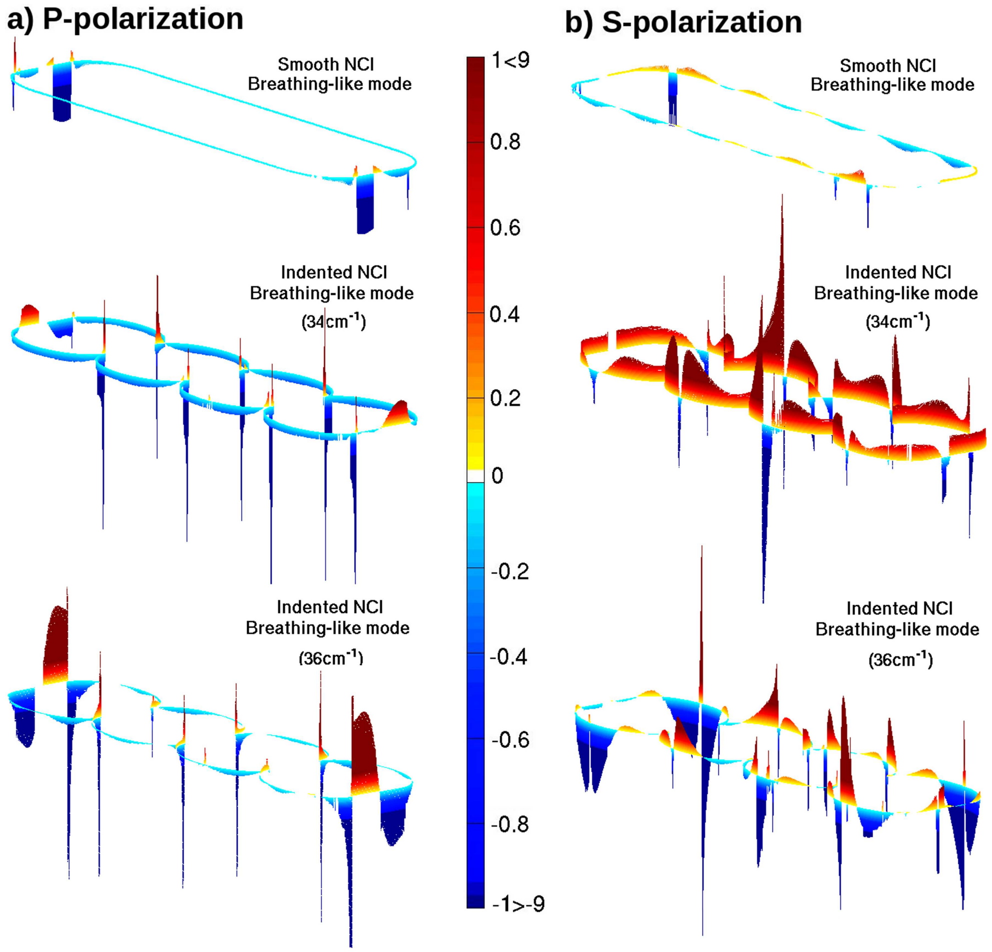

Figure 6.6: Relative modulation of the amplitude of the induced polarization by the breathing-like modes at a fixed distance of 0.5 nm from the surface of the NCls at equilibrium: $\delta_{vib}|\vec{P}|/|\vec{P}_0|$. The modulation, shown here for the smooth and indented nanocolumns, were calculated for the experimental configuration at $\lambda_i = 413$ nm, $\theta_i = 34.5°$, and for both P- and S-polarizations (resp. a and b). The color scale saturates at -1 and 1 even though the minimum and the maximum values are -9 and 9 respectively.

6.3 Acousto-plasmonic dynamics in gold dimers

Another interesting nanostructure which provides excellent properties for plasmonic-based nanophotonics is the system of two metallic nanoparticles or dimers. Raman-Brillouin scattering by acoustic vibrations in small metallic nanoparticles has been studied experimentally [58]. In particular, the plasmonic properties of dimers [59; 102; 137; 157], trimers [26; 107; 178; 181], or quadrumers [26] of metallic nano-objects have already been investigated intensively. Nevertheless, the acousto-plasmonic properties of these systems are still a challenge to be fully understood. Dimers of nanoparticles can be considered as a building block of more complex nanostructures (e.g. clusters of nanoparticles). An important feature of these interacting nano-objects is that they exhibit gaps where plasmonic hot-spots can be localized. These hot-spots are very useful properties in field-enhanced spectroscopies [4; 178; 181]. Furthermore, these gaps can be easily controlled changing the interparticle distance and nano-particle sizes thus leading to controlable properties of the hot-spots.

6.3.1 Far-field properties

In Section 6.2, the concept of acousto-plasmonics has been introduced in the case of an isolated nano-object exhibiting plasmonic hot-spots due to shape effects. Here this approach is extended to the case of interacting nano-objects and more specifically to dimers of gold nanoparticles. This nano-object is of interest since it can be viewed as a building block for more complex nanostructures such as clusters of nanoparticles. Several parameters can affect the plasmonic properties of dimers: (i) the material of the two nanoparticles, that can be different, (ii) the radii of the nanoparticles, that can be also different, (iii) the inter-particle distance, and (iv) the surrounding medium. In order to investigate the effect of these parameters, the extinction cross section has been calculated for different cases. The results are shown in Figure 6.7. First, it can be noticed that the LSPR of the dimers red-shifts when they are embedded in a matrix. Second, the spectral separation between the longitudinal and transverse excitations (i.e. Transverse/Longitudinal splitting) increases when the inter-particle distance decreases (from 10 nm-17 nm in vacuum to 28 nm-69 nm in Al_2O_3). This effect is due to the screening of the interaction by the polarizability of the surrounding medium [157].

These effects underline how the LSPR can be very sensitive, leading to a high tunability and control of the optical properties of the system.

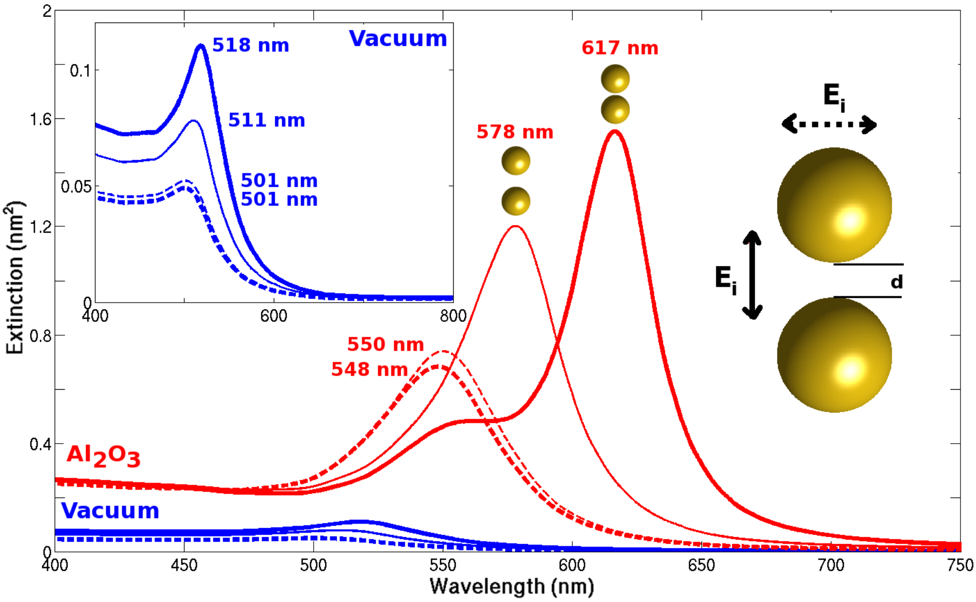

Figure 6.7: Extinction spectra of gold dimers in vacuum (blue spectra) and in Al_2O_3 (red spectra) both in the transverse (dashed lines) and longitudinal (full line) excitation configurations. The spectra have been calculated for two separation distances d =0.7 nm and 2.1 nm (sketches are shown close to the corresponding spectra). The inset shows a zoom-in of the spectra of the dimer in vacuum. The incident light polarizations are shown in the inset.

6.3.2 Controllable acousto-plasmonic hot-spots

Plasmonic hot-spots are generated in the gap between the nanoparticles [102; 137; 157], similarly to the coupled nano-antenna in Section 5.1. Figure 6.8 shows the electric field distribution (Figure 6.8a) and the induced polarization (Figure 6.8b) for (i) both nanoparticles at rest (left panels), (ii) upper nanoparticle vibrating in the $l = 0$ mode, i.e. breathing mode, (center panels), and (iii) upper nanoparticle vibrating in the $l = 2, m = 0$ mode, i.e. quadrupolar mode, (right panels).

a) Electric Field - 578 nm

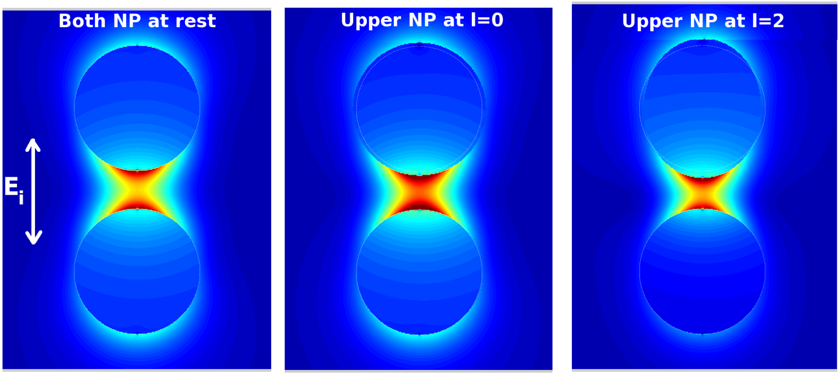

b) Polarization - 578 nm

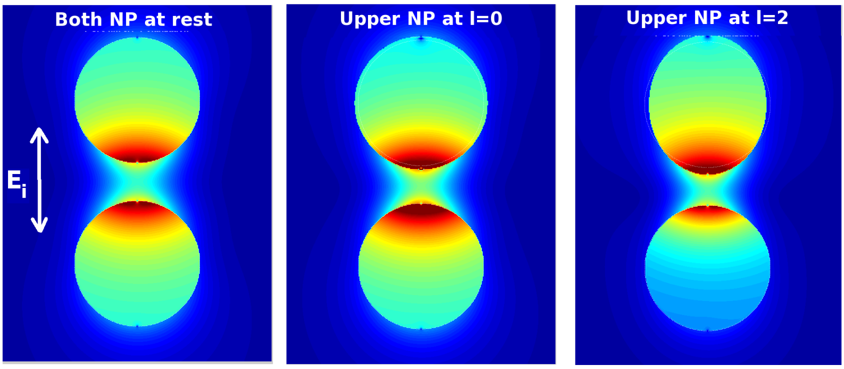

Figure 6.8: (a) Electric field distribution and (b) Polarization of a gold dimer embedded in Al_2O_3, where both particles are at rest (left panels), the upper nanoparticle is vibrating in $l = 0$ mode (center panels), and the upper nanoparticle is vibrating in $l = 2, m = 0$ mode (right panels). The excitation wavelength is 578 nm.

As it can be seen from the electric field distribution, the plasmonic hot-spot, localized in the gap, is efficiently modulated by the acoustic vibration. Both a change in amplitude and in spatial distribution of the electric field can be noticed from Figure 6.8a by comparing the near-field distributions of the particle deformed (center and right panels) with that of the particle at rest (left panel). The breathing $l = 0$ mode has a spherical symmetry and is thus forbidden in Raman-Brillouin scattering of isolated nano-particle [15; 51], whereas it is allowed in dimers of nanoparticles, where the spherical symmetry is broken. An acousto-plasmonic hot-spot is generated similarly to the breathing-like mode with the indentations of the NCls that was discussed in Section 6.2.4. Quadrupolar $l = 2, m = 0$ mode, which breaks the spherical symmetry of an isolated nanoparticle, is also responsible for the generation of an acousto-plasmonic hot-spot in the dimer.

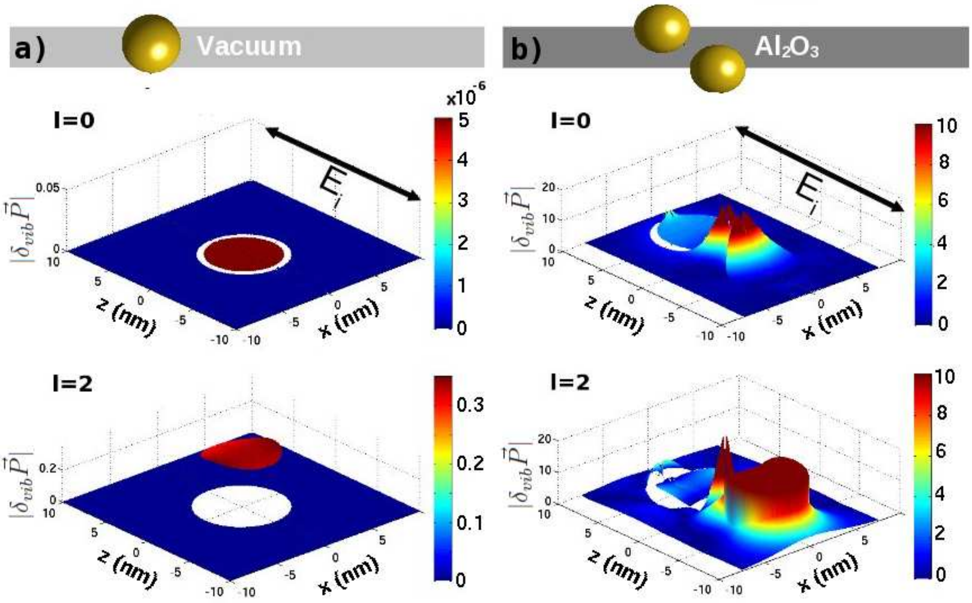

Figure 6.9: Modulus of the modulation of the induced polarization $|\delta_{vib}\vec{P}(\vec{r})|$ for (a) isolated nanoparticle in vacuum and (b) dimer in Al_2O_3 for both $l = 0$ (upper panels) and $l = 2, m = 0$ (lower panels) vibration modes.

Figure 6.9 shows the modulus of the modulation of the polarization $|\delta_{vib}\vec{P}(\vec{r})|$ for (a) isolated nanoparticle in vacuum and (b) dimer in Al_2O_3. In the case of an isolated nanoparticle in vacuum, vibrating in either $l = 0$ or $l = 2$ mode, the modulation of the polarization is negligible and limited to the nanoparticle volume (cf. Figure 6.9a). This small contribution to the Raman-Brillouin scattering intensity (cf. Equation 6.1) is then negligible. For interacting nanoparticles, the acousto-plasmonic hot-spots can be clearly seen in the gap (cf. Figure 6.9b). The penetration of the polarization, and its modulation, in the gap occur because of the presence of the surrounding matrix. The presence of the surrounding matrix as well as the strong interaction between the nanoparticles strongly enhance the amplitude of the polarization modulation. Indeed, for $l = 2$ vibration mode, the dimer exhibits a modulation of about 100 times larger than the modulation generated in the isolated nanoparticle in vacuum (cf. lower panels in Figure 6.9). This effect is much more pronounced for the $l = 0$ vibration mode where the modulation is increased by a factor of 4×10^6 (cf. upper panels in Figure 6.9). Moreover, it has to be noticed that the polarization in the particle at rest (lower nanoparticle) is efficiently modulated by the quadrupolar mode of the upper nanoparticle (cf. lower panel of Figure 6.9b). This strong acousto-plasmonic effect, which is of the same order of magnitude as the acousto-plasmonic hot-spot, is of fundamental interest for the study of vibrational transfer between interacting nano-objects.

The acoustic vibration modes do not only modulate the amplitude of the polarization but also efficiently modulate its direction. The changes in the direction of the polarization field are shown in Figure 6.10 for both breathing (a) and quadrupolar (b) vibration modes. Snapshots of the near-field distribution for the minimum ($\vec{r}-\delta\vec{u}$, left panels) and maximum ($\vec{r}+\delta\vec{u}$, right panels) deformation of the nanoparticle are shown for both acoustic vibration modes. An area where the modulation of the direction of the polarization vector is clearly visible is marked with a white circle in Figure 6.10. These direction changes also contribute to the Raman-Brillouin scattering through the surface orientation coupling mechanism (Equation 6.2).

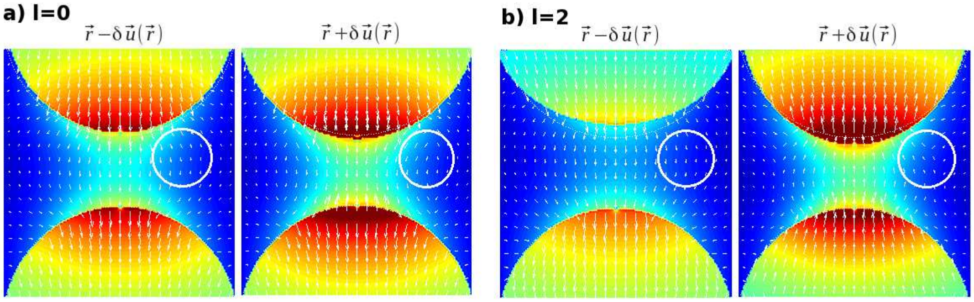

Figure 6.10: Polarization maps of a gold dimer embedded in Al_2O_3, deformed by (a) $l = 0$ vibration mode and (b) $l = 2, m = 0$ vibration mode. For each acoustic vibration, the polarization is shown for the maximum and the minimum deformation.

Similarly to the nanocolumns, these controllable acousto-plasmonic hot-spots, via Equations 6.2 and 6.1, are directly related to the Raman-Brillouin scattering intensity. Modulation of these hot-spots opens new perspectives in the interpretation of Raman-Brillouin measurements in more complex nano-objects and nanostructures. Moreover, fine physical effects have been pointed out toward the control of acousto-optical properties of such metallic nano-objects and shine the light on possible vibrational transfer between interacting nano-objects, mediated by the acousto-plasmonic dynamics.

Summary Part II

In Chapter 5, I have shown that tailoring the optical properties of plasmonic nanostructures requires a complete understanding of the physical parameters that may influence the LSPR (e.g. shape, size, materials).

In a first part, I have investigated a new class of nanoscale optical switches consisting of a plasmonic nano-antenna loaded with a photoconductive semiconductor material. By short circuiting the antenna gap using a semiconductor free-carrier plasma, I have shown that the mode spectrum of the antenna shifts dramatically using only a very modest pumping energy. The nano-antenna switch can be used to control both far-field and near-field properties. In addition, I have identified a regime of partially conductive gap where a new plasmon mode is formed, which combines a narrow spectral profile with a large local-field enhancement in the antenna gap. The nano-antenna switch combines large modulation depth, low switching threshold, and potentially ultrafast time response. Although the switching threshold is relatively high compared to terahertz photoconductive devices, it is expected that these carrier densities can be achieved using ultrafast optical pumping. As the switching mechanism is universal to any photoconductive medium, other semiconductors or semimetals such as InP and ITO can be explored. Further optimization may be possible by considering antenna designs different from the coupled-dipole configuration. Nano-antenna switches open up new avenues to applications ranging from integrated photonics, ultrafast lasers, to quantum information devices.

Plasmonic nano-resonators are generally designed from numerical simulations of ideal nano-objects with the aim of targeting specific applications. In a second part of this work it has been shown that in a ring-disk, the ring-like LSPR wavelength is determined not only by the disk and ring diameters but also by the fine shape deformation of the ring walls and edges caused by the lithography and lift-off processes. It has been found that a rounded shape of the ring surfaces and edges is responsible for significant red-shifts of the ring-like LSPR that can be as large as 469 nm with respect to the perfect ring-disk with vertical side walls, flat surfaces and sharp edges. Moreover, based on numerical simulations and on a quantitative analysis of the shape effect it has been possible to extract, from the measured optical spectra, average ring-disk shapes. Good agreement was found with the AFM profiles. This work has shown that the actual shape of plasmonic nanoresonators that exhibit small imperfections can strongly impacts their LSPR properties. It sheds light on the importance of taking into account the fine shape details of nanostructures exhibiting corners, edges and wedges (e.g. bowtie antennas, nanorods, nanostars) and of systems involving strong electromagnetic interactions (e.g. sharp tip interacting with an object, coupled nano-antennas). This effect is also of importance for the accurate design of plasmonic structures for optical signal processing and control.

These physical parameters are thus important for the understanding of the plasmonic properties, as it has been shown previously, but also for the acousto-plasmonic properties and the understanding of inelastic light scattering properties such as Raman-Brillouin scattering. Indeed, based on the concept of acousto-plasmonic hot-spots, I provided a conceptual understanding of the fundamental mechanism leading to the activation of normally very weak modes in the Raman-Brillouin scattering of nano-objects (Chapter 6). I have shown that, for the surface orientation mechanism, the breathing-like vibrations which are almost silent for smooth cylindrical nanocolumns are strongly enhanced in the case of indented nanocolumns. The indentations of the silver nanocolumns are responsible for the strong localization of the surface plasmon near-field and its modulation by breathing-like acoustic vibrations. Understanding the acousto-plasmonic dynamics of metallic nano-objects is useful not only for the interpretation of Raman-Brillouin and time-resolved pump-probe experiments but also for nanometrology, i.e. extracting information on size and shape distributions from these optical measurements. The concepts, the numerical and experimental approaches have been extended to interacting nano-objects exhibiting strong field localization (i.e. dimers of nano-objects). It has been shown that due to the gap between the two nano-objects, a strong field localization (hot-spot) modulated by the acoustic vibration gives rise to a controllable acousto-plasmonics hot-spot responsible for the activation of Raman band normally forbidden in isolated nano-objects. These activations are induced due to breaking of the vibrational symmetries in the system, leading to the breaking of the Raman-Brillouin selection rules. This concept of acousto-plasmonic hot-spot is the fundamental basis of the vibrational transfer between interacting nano-objects. The concepts developed in this work can thus be extend to more complex interacting systems such as clusters of nanoparticles since the dimer can be seen as a building block of such system.

Epilogue

This work focused on the interactions between low frequency acoustic vibrations and electronic excitations, i.e. confined electronic states in semiconductors and localized surface plasmons in metals, involved in resonant Raman-Brillouin scattering. The use of advanced numerical methods has allowed to develop new theoretical tools and physical concepts that help to deeply understand and interpret Raman-Brillouin scattering measurements on semiconductor and metallic nanostructures: (i) Raman-Brillouin Electronic Density, and (ii) Acousto-plasmonic hot-spots.

A direct and a rather simple way to fully understand Raman-Brillouin scattering in semiconductors, taking into account resonance effects and size dependence of the spectra, even though a large number of electronic states are involved in the light scattering, is the Raman-Brillouin Electronic Density (RBED). The RBED is also a tool to investigate the validity of the step-like profile of the photoelastic coefficient usually assumed in the photoelastic model. Indeed, I have shown that both in the case of membranes and superlattices the use of the RBED allowed to clearly understand the activation and deactivation of Raman-Brillouin acoustic modes. Comparison between the profiles of the photoelastic coefficients and of the RBED were presented and discussed in the case of thin films and superlattices. In particular, because the photoelastic coefficient is constant within each quantum well the electron-vibration interaction may be overestimated or underestimated depending on the considered excitation energy. The RBED is very useful when numerous electronic transitions may be resonantly and simultaneously excited.

In metallic nanostructures, the electronic excitations involved in the Raman-Brillouin scattering process are the surface plasmons. The understanding of the coupling mechanisms are of importance to fully determine the origin of the ineslastic light scattering in complex metallic nanostructures. To investigate that, I first focused on the understanding of plasmonic properties of metallic nanostructures, i.e. gold nanoring-disks and optical nano-antennas. A new class of optical nanoswitchers consisting of a plasmonic nano-antenna loaded with a photoconductive semiconductor material has been introduced. The nano-antenna optical response is dramatically shifted by short-circuiting the nano-antenna with the free-carriers of the photoconductive material gap. This photoconductive switcher can be used to control both far-field and near-field properties. Furthermore, shape and size effects on plasmonic nano-resonators (i.e. nanoring-disks) have been investigated. I have found that a rounded shape of the ring surfaces and edges is responsible for significant red-shifts of the ring-like LSPR that can be very large with respect to the ideal ring-disk exhibiting vertical side walls, flat surfaces and sharp edges. Good agreement was found with the AFM and optical measurements. Shape effects are also important for the understanding of Raman-Brillouin scattering properties. Indeed, I introduced the concept of acousto-plasmonic hot-spots in metallic nanostructures. Well known plasmonics hot-spots, modulated by low frequency acoustic vibrations, are responsible for the activation of Raman-Brillouin acoustic modes in the scattering process of metallic nano-objects. The presence of defects (e.g. indentations in silver nanocolumns) or systems with interacting nanoparticles (e.g. gold dimers) held such acousto-plasmonic hot-spots.

I have shown that, for the surface orientation mechanism, the breathing-like vibrations which are almost silent for smooth cylindrical nanocolumns are strongly enhanced in the case of indented nanocolumns. The indentations of the silver nanocolumns are responsible for the strong localization of the surface plasmon near-field and its modulation by breathing-like acoustic vibrations. Understanding the acousto-plasmonic dynamics of metallic nano-objects is useful not only for the interpretation of Raman-Brillouin and time-resolved pump-probe experiments but also for nanometrology, i.e. extracting information on size and shape distributions from these optical measurements. The concepts, the numerical and experimental approaches have been extended to other isolated nano-objects exhibiting strong field localization (dimers of nano-objects). It has been shown that in the gap between the interacting nanoparticles, a strong field modulation by the acoustic vibrations takes place. This modulation of controllable hot-spots may give rise to Raman-Brillouin scattering by acoustic vibration modes that are normally forbidden in isolated nanoparticles. The concept of acousto-plasmonic hot-spots opens up the way for the vibrational transfer between interacting metallic nano-objects and can be extended to clusters of nanoparticles or other interacting nanostructures.

Appendix A

Fundamental Physical Constants

Table A.1: Fundamental physical constants taken from 2010 CODATA recommended values.

Quantity	Symbol	Value	Unit	Rel. std uncert.
speed of light in vacuum	c	299792458	$\mathrm{m.s}^{-1}$	exact
magnetic constant	μ_0	$4\pi \times 10^{-7}$	$\mathrm{N.A}^{-2}$	exact
electric constant $1/\mu_0 c^2$	ε_0	$8.854187817...\times10^{-12}$	$\mathrm{F.m}^{-1}$	exact
Planck constant	h	$6.62606957(29)\times10^{-34}$	J.s	4.4×10^{-8}
reduced Planck constant	$\hbar = h/2\pi$	$1.054571726(47)\times10^{-34}$	J.s	4.4×10^{-8}
elementary charge	e	$1.602176565(35)\times10^{-19}$	C	2.2×10^{-8}
Bohr radius	a_0	$0.52917721092(17)\times10^{-10}$	m	3.2×10^{-10}
electron mass	m_e	$9.10938291(40)\times10^{-31}$	kg	4.4×10^{-8}
Boltzmann constant	k_B	$1.3806488(13)\times10^{-23}$	$\mathrm{J.K}^{-1}$	9.1×10^{-7}

Appendix B

Numerical Methods to Solve Maxwell's Equations

Analytical exact solutions to Maxwell's equations (cf. Equations 4.4a) can be obtained only in simple cases such as spheres. The theoretical study of plasmonic properties of metallic nano-objects can be challenging when the shape of these nano-objects departs from this canonical shape. To do so, numerical methods are required to solve Maxwell's equations. The Boundary Element Method (BEM) was used to obtain the numerical results presented in this manuscript. I briefly introduced here the principle of this method. In order to emphasize the specificities of the BEM, two extensively used numerical methods are briefly presented in this appendix: Discrete Dipole Approximation, and Finite-Difference Time-Domain.

B.1 Boundary Element Method - BEM

The Boundary Element Method (BEM) is a numerical computational method to solve linear partial differential equations of field problems by solving an equivalent source problem [60; 61; 62]. Maxwell's equations are expressed in terms of charges σ_j and currents $\vec{h}_j$ at the surfaces of the considered objects (boundary-charge method), j referring to the media ε_j at each side of boundary. These charges and currents interact self-consistently with themselves as well as with any external field.

The advantages in BEM lie in the fact that only the surfaces which are the material interfaces require a discretization (cf. Figure B.1a), contrary to FEM where the whole volume of the object has to be sub-divided. Thus the 3 dimensional physical problem of calculation the electric $\vec{E}$ and magnetic $\vec{H}$ fields is effectively reduced to 2 dimensions. The boundary conditions for the electric and magnetic fields transform Maxwell's equations into surface integrals where surface charges and surface currents are unknowns. Once the surface currents and surface charges are calculated, the scalar potential Φ and the vector potential $\vec{A}$ can be expressed as:

$$\begin{bmatrix} \Phi(\vec{r}) \\ \vec{A}(\vec{r}) \end{bmatrix} = \int d\vec{r'} G_j \left(|\vec{r} - \vec{r'}|\right) \begin{bmatrix} \rho(\vec{r'})/\varepsilon(\vec{r'}, \omega) \\ \vec{j}(\vec{r'})/c \end{bmatrix} + \int_S d\vec{s}\, G_j \left(|\vec{r} - \vec{s}|\right) \begin{bmatrix} \sigma_j(\vec{s}) \\ \vec{h}_j(\vec{s}) \end{bmatrix}, \tag{B.1}$$

where $G_j = \exp(ik_j r)/r$ and $k_j = \omega\sqrt{\varepsilon_j(\omega)}/c$. ρ and $\vec{j}$ are the external charge and current densities respectively. The electric and magnetic fields are then calculated as:

$$\vec{E}(\vec{r}) = \frac{i\omega}{c}\vec{A}(\vec{r}) - \vec{\nabla}\Phi(\vec{r}) \tag{B.2a}$$

$$\vec{H}(\vec{r}) = \vec{\nabla} \times \vec{A}(\vec{r}). \tag{B.2b}$$

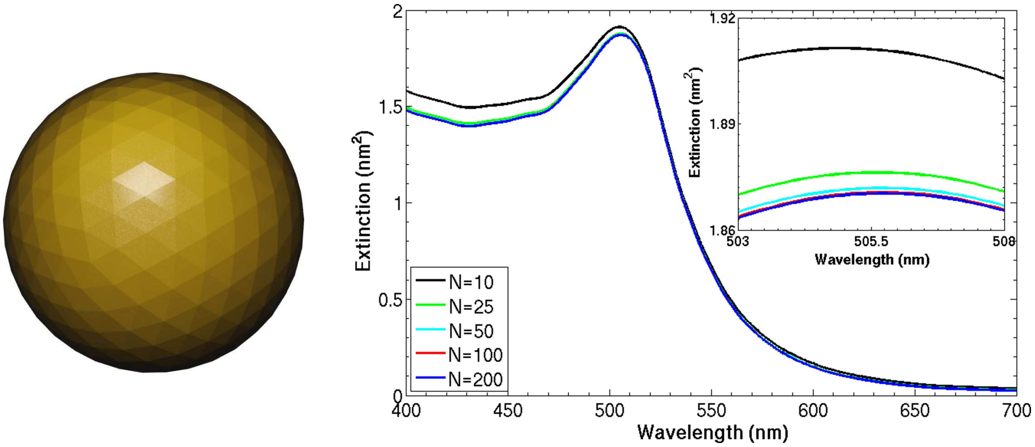

(a)

(b)

Figure B.1: (a) BEM discretizes the surface of the object. (b) Extinction spectra of a gold nanoparticle ($R = 3.5$ nm) in vacuum calculated with BEM for N =10, 25, 50, 100, and 200 points for the contour. Inset: zoom-in view of the LSPR.

Extinction spectra calculated using BEM are shown in Figure B.1b in the simple case of a gold spherical nanoparticle of $R = 4.5$ nm in vacuum. The results are shown for different number of discretization points of the countour N. In this case, complete convergence is obained for $N \approx 50$ (light blue line). Nevertheless, a good convergence can be obtained for $N \approx 25$ (green line).

The version of the BEM used during the development of this thesis is limited to systems with azimuthal symmetry, i.e. that they are the result of a 2π rotation of a given contour. This is the main limitation of the 2D-version of BEM. The only assumption of this method is that the media constituting the considered objects have to be described by a frequency-dependent homogeneous local dielectric function. In that case, the boundaries and interfaces of the objects are sharp and abrupt. A further description of this method can be found in References [60; 61; 62].

B.2 Discrete Dipole Approximation - DDA

The Discrete Dipole Approximation (DDA) was first proposed by Purcell and Pennyparker in 1973 [152] and has been further reviewed, developed and implemented in the DDSCAT package by Draine *et al.* since 1988 [48; 49; 50]. This numerical method solves the problem of scattering and absorption by a finite object, represented by an array of polarizable dipoles (cf. Figure B.2), interacting with a monochromatic plane wave.

The advantage of DDA is the flexibility regarding the geometry of the studied object and is not limited to azimuthal symmetry contrary to 2D BEM. The main limitation of this method is the need to use a interdipole distance d small enough compared to the typical structural dimensions of the considered object. The convergence criterion to be satisfied is: $|\tilde{n}|kd < 1$, where $\tilde{n} = n + i\kappa$ is the complex refractive index of the object material and $k = 2\pi/\lambda$. The actual volume V of the object is then given by the number of dipoles N, located on a cubic array, and the interdipole distance d: $V = Nd^3$ (cf. Figure B.2).

B.3 Finite-Difference Time-Domain - FDTD

Finite-Difference Time-Domain method (FDTD), first introduced in 1966 by Kane Yee, is an effective computational tool for finding numerical solutions of Maxwell's equations [174; 193]. This method is based on the approximation of the derivatives by central differences (leapfrog integration algorithm) and on the use of Yee's scheme to evaluate the electric

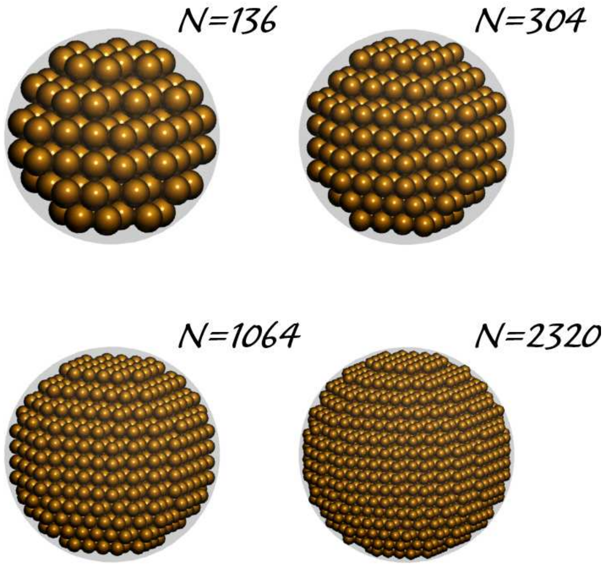

Figure B.2: DDA approximates a solid scatterer (gray sphere) by an array of polarizable N dipoles. Here $N = 136$, 304, 1064, and 2320.

and magnetic field components (cf. Figure B.3). Contrary to the BEM and the DDA, this method is a time-domain method. FDTD is well adapted to large systems (e.g. micro-objects) and to periodic systems (e.g. periodic arrays of nano-objects) [140]. It is widely used for simulations of waveguiding, radar, photonic crytals and metamaterials and other applications in photonics [140].

Yee's algorithm centers the E- and H-components in a three-dimensional space grid as shown in Figure B.3. The E-components are centered on the edges while the H-components are centered on the faces of Yee's cube. FDTD solves Maxwell's curl equations (Equations 4.4c and 4.4d) in a non-magnetic medium ($\vec{J} = \vec{0}$).

In three dimensions, Maxwell's equations have six electromagnetic field components: E_x, E_y, E_z, H_x, H_y, and H_z. If one assumes that the structure is infinite in the z-drirection and that the fields are independent of z:

$$\frac{\partial \vec{E}}{\partial z} = \frac{\partial \vec{H}}{\partial z} = 0, \tag{B.3}$$

then Maxwell's equations split into two independent sets of equations which can be solved in the (x, y) plane only. These are termed the TE (transverse electric), and TM (transverse

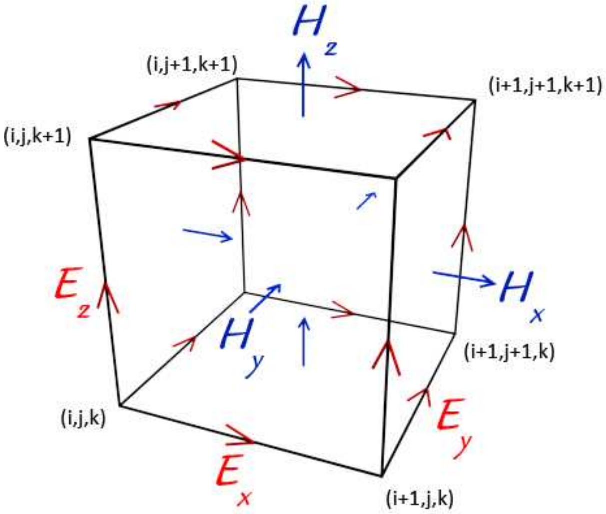

Figure B.3: Yee's cube: Position of the electric and magnetic field components. The E-components (red) are in the middle of the edges and the H-components (blue) are in the center of the faces. i, j, and k label the position on the Yee's grid.

magnetic) equations. Both sets of equations can be solved with the following components: E_x, E_y, H_z for TE, and H_x, H_y, E_z for TM. For example, in the TM case, Maxwell's equations reduce to:

$$\frac{\partial D_z}{\partial t} = \frac{\partial H_y}{\partial x} - \frac{\partial H_x}{\partial y} \tag{B.4a}$$

$$\frac{\partial H_x}{\partial t} = -\frac{1}{\mu_0}\frac{\partial E_z}{\partial y} \tag{B.4b}$$

$$\frac{\partial H_y}{\partial t} = \frac{1}{\mu_0}\frac{\partial E_z}{\partial x}. \tag{B.4c}$$

FDTD is used to calculate the electromagnetic fields as a function of frequency or wavelength by performing Fourier transforms during the simulation. Complex-valued fields and other derived quantities such as the complex Poynting's vector, normalized transmission, and far-field projections can be obtained.

References

[1] E. Abraham and S. D. Smith. Optical bistability and related devices. *Rep. Progr. Phys.*, **45**:815, 1982. 111

[2] M. Aeschlimann, M. Bauer, D. Bayer, T. Brixner, F. J. García de Abajo, W. Pfeiffer, M. Rohmer, C. Spindler, and F. Steeb. Adaptive subwavelength control of nano-optical fields. *Nature*, **446**[7133]:301–304, 2007. 108

[3] J. Aizpurua and G. W. Bryant. *Handbook of Nanophysics, Nanoparticles and Quantum Dots*, chapter 24 "Coupling in Metallic Nanoparticles: Approaches to Optical Nanoantennas", pages 24–1 – 24–18. Handbook of Nanophysics. CRC Press, New York, 2011. 89

[4] J. Aizpurua, G. W. Bryant, L. J. Richter, F. J. García de Abajo, B. K. Kelley, and T. Mallouk. Optical properties of coupled metallic nanorods for field-enhanced spectroscopy. *Phys. Rev. B*, **71**[23]:235420–235432, 2005. 83, 99, 104, 110, 113, 122, 135

[5] J. Aizpurua, P. Hanarp, D. S. Sutherland, M. Käll, G. W. Bryant, and F. J. García de Abajo. Optical properties of gold nanorings. *Phys. Rev. Lett.*, **90**[5]:057401–057403, 2003. 111, 113, 115

[6] J. Aizpurua and A. Rivacoba. Nonlocal effects in the plasmons of nanowires and nanocavities excited by fast electron beams. *Phys. Rev. B*, **78**:035404, 2008. 90

[7] A. V. Akimov, A. Mukherjee, C. L. Yu, D. E. Chang, A. S. Zibrov, P. R. Hemmer, H. Park, and M. D. Lukin. Generation of single optical plasmons in metallic nanowires coupled to quantum dots. *Nature*, **450**[7168]:402–406, 2007. 108

[8] P. Alivisatos. The use of nanocrystals in biological detection. *Nat. Biotech.*, **22**[1]:47–52, 2004. 83

[9] V. R. Almeida, C. A. Barrios, R. R. Panepucci, and M. Lipson. All-optical control of light on a silicon chip. *Nature*, **431**[7012]:1081–1084, 2004. 102, 109

[10] A. Alu and N. Engheta. Tuning the scattering response of optical nanoantennas with nanocircuit loads. *Nat. Photon.*, **2**[5]:307–310, 2008. 102, 105

[11] D. E. Aspnes, A. A. Studna, and E. Kinsbron. Dielectric properties of heavily doped crystalline and amorphous silicon from 1.5 to 6.0 ev. *Phys. Rev. B*, **29**[2]:768–779, 1984. 103

[12] T. Atay, J.-H. Song, and A. V. Nurmikko. Strongly interacting plasmon nanoparticle pairs: From dipole-dipole interaction to conductively coupled regime. *Nano Lett.*, **4**[9]:1627–1631, 2004. 102

[13] H. A. Atwater and A. Polman. Plasmonics for improved photovoltaic devices. *Nat. Mater.*, **9**[3]:205, 2010. 33, 83

[14] D. H. Auston and P. R. Smith. Generation and detection of millimeter waves by picosecond photoconductivity. *Appl. Phys. Lett.*, **43**:631, 1983. 102

[15] G. Bachelier. *Propriétés Optiques de Nano-Structures Métalliques et Semi-Conductrices.* PhD thesis, Université Paul Sabatier, Toulouse III, 2004. xxiii, 35, 85, 86, 87, 122, 123, 137

[16] G. Bachelier, J. Margueritat, A. Mlayah, J. Gonzalo, and C. N. Afonso. Size dispersion effects on the low-frequency Raman scattering of the quasi-spherical silver nanoparticles: Experiment and theory. *Phys. Rev. B*, **76**[23]:235419–235424, 2007. 127

[17] G. Bachelier and A. Mlayah. Surface plasmon mediated Raman scattering in metal nanoparticles. *Phys. Rev. B*, **69**[20]:205408–205414, 2004. 85, 86, 89, 122, 123, 127

[18] K. Bajema and R. Merlin. Raman scattering by acoustic phonons in Fibonacci GaAs-AlAs superlattices. *Phys. Rev. B*, **36**[8]:4555–4557, 1987. 35

[19] M. G. Banaee and K. B. Crozier. Gold nanorings as substrates for surface-enhanced Raman scattering. *Opt. Lett.*, **35**[5]:760–762, 2010. 83, 111

[20] M. Bass, editor. *Handbook of Optics - Optical Properties of Materials, Nonlinear Optics, Quantum Optics*, **IV**. McGraw-Hill, New York, New York; Chicago; San

Francisco; Lisbon; London; Madrid; Mexico City; Milan; New Delhi; San Juan; Seoul; Singapore; Sydney; Toronto, 3rd edition, 2010. 42, 43

[21] V. I. Belitsky, T. Ruf, J. Spitzer, and M. Cardona. Theory of disorder-induced acoustic-phonon Raman scattering in quantum wells and superlattices. *Phys. Rev. B*, **49**[12]:8263–8272, 1994. 36, 68

[22] S. Bellucci, C. Balasubramanian, F. Micciulla, and G. Rinaldi. CNT composites for aerospace applications. *J. Exp. Nanosci.*, **2**[3]:1745–8099, 2005. 34

[23] J. Berthelot, A. Bouhelier, C. Huang, J. Margueritat, G. Colas-des Francs, E. Finot, J.-C. Weeber, A. Dereux, S. Kostcheev, H. I. E. Ahrach, A.-L. Baudrion, J. Plain, R. Bachelot, P. Royer, and G. P. Wiederrecht. Tuning of an optical dimer nanoantenna by electrically controlling its load impedance. *Nano Lett.*, **9**[11]:3914–3921, 2009. 102, 104

[24] C. F. Bohren and D. R. Huffman. *Absorption and Scattering of Light by Small Particles*. Wiley Interscience, 1983. 89, 93, 98, 99

[25] R. W. Boyd. *Nonlinear Optics*. Academic Press, New-York, 3rd edition, 2007. 37

[26] D. W. Brandl, N. A. Mirin, and P. Nordlander. Plasmon modes of nanosphere trimers and quadrumers. *J. Phys. Chem. B*, **110**[25]:12302–12310, 2006. 135

[27] G. W. Bryant, F. J. García de Abajo, and J. Aizpurua. Mapping the plasmon resonances of metallic nanoantennas. *Nano Lett.*, **8**[2]:631–636, 2008. 103

[28] J. Burgin. *Etude femtoseconde de la dynamique électronique et vibrationnelle de nano-objets métalliques et de l'ordre local dans les verres*. PhD thesis, Université Bordeaux I, 2007. 35, 88, 125

[29] J. Burgin, P. Langot, A. Arbouet, J. Margueritat, J. Gonzalo, C. N. Afonso, F. Vallée, A. Mlayah, M. D. Rossell, and G. Van Tendeloo. Acoustic vibration modes and electron-lattice coupling in self-assembled silver nanocolumns. *Nano Lett.*, **8**[5]:1296–1302, 2008. xxiii, 88, 124, 125

[30] M. Cardona, G. Abstreiter, M. H. Grimsditch, P Griinberg, G. Gintherodt, B. Jusserand, R. Merlin, D. L. Mills, A. Pinczuk, and J. C.Tsang. *Light Scattering in Solids* V*: superlattices and other microstructures*. Topics in Applied Physics. Springer, Berlin, 1989. 34, 35, 36, 37, 39, 62, 66, 69

[31] M. Cardona and F. H. Pollak. Energy-band structure of germanium and silicon: The k-p method. *Phys. Rev.*, **142**[2]:530–543, 1966. 42, 49

[32] M. Cazayous, J. Groenen, J. R. Huntzinger, A. Mlayah, and O. G. Schmidt. Spatial correlations and Raman scattering interferences in self-assembled quantum dot multilayer. *Phys. Rev. B*, **64**[3]:33306, 2001. 41

[33] M. Cazayous, J. Groenen, J. R. Huntzinger, A. Mlayah, O. G. Schmidt, and K. Eberl. A new tool for measuring island dimensions and spatial correlations in quantum dot multilayer: Raman scattering interferances. *Mat. Sci. Engin. B*, **88**:173–176, 2002. 41

[34] H.-T. Chen, W. J. Padilla, M. J. Cich, A. K. Azad, R. D. Averitt, and A. J. Taylor. A metamaterial solid-state terahertz phase modulator. *Nat. Photon.*, **3**:148, 2009. 108

[35] W. Cheng, S.-F. Ren, and P. Y. Yu. Erratum: Microscopic theory of the low frequency Raman modes in germanium nanocrystals [phys. rev. b 71, 174305 (2005)]. *Phys. Rev. B*, **72**[5]:059901(E), 2005. 129

[36] W. Cheng, S.-F. Ren, and P. Y. Yu. Microscopic theory of the low frequency Raman modes in germanium nanocrystals. *Phys. Rev. B*, **71**[17]:174305–174314, 2005. 129, 130

[37] C. Colvard, T. A. Gant, M. V. Klein, R. Merlin, R. Fischer, H. Morkoc, and A. C. Gossard. Folded acoustic and quantized optic phonons in (GaAl)As superlattices. *Phys. Rev. B*, **31**[4]:2080–2091, 1985. 35, 36, 69

[38] C. Colvard, R. Merlin, M. V. Klein, and A. C. Gossard. Observation of folded acoustic phonons in a semiconductor superlattice. *Phys. Rev. Lett.*, **45**[4]:298, 1980. 35

[39] N. Combe, J. R. Huntzinger, and A. Mlayah. Vibrations of quantum dots and light scattering properties: Atomistic versus continuous models. *Phys. Rev. B*, **76**[20]:205425–205436, 2007. 129

[40] N. Combe and L. Saviot. Acoustic modes in metallic nanoparticles: Atomistic versus elasticity modeling. *Phys. Rev. B*, **80**[3]:035411–035417, 2009. 85, 87

[41] E. Cubukcu, E. A. Kort, K. B. Crozier, and F. Capasso. Plasmonic laser antenna. *Appl. Phys. Lett.*, **89**[9]:093120, 2006. 83

[42] A. Dahlin, M. Zäch, T. Rindzevicius, M. Käll, D. S. Sutherland, and F. Höök. Localized surface plasmon resonance sensing of lipid-membrane-mediated biorecognition events. *J. Am. Chem. Soc.*, **127**[14]:5043–5048, 2005. 83

[43] G. Danan, B. Etienne, F. Mollot, R. Planel, A. M. Jean-Louis, F. Alexandre, B. Jusserand, G. Le Roux, J. Y. Marzin, H. Savary, and B. Sermage. Optical evidence of the direct-to-indirect-gap transition in gaas-alas short-period superlattices. *Phys. Rev. B*, **35**:6207–6212, 1987. 43

[44] L. C. Davis. Electostatic edge modes of a dielectric wedge. *Phys. Rev. B*, **14**[12]:5523–5525, 1976. 84

[45] N. Del Fatti, F. Vallée, C. Flytzanis, Y. Hamanaka, and A. Nakamura. Electron dynamics and surface plasmon resonance nonlinearities in metal nanoparticles. *Chem. Phys.*, **251**[1–3]:215–226, 2000. 94

[46] N. Del Fatti, C. Voisin, F. Chevy, F. Vallée, and C. Flytzanis. Coherent acoustic mode oscillation and damping in silver nanoparticles. *J. Chem. Phys.*, **110**[23]:11484–11487, 1999. 35, 127

[47] A. Devos, J.-F. Robillard, R. Côte, and P. Emery. High-laser-wavelength sensitivity of the picosecond ultrasonic response in transparent thin films. *Phys. Rev. B*, **74**[6]:064114–064121, 2006. 40

[48] B. T. Draine and P. J. Flatau. Discrete-dipole approximation for scattering calculations. *J. Opt. Soc. Am. B*, **11**[4]:1491–1499, 1994. 149

[49] B. T. Draine and P. J. Flatau. Discrete-dipole approximation for periodic targets: theory and tests. *J. Opt. Soc. Am. B*, **25**[11]:2693–2703, 2008. 149

[50] B. T. Draine and P. J. Flatau. *User Guide for the Discrete Dipole Approximation Code DDSCAT 7.1.* Department of Astrophysical Sciences Princeton University, 108 Peyton Hall Princeton, NJ 08544-1001 U.S.A., 2010. http://arxiv.org/abs/1002.1505v1. 149

[51] E. Duval. Far-infrared and Raman vibrational transitions of a solid sphere: Selection rules. *Phys. Rev. B*, **46**[9]:5795–5797, 1992. 85, 86, 129, 137

[52] V. M. Dzhagan, M. Y. Valakh, A. E. Raevskaya, A. L. Stroyuk, S. Y. Kuchmiy, and D. R. T. Zahn. Size effects on Raman spectra of small CdSe nanoparticles in polymer films. *Nanotechnology*, **19**[30]:305707, 2008. 41

[53] H. Eschrig. *The Fundamentals of Density Functional Theory*. Teubner-Texte zur Physik. Teubner, 2nd edition, 2003. 42

[54] A. Esser, K. Seibert, H. Kurz, G. N. Parsons, C. Wang, B. N. Davidson, G. Lucovsky, and R. J. Nemanich. Ultrafast recombination and trapping in amorphous silicon. *Phys. Rev. B*, **41**[5]:2879–2884, 1990. 102, 108, 109, 110

[55] P. G. Etchegoin, E. C. Le Ru, and M. Meyer. An analytic model for the optical properties of gold. *J. Chem. Phys.*, **125**[16]:164705, 2006. xxix, 94

[56] P. G. Etchegoin, E. C. Le Ru, and M. Meyer. Erratum: "an analytic model for the optical properties of gold" [j. chem. phys. 125, 164705 (2006)]. *J. Chem. Phys.*, **127**[18]:189901, 2007. xxix, 94

[57] A. Fainstein and B. Jusserand. Raman scattering in resonant cavities. In Manuel Cardona and Roberto Merlin, editors, *Light Scattering in Solid IX*, **108** of *Topics in Applied Physics*, pages 17–110. Springer Berlin / Heidelberg, 2007. 39, 40

[58] M. Fuji, T. Nagareda, S. Hayashi, and K. Yamamoto. Raman scattering from acoustic phonons confined in microcrystals: Small gold and silver particles embedded in SiO2 thin films. *J. Phys. Soc. Jpn.*, **61**[2]:754–755, 1992. 135

[59] A. M. Funston, C. Novo, T. J. Davis, and P. Mulvaney. Plasmon coupling of gold nanorods at short distances and in different geometries. *Nano Lett.*, **9**[4]:1651–1658, 2009. 103, 135

[60] F. J. García de Abajo and J. Aizpurua. Numerical simulation of electron energy loss near inhomogeneous dielectrics. *Phys. Rev. B*, **56**[24]:15873–15884, 1997. 147, 149

[61] F. J. García de Abajo and A. Howie. Relativistic electron energy loss and electron-induced photon emission in inhomogeneous dielectrics. *Phys. Rev. Lett.*, **80**[23]:5180–5183, 1998. 90, 113, 147, 149

[62] F. J. García de Abajo and A. Howie. Retarded field calculation of electron energy loss in inhomogeneous dielectrics. *Phys. Rev. B*, **65**[11]:115418–115434, 2002. 90, 113, 147, 149

[63] V. Giannini, A. I. Fernández-Domínguez, Y. Sonnefraud, T. Roschuk, R. Fernández-García, and S. A. Maier. Controlling light localization and

light-matter interactions with nanoplasmonics. *Small*, **6**[22]:2498–2507, 2010. 83, 90, 99

[64] M. Giehler, T. Ruf, M. Cardona, and K. Ploog. Interference effects in acoustic-phonon Raman scattering from GaAs/AlAs mirror-plane superlattices. *Phys. Rev. B*, **55**[11]:7124–7129, 1997. 36, 39, 62

[65] C. Girard and E. Dujardin. Near-field optical properties of top-down and bottom-up nanostructures. *J. Opt. A: Pure Appl. Opt.*, **8**[4]:S73–S86, 2006. 34, 83

[66] A. L. González and C. Noguez. Influence of morphology on the optical properties of metal nanoparticles. *J. Comput. Theor. Nanosci.*, **4**[2]:231–238, 2007. 84

[67] M. A. Green. Intrinsic concentration, effective densities of states, and effective mass in silicon. *J. Appl. Phys.*, **67**[6]:2944–2955, 1990. xxix, 49

[68] F. Hache, D. Ricard, and C. Flytzanis. Optical nonlinearities of small metal particles: surface-mediated resonance and quantum size effects. *J. Opt. Soc. Am. B*, **3**[12]:1647–1655, 1986. 94

[69] N. J. Halas. Plasmonics: An emerging field fostered by nano letters. *Nano Lett.*, **10**[10]:3816–3822, 2010. 34, 89

[70] F. Hao, C. L. Nehl, J. H. Hafner, and P. Nordlander. Plasmon resonances of a gold nanostar. *Nano Lett.*, **7**[3]:729–732, 2007. 83, 84

[71] F. Hao, P. Nordlander, M. T. Burnett, and S. A. Maier. Enhanced tunability and linewidth sharpening of plasmon resonances in hybridized metallic ring/disk nanocavities. *Phys. Rev. B*, **76**[24]:245417–245423, 2007. 111, 113

[72] F. Hao, P. Nordlander, Y. Sonnefraud, P. Van Dorpe, and S. A. Maier. Tunability of subradiant dipolar and fano-type plasmon resonances in metallic ring/disk cavities: Implications for nanoscale optical sensing. *ACS Nano*, **3**[3]:643–652, 2009. 90, 111, 116

[73] F. Hao, Y. Sonnefraud, P. Van Dorpe, S. A. Maier, N. J. Halas, and P. Nordlander. Symmetry breaking in plasmonic nanocavities: Subradiant lspr sensing and a tunable fano resonance. *Nano Lett.*, **8**[11]:3983–3988, 2008. 90, 111, 116

[74] G. V. Hartland. Measurements of the material properties of metal nanoparticles by time-resolved spectroscopy. *Phys. Chem. Chem. Phys.*, **6**:5263–5274, 2004. 88

[75] G. V. Hartland. Coherent excitation of vibrational modes in metallic nanoparticles. *Annu. Rev. Phys. Chem.*, **57**:403–430, 2006. 88

[76] J. He, B. Djafari-Rouhani, and J. Sapriel. Theory of light scattering by longitudinal-acoustic phonons in superlattices. *Phys. Rev. B*, **37**[8]:4086–4098, 1988. 69

[77] E. Hendry, M. J. Lockyear, J. Gómez Rivas, L. Kuipers, and M. Bonn. Ultrafast optical switching of the THz transmission through metallic subwavelength hole arrays. *Phys. Rev. B*, **75**[23]:235305–235309, 2007. 108

[78] J.-H. Huang and R. Chang. Nonlocal and nonlinear effects on the dispersion relation for surface plasmon at a metalkerr medium interface. *J. Opt.*, **12**[4]:045003, 2010. 90

[79] J. R. Huntzinger, J. Groenen, M. Cazayous, A. Mlayah, N. Bertru, C. Paranthoen, and O. Dehaese. Acoustic phonons Raman scattering in InAs/InP self-assembled quantum dots. *Phys. Rev. B.*, **61**[16]:R10547, 2000. 41

[80] J. R. Huntzinger, A. Mlayah, V. Paillard, A. Wellner, N. Combe, and C. Bonafos. Electron–acoustic-phonon interaction and resonant Raman scattering in Ge quantum dots: Matrix and quantum confinement effects. *Phys. Rev. B*, **74**[11]:115308–115319, 2006. 36, 50, 65

[81] K. Ikeda, Y. Shen, and Y. Fainman. Enhanced optical nonlinearity in amorphous silicon and its application to waveguide devices. *Opt. Express*, **15**[26]:17761–17771, 2007. 102, 109

[82] H. Ishida and A. Liebsch. Lifetime of surface plasmons of simple metals: Volume versus surface contributions. *Phys. Rev. B*, **54**:14127–14133, 1996. 90

[83] P. K. Jain, S. Eustis, and M. A. El-Sayed. Plasmon coupling in nanorod assemblies: Optical absorption, discrete dipole approximation simulation, and exciton-coupling model. *J. Phys. Chem. B*, **110**[37]:18243–18253, 2006. 83

[84] P. B. Johnson and R. W. Christy. Optical constants of the noble metals. *Phys. Rev. B*, **6**[12]:4370–4379, 1972. xxiv, xxix, 91, 92, 93, 94, 95, 113

[85] B. Jusserand, D. Paquet, F. Mollot, F. Alexandre, and G. Le Roux. Influence of the supercell structure on the folded acoustical Raman line intensities in superlattices. *Phys. Rev. B*, **35**[6]:2808–2817, 1987. 35, 36, 75

[86] B. N. Khlebtsov and N. G. Khlebtsov. Multipole plasmons in metal nanorods: Scaling properties and dependence on particle size, shape, orientation, and dielectric environment. *J. Phys. Chem. C*, **111**[31]:11516–11527, 2007. 84, 90

[87] C. Kittel. *Introduction to Solid State Physics*. Wiley Interscience, 8th edition, 2005. 42, 48, 71, 91

[88] M. Klein. Phonons in semiconductor superlattices. *Quantum Electronics, IEEE Journal of*, **22**[9]:1760–1770, 1986. 35

[89] M. W. Knight, Y. Wu, J. B. Lassiter, P. Nordlander, and N. J. Halas. Substrates matter: Influence of an adjacent dielectric on an individual plasmonic nanoparticle. *Nano Lett.*, **9**[5]:2188–2192, 2009. 90

[90] D. Kop'ev, D. Mirlin, V. Sapega, and A. Sirenko. Geminate radiative recombination in GaAs/AlGaAs quantum-well structures in magnetic field. *JETP Lett.*, **51**[12]:624–626, 1990. 41

[91] R. de L. Krönig and W. G. Penney. Quantum mechanics of electrons in crystal lattices. *Proc. R. Soc. Lond. A*, **130**:499–513, 1931. 48, 71

[92] H. Kushibe, M. Nakayama, and M. Yokota. Incident-photon energy dependence of Raman-scattering profiles by folded acoustic phonons in GaAs/AlAs superlattices. *Phys. Rev. B*, **47**[15]:9566–9571, 1993. 66, 73

[93] S. Lal, S. E. Clare, and N. J. Hallas. Nanoshell-enabled photothermal cancer therapy: Impending clinical impact. *Acc. Chem. Res.*, **41**[12]:1842–1851, 2008. 33, 83

[94] H. Lamb. On the vibrations of an elastic sphere. *Proc. London Math. Soc.*, **13**[1]:189–212, 1881. 85

[95] C. Langhammer, M. Schwind, B. Kasemo, and I. Zoric. Localized surface plasmon resonances in aluminum nanodisks. *Nano Lett.*, **8**[5]:1461–1471, 2008. 83

[96] N. Large, M. Abb, J. Aizpurua, and O. L. Muskens. Photoconductively loaded plasmonic nanoantenna as building block for ultracompact optical switches. *Nano Lett.*, **10**[5]:1741–1746, 2010. 33, 34, 83, 84, 101

[97] N. Large, J. Aizpurua, S. L. Teo, V. K. Lin, R. Marty, S. Tripathy, and A. Mlayah. Plasmonic properties of gold ring-disk nano-resonators: Fine shape details matter. *Opt. Express*, **19**[6]:5587–5595, 2011. 34, 83, 84, 101

[98] N. Large, Huntzinger J. R., J. Aizpurua, B. Jusserand, and A. Mlayah. Raman-Brillouin electronic density in short period superlattices. *Phys. Rev. B*, **82**[7]:075310, 2010. 34, 36, 66, 67

[99] N. Large, A. Mlayah, L. Saviot, J. Margueritat, J. Gonzalo, C. N. Afonso, and J. Aizpurua. Acousto-plasmonic coupling in engineered metal nanocomposites. In *Lasers and Electro-Optics (CLEO) and Quantum Electronics and Laser Science Conference (QELS), 2010 Conference on*, San Jose, CA, USA, 2010. 34, 84

[100] N. Large, L. Saviot, J. Margueritat, J. Gonzalo, C. N. Afonso, A. Arbouet, P. Langot, A. Mlayah, and J. Aizpurua. Acousto-plasmonic hot spots in metallic nano-objects. *Nano Lett.*, **9**[11]:3732–3738, 2009. 34, 84, 122

[101] E. M. Larsson, J. Alegret, M. Käll, and D. S. Sutherland. Sensing characteristics ofNIR localized surface plasmon resonances in gold nanorings for application as ultrasensitive biosensors. *Nano Lett.*, **7**[5]:1256–1263, 2007. 83, 101, 111

[102] J. B. Lassiter, J. Aizpurua, L. I. Hernandez, D. W. Brandl, I. Romero, S. Lal, J. H. Hafner, P. Nordlander, and N. J. Halas. Close encounters between two nanoshells. *Nano Lett.*, **8**[4]:1212–1218, 2008. 135, 136

[103] J. B. Lassiter, H. Sobhani, J. A. Fan, J. Kundu, F. Capasso, P. Nordlander, and N. J. Halas. Fano resonances in plasmonic nanoclusters: Geometrical and chemical tunability. *Nano Lett.*, **10**[8]:3184–3189, 2010. 90, 99

[104] F. Le, D. W. Brandl, Y. A. Urzhumov, H. Wang, J. Kundu, N. J. Halas, J. Aizpurua, and P. Nordlander. Metallic nanoparticle arrays: A common substrate for both surface-enhanced Raman scattering and surface-enhanced infrared absorption. *ACS Nano*, **2**[4]:707–718, 2008. 83

[105] E. C. Le Ru, J. Grand, N. Félidj, J. Aubard, G. Lévi, A. Hohenau, J. R. Krenn, E. Blackie, and P. G. Etchegoin. Experimental verification of the SERS, electromagnetic model beyond the $|E|^4$ approximation: Polarization effects. *J. Phys. Chem. C*, **112**[22]:8117–8121, 2008. 83, 122

[106] P. A. Letnes, I. Simonsen, and D. L. Mills. Substrate influence on the plasmonic response of clusters of spherical nanoparticles. *Phys. Rev. B*, **83**[7]:075426–075436, 2011. 90

[107] V. K. Lin, S. L. Teo, R. Marty, A. Arbouet, C. Girard, E. Alarcon-Llado, S. H. Liu, M. Y. Han, S. Tripathy, and A. Mlayah. Dual wavelength sensing based on interacting gold nanodisk trimers. *Nanotech.*, **21**[30]:305501, 2010. 83, 111, 135

[108] S. Link, M. B. Mohamed, and M. A. El-Sayed. Simulation of the optical absorption spectra of gold nanorods as a function of their aspect ratio and the effect of the medium dielectric constant. *J. Phys. Chem. B*, **103**[16]:3073–3077, 1999. 84, 124

[109] D. J. Lockwood, M. W. C. Dharma-wardana, J. M. Baribeau, and D. C. Houghton. Folded acoustic phonons in Si/Ge$_x$Si$_{1-x}$ strained-layer superlattices. *Phys. Rev. B*, **35**[5]:2243–2251, 1987. 36

[110] D. J. Lockwood, A. H. MacDonald, G. C. Aers, M. W. C. Dharma-wardana, R. L. S. Devine, and W. T. Moore. Raman scattering in a GaAs/Ga_{1-x},Al_x,As F,ibonacci superlattice. *Phys. Rev. B*, **36**[17]:9286–9289, 1987. 36

[111] C. Loo, A. Lowery, N. J. Halas, J. L. West, and R. Drezek. Immunotargeted nanoshells for integrated cancer imaging and therapy. *Nano Lett.*, **5**[8]:709–711, 2005. 33, 83

[112] A. E. H. Love. *A treatise on the mathematical theory of elasticity.* Dover Publications, New York, 4th edition, 1944. 41, 85, 86

[113] B. Luk'yanchuk, N. I. Zheludev, S. A. Maier, N. J. Halas, P. Nordlander, H. Giessen, and C. T. Chong. The fano resonance in plasmonic nanostructures and metamaterials. *Nat. Mater.*, **9**:707, 2010. 90

[114] K. F. MacDonald, Z. L. Samson, M. I. Stockman, and Nikolay I. Zheludev. Ultrafast active plasmonics. *Nat. Photon.*, **3**[1]:55–58, 2009. 110

[115] S. A. Maier. *Plasmonics: Fundamentals and Applications*, **XXV**. Springer, Berlin, 2007. 34, 83, 89, 91, 93, 94, 96, 97, 98, 99

[116] J. Margueritat, J. Gonzalo, C. N. Afonso, A. Mlayah, D. B. Murray, and L. Saviot. Surface plasmons and vibrations of self-assembled silver nanocolumns. *Nano Lett.*, **6**[9]:2037–2042, 2006. xxiii, 88, 89, 122, 124, 125, 129

[117] R. Marty, A. Arbouet, C. Girard, J. Margueritat, J. Gonzalo, and C. N. Afonso. Sculpting nanometer-sized light landscape with plasmonic nanocolumns. *J. Chem. Phys.*, **131**[22]:224707, 2009. 84, 125, 131

[118] O. Matsuda and O. B. Wright. Laser picosecond acoustics with oblique probe light incidence. *Rev. Sci. Instrum.*, **74**:895, 2003. 40

[119] J. C. Maxwell. *A Treatise on Electricity and Magnetism.* Oxford Univ. Press, London, 1873. xxiii, 89, 90

[120] R. Merlin, K. Bajema, Roy Clarke, F. Y. Juang, and P. K. Bhattacharya. Quasiperiodic GaAs-AlAs heterostructures. *Phys. Rev. Lett.*, **55**[17]:1768–1770, 1985. 35, 36

[121] J. L. Merz, A. S. Barker, and A. C. Gossard. Raman scattering and zone-folding effects for alternating monolayers of GaAs-AlAs. *Appl. Phys. Lett.*, **31**:117, 1977. 35

[122] G. Mie. Beitrage zur optik truber medien, speziell kolloidaler metallosungen. *Ann Phys Vierte Folge*, **Band 25**[3]:377–445, 1908. 99

[123] A. G. Milekhin, A. I. Nikiforov, O. P. Pchelyakov, S. Schulze, and D. R. T. Zahn. Abstract phonons in Ge/Si superlattices with Ge quantum dots. *JETP Lett.*, **73**[9]:461, 2001. 41

[124] A. G. Milekhin, A. I. Nikiforov, O. P. Pchelyakov, S. Schulze, and D. R. T. Zahn. Phonons in self-assembled Ge/Si structures. *Physica E*, **13**:982, 2002. 41

[125] M. I. Mishchenko, J. W. Hovenier, and L. D. Travis. *Light scattering by nonspherical particles.* Academic Press, London, 2000. 84, 89

[126] M. I. Mishchenko, L. D. Travis, and A. A. Lacis. *Scattering, Absorption, and Emission of Light by Small Particles.* Cambridge University Press, New-York, 2004. 89, 99

[127] A. Mlayah and J. Groenen. Resonant Raman scattering by acoustic phonons in quantum dots. In Manuel Cardona and Roberto Merlin, editors, *Light Scattering in Solids IX*, **108/2007** of *Topics in Applied Physics*, pages 237–314. Springer, Berlin, 2007. 35, 41

[128] A. Mlayah, J. R. Huntzinger, and N. Large. Raman-Brillouin light scattering in low-dimensional systems: Photoelastic model versus quantum model. *Phys. Rev. B*, **75**[24]:245303, 2007. 34, 36, 46, 50, 65

[129] P. Mühlschlegel, H.-J. Eisler, O. J. F. Martin, B. Hecht, and D. W. Pohl. Resonant optical antennas. *Science*, **308**[5728]:1607–1609, 2005. 108, 110

[130] D. B. Murray and L. Saviot. Phonons in an inhomogeneous continuum: Vibrations of an embedded nanoparticle. *Phys. Rev. B*, **69**[9]:094305, 2004. 85, 86

[131] O. L. Muskens, N. Del Fatti, and F. Vallée. Femtosecond response of a single metal nanoparticle. *Nano Lett.*, **6**[3]:552–556, 2006. 35, 110

[132] K. Nakayama, K. Tanabe, and H. A. Atwater. Plasmonic nanoparticle enhanced light absorption in GaAs solar cells. *Appl. Phys. Lett.*, **93**[12]:121904–121906, 2008. 33, 83

[133] M. Nakayama, K. Kubota, H. Kato, and N. Sano. Finite-size effects on Raman scattering from GaAs/AlAs superlattices. *J. Appl. Phys.*, **60**[9]:3289, 1986. 77

[134] A. Nelet, A. Crut, A. Arbouet, N. Del Fatti, F. Vallée, H. Portalès, L. Saviot, and E. Duval. Acoustic vibrations of metal nanoparticles: high order radial mode detection. *Appl. Surf. Sci.*, **226**:209–215, 2004. 35, 85

[135] D. F. Nelson and M. Lax. Theory of the photoelastic interaction. *Phys. Rev. B*, **3**[8]:2778, 1971. 38

[136] P. Nordlander. The ring: A leitmotif in plasmonics. *ACS Nano*, **3**[3]:488–492, 2009. 83, 111

[137] P. Nordlander, C. Oubre, E. Prodan, K. Li, and M. I. Stockman. Plasmon hybridization in nanoparticle dimers. *Nano Lett.*, **4**[5]:899–903, 2004. 90, 113, 122, 135, 136

[138] L. Novotny and B. Hecht. *Principles of Nano-Optics*. Cambridge University Press, New-York, 2007. 34, 89, 93, 94, 96, 97, 98, 122

[139] D. P. O'Neal, L. R. Hirsch, N. J. Halas, Payne J.D., and J. L. West. Photothermal tumor ablation in mice using near infrared absorbing nanoshells. *Cancer Lett.*, **209**:171–176, 2004. 33, 83

[140] C. Oubre and P. Nordlander. Optical properties of metallodielectric nanostructures calculated using the finite difference time domain method. *J. Phys. Chem. B*, **108**[46]:17740–17747, 2004. xxix, 84, 92, 93, 116, 150

[141] E. Ozbay. Plasmonics: Merging photonics and electronics at nanoscale dimensions. *Science*, **311**[5758]:189–193, 2006. 33, 83

[142] C. J. Panagamuwa, A. Chauraya, and J. C. Vardaxoglou. Frequency and beam reconfigurable antenna using photoconducting switches. *Antennas and Propagation,* IEEE *Transactions on*, **54**[2]:449–454, 2006. 102

[143] R. A. Paquin. *Handbook of Optics - Optical Properties of Materials, Nonlinear Optics, Quantum Optics, Vol. 4*, chapter 4. McGraw-Hill, New York, 2010. 113

[144] S. Park, M. Pelton, M. Liu, P. Guyot-Sionnest, and N. F. Scherer. Ultrafast resonant dynamics of surface plasmons in gold nanorods. *J. Phys. Chem. C*, **111**[1]:116–123, 2007. 102

[145] M. Pelton, J. Aizpurua, and G. Bryant. Metal-nanoparticle plasmonics. *Laser & Photonics Reviews*, **2**:1–24, 2008. 83, 84, 99

[146] D. R. Penn. Electron mean free paths for free-electron-like materials. *Phys. Rev. B*, **13**[12]:5248–5254, 1976. 94

[147] J. C. Phillips. Band structure of silicon, germanium, and related semiconductors. *Phys. Rev.*, **125**[6]:1931–1936, 1962. 42, 49

[148] F. Pockels. über die änderung der lichtfortpflanzung in kalkspat durch deformationen. *Ann. Physik*, **11**:726–753, 1903. 39

[149] C. J. Powell and J. B. Swan. Origin of the characteristic electron energy losses in aluminum. *Phys. Rev.*, **115**[4]:869–875, 1959. 89

[150] C. J. Powell and J. B. Swan. Effect of oxidation on the characteristic loss spectra of aluminum and magnesium. *Phys. Rev.*, **118**[3]:640–643, 1960. 89

[151] E. Prodan, C. Radloff, N. J. Halas, and P. Nordlander. A hybridization model for the plasmon response of complex nanostructures. *Science*, **302**[5644]:419–422, 2003. 90, 103, 113

[152] E. M. Purcell and C. R. Pennypacker. Scattering and absorption of light by nonspherical dielectric grains. *Astro. J.*, **186**[2]:705–714, 1973. 149

[153] A. H. Quarterman, K. G. Wilcox, V. Apostolopoulos, Z. Mihoubi, S. P. Elsmere, I. Farrer, D. A. Ritchie, and A. Tropper. A passively mode-locked external-cavity semiconductor laser emitting 60-fs pulses. *Nat. Photon.*, **3**[12]:729–731, 2009. 111

[154] F. Ramirez, P. R. Heyliger, A. K. Rappé, and R. G. Leisure. Vibrational modes of free nanoparticles: From atomic to continuum scales. *J. Acoust. Soc. Am.*, **123**:709, 2008. 129

[155] R. M. Ringler, T. A. Klar, A. Schwemer, A. S. Susha, J. Stehr, G. Raschke, S. Funk, M. Borowski, A. Nichtl, K. Kürzinger, R. T. Phillips, and J. Feldmann. Moving nanoparticles with Raman scattering. *Nano Lett.*, **7**[9]:2753–2757, 2007. 122

[156] R. H. Ritchie. Plasma losses by fast electrons in thin films. *Phys. Rev.*, **106**[5]:874–881, 1957. 89

[157] I. Romero, J. Aizpurua, G. W. Bryant, and F. J. García De Abajo. Plasmons in nearly touching metallic nanoparticles: singular response in the limit of touching dimers. *Opt. Express*, **14**[21]:9988–9999, 2006. 102, 106, 111, 122, 135, 136

[158] T. Ruf, V. I. Belitsky, J. Spitzer, V. F. Sapega, M. Cardona, and K. Ploog. Raman scattering from folded phonon dispersion gaps. *Phys. Rev. Lett.*, **71**[18]:3035–3038, 1993. 35, 36

[159] V. F. Sapega, V. I. Belitsky, T. Ruf, H. D. Fuchs, M. Cardona, and K. Ploog. Secondary emission and acoustic-phonon scattering induced by strong magnetic fields in multiple quantum wells. *Phys. Rev. B*, **46**[24]:16005, 1992. 36, 41, 68

[160] V. F. Sapega, V. I. Belitsky, A. J. Shields, T. Ruf, M. Cardona, and K. Ploog. Resonant one-acoustic-phonon Raman scattering in multiple quantum wells. *Solid State Communications*, **84**[11]:1039, 1992. 36, 68

[161] J. Sapriel, J. He, B. Djafari-Rouhani, R. Azoulay, and F. Mollot. Coupled Brillouin-Raman study of direct and folded acoustic modes in GaAs-AlAs superlattices. *Phys. Rev. B*, **37**[8]:4099–4105, 1988. 62

[162] L. Saviot, A. Mermet, and E. Duval. *Handbook of Nanophysics, Nanoparticles and Quantum Dots*, chapter 11 “Acoustic Vibrations in Nanoparticles”, pages 11–1 – 11–16. Handbook of Nanophysics. CRC Press, New York, 2011. 34, 85, 87

[163] L. Saviot and D. B. Murray. Acoustic vibrations of anisotropic nanoparticles. *Phys. Rev. B*, **79**[21]:214101, 2009. 85, 129

[164] M. Schnell, A. García-Etxarri, A. J. Huber, K. Crozier, J. Aizpurua, and R. Hillenbrand. Controlling the near-field oscillations of loaded plasmonic nanoantennas. *Nat. Photon.*, **3**[5]:287–291, 2009. 33, 83, 101, 102, 105, 106

[165] P. J. Schuck, D. P. Fromm, A. Sundaramurthy, G. S. Kino, and W. E. Moerner. Improving the mismatch between light and nanoscale objects with gold bowtie nanoantennas. *Phys. Rev. Lett.*, **94**[1]:017402–017405, 2005. 110

[166] B. E. Sernelius. *Surface modes in Physics.* Wiley Interscience, New-York, 2000. 34, 83, 89, 96, 97

[167] V.M. Silkin and E.V. Chulkov. Energy and lifetime of surface plasmon from first-principles calculations. *Vacuum*, **81**[2]:186–191, 2006. 90

[168] J. Singh. Physics of semiconductors and their heterostructures. In J. Singh, editor, *Electrical and Computer Engineering*, Electrical and Computer Engineering. Mcgraw-Hill, New York, 1993. xxix, 49

[169] A. A. Sirenko, V. I. Belitsky, T. Ruf, M. Cardona, A. I. Ekimov, and C. Trallero-Giner. Spin-flip and acoustic-phonon Raman scattering in CdS nanocrystals. *Phys. Rev. B*, **58**[4]:2077–2087, 1998. 41

[170] K. Sokolowski-Tinten and D. von der Linde. Generation of dense electron-hole plasmas in silicon. *Phys. Rev. B*, **61**[4]:2643–2650, 2000. 102, 103, 108

[171] Y. Sonnefraud, N. Verellen, H. Sobhani, G. A. E. Vandenbosch, V. V. Moshchalkov, P. Van Dorpe, P. Nordlander, and S. A. Maier. Experimental realization of subradiant, superradiant, and fano resonances in ring/disk plasmonic nanocavities. *ACS Nano*, **4**[3]:1664–1670, 2010. 90, 111, 116

[172] C. M. Sotomayor Torres, A. Zwick, F. Poinsotte, J. Groenen, M. Prunilla, J. Ahopelto, A. Mlayah, and V. Paillard. Observations of confined acoustic phonons in silicon membranes. *Phys. Status Solidi (c)*, **1**[11]:2609, 2004. xx, 39, 40, 45, 46, 63

[173] M. A. Suarez, T. Grosjean, D. Charraut, and D. Courjon. Nanoring as a magnetic or electric field sensitive nano-antenna for near-field optics applications. *Opt. Commun.*, **270**[2]:447–454, 2007. 33, 111

[174] A. Taflove. Application of the finite-difference time-domain method to sinusoidal steady-state electromagnetic-penetration problems. *Electromagnetic Compatibility,* IEEE *Transactions on*, **EMC-22**[3]:191–202, 1980. 149

[175] C. E. Talley, J. B. Jackson, C. Oubre, N. K. Grady, C. W. Hollars, S. M. Lane, T. R. Huser, P. Nordlander, and N. Halas. Surface-enhanced Raman scattering from individual Au nanoparticles and nanoparticle dimer substrates. *Nano Lett.*, **5**[8]:1569–1574, 2005. 122

[176] T. Tanabe, M. Notomi, S. Mitsugi, A. Shinya, and E. Kuramochi. Fast bistable all-optical switch and memory on a silicon photonic crystal on-chip. *Opt. Lett.*, **30**[19]:2575–2577, 2005. 102, 109

[177] L. Tang, S. E. Kocabas, S. Latif, A. K. Okyay, D.-S. Ly-Gagnon, K. C. Saraswat, and D. A. B. Miller. Nanometre-scale germanium photodetector enhanced by a near-infrared dipole antenna. *Nat. Photon.*, **2**[4]:226–229, 2008. 33

[178] S. L. Teo, V. K. Lin, R. Marty, N. Large, E. Alarcon Llado, A. Arbouet, C. Girard, J. Aizpurua, S. Tripathy, and A. Mlayah. Gold nanoring trimers: a versatile structure for infrared sensing. *Opt. Express*, **18**[21]:22271–22282, 2010. 83, 84, 101, 111, 135

[179] C. Thomsen, H. T. Grahn, H. J. Maris, and J. Tauc. Surface generation and detection of phonons by picosecond light pulses. *Phys. Rev. B*, **34**[6]:4129–4138, 1986. 40

[180] G. F. Torres del Castillo and I. Rubalcava García. Transfer matrices for piecewise constant potentials. *Revista Mexicana de Física*, **52**[En2]:172–176, 2006. 69

[181] S. Tripathy, R. Marty, V. K. Lin, S. L. Teo, E. Ye, A. Arbouet, L. Saviot, C. Girard, M. Y. Han, and A. Mlayah. Acousto-plasmonic and surface-enhanced Raman scattering properties of coupled gold nanospheres/nanodisk trimers. *Nano Lett.*, **11**[2]:431–437, 2011. 83, 84, 101, 111, 135

[182] W. J. Tropf, M. E. Thomas, and E. W. Rogala. *Handbook of Optics - Optical Properties of Materials, Nonlinear Optics, Quantum Optics, Vol. 4*, chapter 2. McGraw-Hill, New York, 3rd edition, 2010. 113

[183] A. Trügler, J.-C. Tinguely, J. R. Krenn, A. Hohenau, and U. Hohenester. Influence of surface roughness on the optical properties of plasmonic nanoparticles. *Phys. Rev. B*, **83**[8]:081412–081415, 2011. 84

[184] C. G. Van de Walle. Band lineups and deformation potentials in the model-solid theory. *Phys. Rev. B*, **39**[3]:1871–1883, 1989. xxix, 71, 73

[185] Kristy C Vernon, Alison M. Funston, Carolina Novo, Daniel E. Gómez, Paul Mulvaney, and Timothy J. Davis. Influence of particlesubstrate interaction on localized plasmon resonances. *Nano Lett.*, **10**[6]:2080–2086, 2010. 90

[186] W. M. Visscher, A. Migliori, T. M. Bell, and R. A. Reinert. On the normal modes of free vibration of inhomogeneous and anisotropic elastic objects. *J. Acoust. Soc. Am.*, **90**[4]:2154, 1991. 129

[187] H. Wei, A. Reyes-Coronado, P. Nordlander, J. Aizpurua, and H. Xu. Multipolar plasmon resonances in individual Ag nanorice. *ACS Nano*, **4**[5]:2649–2654, 2010. 83

[188] C. Weisbuch and B. Vinter. *Quantum semiconductor structures: fundamentals and applications.* Academic Press, New York, 1991. 66, 77

[189] J. D. Wiley. Valence-band deformation potentials for the III-V compounds. *Solid State Communications*, **8**[22]:1865–1868, 1970. xxix, 71, 73

[190] Y. Wu and P. Nordlander. Plasmon hybridization in nanoshells with a nonconcentric core. *J. Chem. Phys.*, **125**[12]:124708, 2006. 90, 113

[191] G. A. Wurtz, R. Pollard, and A. V. Zayats. Optical bistability in nonlinear surface-plasmon polaritonic crystals. *Phys. Rev. Lett.*, **97**[5]:057402–057405, 2006. 104

[192] H. Xu, J. Aizpurua, M. Käll, and P. Apell. Electromagnetic contributions to single-molecule sensitivity in surface-enhanced Raman scattering. *Phys. Rev. E*, **62**[3]:4318–4324, 2000. 122

[193] K. Yee. Numerical solution of initial boundary value problems involving Maxwell's equations in isotropic media. *Antennas and Propagation,* IEEE *Transactions on*, **14**[3]:302–307, 1966. 149

[194] P. Y Yu and M. Cardona. *Fundamentals of semiconductors: physics and material properties.* Springer, Berlin, 4th edition, 2010. 34, 35, 36, 42

[195] H. Zhang and H.-P. Ho. Quasi-uniform excitation source for cascade enhancement of SERS via focusing of surface plasmons. *Opt. Express*, **17**[23]:21159–21168, 2009. 83

[196] X. Zhang, B. Sun, J. M. Hodgkiss, and R. H. Friend. Tunable ultrafast optical switching via waveguided gold nanowires. *Adv. Mater.*, **20**[23]:4455–4459, 2008. 83

List of Publications Related to this Thesis

Part I

1. A. Mlayah, J. R. Huntzinger, and N. Large. Raman-Brillouin light scattering in low-dimensional systems: Photoelastic model versus quantum model. *Phys. Rev. B*, **75**[24]:245303, 2007.

2. N. Large, J. R. Huntzinger, J. Aizpurua, B. Jusserand, and A. Mlayah. Raman-Brillouin electronic density in short period superlattices. *Phys. Rev. B*, **82**[7]:075310, 2010.

Part II

1. N. Large, L. Saviot, J. Margueritat, J. Gonzalo, C. N. Afonso, A. Arbouet, P. Langot, A. Mlayah, and J. Aizpurua. Acousto-plasmonic hot spots in metallic nano-objects. *Nano Lett.*, **9**[11]:37323738, 2009.

2. N. Large, A. Mlayah, L. Saviot, J. Margueritat, J. Gonzalo, C. N. Afonso, and J. Aizpurua. Acousto-plasmonic coupling in engineered metal nanocomposites. In *Lasers and Electro-Optics (CLEO) and Quantum Electronics and Laser Science Conference (QELS), Conference on*, San Jose, USA, 2010.

3. N. Large, M. Abb, J. Aizpurua, and O. L. Muskens. Photoconductively loaded plasmonic nanoantenna as building block for ultracompact optical switches. *Nano Lett.*, **10**[5]:17411746, 2010.

4. S. L. Teo, V. K. Lin, R. Marty, N. Large, E. Alarcon Llado, A. Arbouet, C. Girard, J. Aizpurua, S. Tripathy, and A. Mlayah. Gold nanoring trimers: a versatile structure for infrared sensing. *Opt. Express*, **18**[21]:2227122282, 2010.
5. N. Large, J. Aizpurua, S. L. Teo, V. K. Lin, R. Marty, S. Tripathy, and A. Mlayah. Plasmonic properties of gold ring-disk nano-resonators: Fine shape details matter. *Opt. Express*, **19**[6]:55875595, 2011.

Index

CEMES

cnrs

CSIC
CONSEJO SUPERIOR DE INVESTIGACIONES CIENTÍFICAS

The work presented here is devoted to the study of the optical and vibrational properties of semiconductor and metallic nanostructures. The inelastic light scattering by low frequency acoustic vibrations, called Raman-Brillouin scattering, gives access to such properties. The confined electronic states of semiconductor nanostructures are involved in the Raman-Brillouin scattering as an intermediary. When applying an external electric field, metallic nano-objects sustain collective oscillation modes of the free electron gas (plasmons) which also act as an intermediary during the emission and the absorption of low frequency acoustic vibrations in the Raman-Brillouin scattering process. The understanding of the interaction between the acoustic vibrations and the electronic excitations (excitons or plasmons) gives direct information on the optical and vibrational properties of those nano-objects. New physical concepts are introduced as theoretical tools for the interpretation of the Raman-Brillouin scattering in semiconductors and metals. An effective electronic density, responsible for the Raman-Brillouin scattering in semiconductors, is here introduced for the first time as new advanced theoretical tool for the interpretation of the inelastic light scattering processes by low frequency acoustic vibrations. The concept of acousto-plasmonics is also introduced for the first time to study and describe the modulation of the plasmonic properties of metallic nano-objects by the acoustic vibrations. These concepts and the numerical methods used in this work (BEM, DDA, FDTD) allowed to interpret fine physical effects such as significant spectral red-shifts of plasmons resonances and unexpected observations of acoustic vibrations by Raman-Brillouin spectroscopy.